COMPUTATIONAL AND EXPERIMENTAL STUDIES ON ENERGY STORAGE MATERIALS AND ELECTROCATALYSTS

by

Jared B. Moss

A thesis submitted in partial fulfillment
of the requirements for the degree

of

MASTER OF SCIENCE

in

Chemistry

Approved:

_____	_____
Tianbiao Leo Liu, Ph.D. Major Professor	Lisa Berreau, Ph.D. Committee Member
_____	_____
Steve Scheiner, Ph.D. Committee Member	Richard S. Inouye, Ph.D. Vice Provost for Graduate Studies

UTAH STATE UNIVERSITY
Logan, Utah

2019

ABSTRACT

Computational and Experimental Studies on Energy Storage Materials and Electrocatalysts

by

Jared B. Moss, Master of Science

Utah State University, 2019

Major Professor: Dr. Leo Liu
Department: Chemistry and Biochemistry

Energy storage materials are a critical component of society in their fundamental operation, from cell-phones and portable devices, to powering cities and reducing greenhouse gas emissions. This thesis focuses on selected energy storage materials along with electrocatalysts as attractive technology for sustainable and benign renewable energy chemistry, specifically: (1) theoretical studies on magnesium chloride / aluminum chloride electrolytes to gain an in-depth understanding of this simple electrolyte system for Mg batteries; (2) theoretical and experimental studies on viologen derivatives for organic redox flow batteries (RFBs); and (3) a new iron(II) polypyridine-based electrocatalyst that exhibits the ability to reduce CO_2 to renewable fuels.

Comprehensive density functional theory (DFT) calculations were conducted to provide insightful and unprecedented thermodynamic information on tetrahydrofuran (THF) solvation, isomerization, chloration, and dimerization of possible Mg-Cl species for popular Mg-Cl complex electrolytes. The results give an indication to the likely

stripping/deposition active species and solution chemistry in electrolyte solutions. The DFT states that the dimer, $[(\mu\text{-Cl})_3Mg_2(THF)_6]^+$, is the most abundant species present in electrolyte solutions and is the likely Mg deposition active species.

The theoretical study of designed viologen derivatives for RFBs was done using the M06-2x functional and 6-31+G(d) basis set to demonstrate that rational molecular engineering can yield a series of efficient two-electron storage viologen molecules as anolyte materials for aqueous organic RFBs. Electrostatic potential surfaces suggest good membrane compatibility for viologen derivatives. Calculations of the frontier HOMO or SOMO indicate high charge delocalization allowing high redox stabilities. Furthermore, calculated redox potentials has aided in the experimental design of high-powered aqueous organic RFBs.

The synthesis and characterization of the $Fe(bapbpy)(OTf)_2$ catalyst is reported. This complex and was found to exhibit the ability to electrochemically reduce CO_2 to renewable fuels such as carbon monoxide (CO), dihydrogen (H_2), and even methane (CH_4) making it an attractive electrocatalyst. Furthermore, the iron(II) catalyst achieved the photochemical CO_2-to-methane conversion with high selectivity over CO production using visible light.

(171 pages)

PUBLIC ABSTRACT

Computational and Experimental Studies on Energy Storage Materials and Electrocatalysts

Jared B. Moss

With the growing global population comes the ever-increasing consumption of energy in powering cities, electric vehicles, and portable devices such as cell-phones. While the power grid is used to distribute energy to consumers, the energy sources needed to power the grid itself are unsustainable and inefficient. The primary energy sources powering the grid, being fossil fuels, natural gas, and nuclear, are unsustainable as the economically-accessible reserves are continually depleted in exchange for detrimental emissions and air-pollutants. Cleaner, renewable sources, such as solar, wind, and hydroelectric, are intermittent and unreliable during the peak hours of energy usage, that is dawn and dusk. However, during waking hours and nighttime sleeping hours, energy consumption plummets resulting in substantial losses of potential energy as these intermittent energy providers do not have the infrastructure to store unused energy. Therefore, the research and development of efficient energy storage materials and renewable energy sources is critical to meet the needs of society in their fundamental operation while reducing harmful emissions. The research presented in this thesis focuses on selected energy storage materials and electrocatalysts as attractive technology for sustainable and benign renewable energy chemistry. Specifically, (1) theoretical studies on magnesium chloride / aluminum chloride electrolytes provide insight for further development of Mg batteries; (2) theoretical and experimental studies on viologen

derivatives for organic redox flow batteries advance the development of these two-electron storage systems; and (3) a new iron(II) polypyridine catalyst that was found to electrochemically reduce CO_2 to produce renewable fuels such as carbon monoxide (CO), hydrogen (H_2), and methane (CH_4), as well as promote the photochemical CO_2-to-methane conversion with visible light.

DEDICATION

I dedicate this thesis, this degree, and this life to the Lord Jesus Christ, the God of Abraham, Isaac, and Jacob. To the One who saved me and simultaneously healed me from autism at age twelve years when received Jesus as my personal Lord and Savior. I can truly say I was "reborn" on that day as a new person. None that I have accomplished could have been done without His help. Thereby, I must fulfill an obligation to give credit where credit is due.

My early childhood was excruciating because of my lack of ability to communicate and socialize. At age four, I was diagnosed with "moderate to severe" autism by the San Diego Autism Research Institute. However, I was found to be very adept at math, fine motor coordination, and learning how to do complex mechanics by mere observation of others. The day I invited God into my life, the physiological aspects of autism were taken away, such as high sensitivity to lights and sounds. The social aspect was quickly overcome as I developed His love for others. I still retained my ability for intense observation which is what eventually brought me to the field of chemistry.

To me, the world of chemistry put me in awe of our Creator as I found the molecular world to be incredibly ordered. 1 Corinthians 14:33 states, "For God is not a God of disorder but of peace." I quickly found that *He is who He says He is* as I observed that the effects of His Word, Love, and Power were consistent in every observed situation. It's a cause-and-effect that occurs regardless of one's disposition. This is why I can conclude, similar to the conclusions in this thesis, that His promises and love are with 100% certainty;

more certainty to that which is held for any observation I've done in chemistry – "as a Grignard reaction may not always occur even at the same conditions."

In the same way one cannot 'see' a magnetic field, the effects of His Power are unmistakable as I have walked these sixteen years in a personal relationship with Him. Therefore, how could I not dedicate everything I have to Him, when He dedicated everything of Himself to me?

ACKNOWLEDGMENTS

"Two are better than one, because they have a good return for their labor. If either of them falls down, one can help the other up. But pity anyone who falls and has no one to help them up" (Ecclesiastes 4:9-10).

Born with nothing, I cannot claim to have gained anything at all without the help of those close to me. Those individuals have helped shape me into who I am, and taught me the value of integrity and good character. To those not mentioned here, I have appreciated your help, kindness, and who you are. Without a doubt, herein lies the most important portion of this thesis.

First and foremost, I want to acknowledge my personal Lord and Savior, and absolute best friend, Jesus Christ. The One who has given me all that I have. Thank You. As I have said during my graduation ceremony for my Bachelor's degree in Chemistry at Weber State University, "I must give credit where credit is due." It would be irresponsible for me to take credit for something that was not my doing. Thank You for Your unending kindness, love, and *patience*, even though I did not deserve it. It goes beyond my comprehension of how deep and great Your love is for me. I love and appreciate You with all that I am. Where would I be without You?

Second, I thank my wife, Tawnie Moss. The most amazing, wonderful, beautiful woman in the entire world. I could not be more blessed to have you in my life. Thank you for saying, "Yes!" You have been there for me and still loved me at my lowest; and have laughed and smiled with me at my highest. You have been so good to me no matter how diverse the situation. You are the one who has lifted me up the most when I have fallen

down. I can only hope to somehow return the measure of love you given to me – as you have set an insurmountable standard. I suppose trying to outdo you in returning that love is what the rest of the journey is for.

Third, I thank my Mom and Dad. You have taught me the most valuable things in life. What it is to have good character; what it is to work hard; what is right, what is wrong (a rare quality in the present days); and what it is to love. There are not many words that can adequately describe my appreciation and gratitude – let me just say, God chose to put me with the right family in all of time and history. Thank you everything you have done for me and for the memories. Many more to come.

To my friends. Rob George, my good friend of sixteen years, who has mentored me on the deepest levels as my youth pastor. I could not have done it without your incredible support. You always believed I could do anything, and here I am. I look forward to continuing to travel the world with you to rescue those who are suffering, those hurting and broken, to bring food to the hungry and hope to the hopeless as we have done in the U.S., Jamaica, Belize, and South Africa. Thank you for building me up to be a Man of God after His own Heart.

Talon Romero and Ryan Finley, you two are great. Thank you for the all the memories we've had since birth and fourth grade, respectively. When I reminisce of what it means to have a good childhood, you two are always there… Rescuing our neighborhood from toilet-paperers using chemistry, ingenuity, and fireworks at two in the morning and the memories of making lasting videos may never be topped.

With the people mentioned above, I would not be who I am today here at Utah State University pursuing my dreams in chemistry. There, too, I have people to thank and give credit where credit is due.

First, I thank my advisor, Dr. Leo Liu, who has given me the opportunity to pursue my dream here at USU. Thank you for your patience during my stubbornness when it took me weeks to learn the same concepts, and for allowing me to have a flexible schedule to fit in my weekly outreach to our next generation of students. You have shown me a lot about what I can do and given me a broad skillset from the many different chemistry projects you allowed me research. Those projects and your time were truly appreciated.

To Dr. Lisa M. Berreau, who has never ceased answering my unending questions, encouraging me when times were rough, and taking precious time for the most insightful discussions of chemistry which rank among my favorite, inspiring moments at USU. Thank you for being genuine. Whether you still have that weird, yellow smiley Bluetooth speaker ball or not, I hope it will always bring you a smile when remembering my crazy hair and wild, enthusiastic presentations.

To Dr. Steve Scheiner, who gave me the summer research opportunity in his lab and taught me the joy of computational chemistry. I credit a lot of this thesis to you as I wouldn't have been able to do the computational presented in this thesis without your help and advice. Thank you for your time and patience in winning over the faceless robots! A victory indeed. That five-year publication will not be forgotten… Well, at least not by me.

Last but not least by any means, my colleagues: Kevin Nielson, Cam DeBruler, Bo Hu, Tatiana Soboleva, Dr. Jian Luo, Dr. Yujing Bi, and others not mentioned but not forgotten. Thank you for your friendship, help, and advice. One can always count on

learning the most from one's colleagues. This couldn't ring truer than in the countless hours spent discussing, reviewing, and laughing with each other over the last three years. During the more intricate of research and productivity therein came the more fruitful of quotes that has driven through the hardships when there was nothing left to keep us going. Yes, while on the brink of existential crisis, where one can no longer stand and tell the difference between reality and meta-reality – the reality of these words come to mind: "Work harder, not smarter!" If you have the desire to ask what to do next, without doubt, the answer is: "More data! MORE FIGURES!" And finally, when all else fails, keep calm and remember this:

– "We're onto something *great* here!" (Lab group moto).

CONTENTS

Page

LIST OF TABLES

LIST OF FIGURES

LIST OF SCHEMES

CHAPTER I

INTRODUCTION

Background

To meet increasing energy demands, advanced batteries are greatly desired for powering portable devices and electric vehicles (EVs) that are pivotal to our daily life and the economic development of the modern society.[1-3] In addition, to address the global problems of escalating energy demand and increasing emissions of CO_2, it is critical to develop effective approaches to converting and storing renewable but intermittently available energy sources (*e.g.* solar, wind, etc.) into reliable energy forms.[4-5] Battery systems with low cost, high energy density and long cycling life time have been suggested as viable technologies for storing sustainable energy.[4-5] In addition to batteries as energy storage devices, catalytic energy conversion systems can enable the reduction of CO_2 to energy-rich fuels to remediate unsustainable energy sources through a renewable carbon cycle.[6]

Solid-State Batteries. Rechargeable Li ion batteries have shown tremendous success in portable electronic devices, power tools, and electric vehicles.[1-3] Moreover, rechargeable Li ion batteries have been recently employed as a power source for electrical vehicles (EVs) and have been helping reduce the use of fossil fuels and emission of CO_2.[1-3] However, technological limitations of Li ion batteries including low energy density, high cost, and safety issues have stimulated the development of the next generation of battery technology.[1-3] Beyond Li ion batteries, pure metal battery systems such as Li batteries and Na batteries are highly attractive and have been regarded as power sources for portable

devices and electric vehicles (EVs) because of their high energy densities and as a potential strategy for grid scale energy storage.[1-3] However, they have not been implemented due to a number of technical issues associated with these highly reactive pure metals, including severe dendrite formation, and irreversible depletion of electrolyte solvents.[7-8]

Recently, rechargeable Mg batteries have been advocated as promising battery systems alternative to Li- or Na-based batteries for powering portable devices and electrical vehicles, and grid-scale energy storage.[7, 9-13] There are several technological advantages of Mg batteries over Li batteries and Na batteries. Mg is earth abundant and low cost (ca. 24 times cheaper than Li). As an anode material, Mg is safe to use without dendrite formation (vs Li, Li ion, or Na batteries) and also due to its milder reactivity compared to Li and Na. Mg has a high volumetric capacity (3832 Ah/L vs 2062 Ah/L for Li and 1165 Ah/L for Na) due to the two-electron redox chemistry of the $Mg^{2+/0}$ redox couple. Mg-based electrolytes are environmentally benign. Furthermore, Mg possesses a sufficient high reduction potential (-2.37 vs SHE) amenable for assembling high voltage and high energy density batteries with suitable cathode materials. However, the biggest roadblock in its development is the electrolyte as it experiences low stability and slow electrochemical cycling kinetics.[14] The development of the Mg-Cl/Al-Cl electrolyte system proved to be a major milestone for Mg batteries, however, optimization is still required to reach satisfactory performance.[14-15] Investigations through density functional theory would be an effective strategy to overcome these barriers by deepening our understanding of the electrolyte solution chemistry.[15-16]

Redox Flow Batteries. Steadily increasing utilization of renewable energy resources, such as solar and wind power, requires affordable and sustainable energy storage

technologies at grid scales up to MW/MWh.[4-5, 17] Redox flow batteries (RFBs) represent one of the most promising battery technologies to overcome the intermittence of renewable energy and supply reliable renewable electricity to grids.[5,17] Simultaneously, implementation of renewable electricity will significantly address the dependence of diminishing fossil fuels and their adverse environmental impact. Operating on the general principle of rechargeable batteries, RFBs employ redox-active materials dissolved in liquid supporting electrolytes as anode and cathode electrolytes (called anolyte and catholyte, respectively).[5, 17-18] During the charge-discharge process, the redox active anolyte and catholyte stored in two separated reservoirs are pumped through the electrode surface to conduct electrochemical reactions.[5, 17-18] The distinctive cell architecture of RFBs empowers a number of attractive technical strengths for large-scale energy storage in comparison to traditional static cells, including decoupled energy and power, high current and high power performance, and safety advantages.[5, 17-18]

However, in spite of these merits, traditional inorganic RFBs, such as vanadium RFBs and Zn-Br_2 RFBs, exhibit a number of material challenges for wide-spread implementation, including expensive active materials (vanadium RFBs), electrolyte crossover (both RFBs), and corrosive and/or hazardous electrolytes (both RFBs).[17-19] Thus, there is an indispensable need to develop new RFB chemistry to address these challenges and achieve sustainable and "green" electrochemical energy storage.[20-21] Given that resource-abundant redox-active organic molecules have been advocated to replace inorganic materials in traditional RFBs, recently, aqueous organic RFBs (AORFBs) and nonaqueous organic RFBs (NAORFBs) have received increasing attention as viable alternatives.[22-42]

Besides the general technical merits of RFBs discussed above, AORFBs have several outstanding advantages for large-scale energy storage, five of which are outlined here.[29] (1) Using organic redox-active molecules consisting of earth-abundant elements is a sustainable practice. (2) Redox-active molecules are also synthetically tunable to gain high oxidation or low reduction redox potentials and can have high solubility, thus offering high energy density RFBs while providing optimal membrane compatibility. (3) Utilization of non-flammable aqueous electrolytes offers safety benefits. (4) Aqueous electrolytes consisting of water and simple inorganic supporting electrolytes, such as NaCl and KOH, are inexpensive. (5) High-conductivity aqueous electrolytes (>100 mS/cm) and well-developed selective ion conductive membranes for aqueous electrolytes allow high-current and high-power operation while achieving high energy efficiency. Rapid progress has been made in the emerging AORFB technology, including high power acid/alkaline AORBFs,[22-23, 26, 43] and high voltage and low-cost neutral AORFBs.[24-25, 28-30] Thus far, pH-neutral AORFBs have displayed the most stable flow battery performance and stand as the state-of-the-art for organic RFBs.[28-30, 41] For example, our group[29] and Aziz *et al.*[30] reported rather stable viologen/ferrocene AORFBs, with a capacity retention of up to 99.99% per cycle for up to 700 cycles at 60 mA/cm^2 using at least 0.5 M active materials. In terms of the battery performance status of AORFBs, it is realistic to develop an AORFB system of 1-2 M active materials at a cost of $5/kg, 0.8 V cell voltage, and area specific resistance of 0.5 $\Omega \cdot cm^2$, meeting the cost target of RFBs for large-scale energy storage, in the range from $100/kWh to $150/kWh, that is proposed by the United States Department of Energy.[44-45]

On the other hand, NAORFBs are claimed to have higher cell voltages and higher energy densities by avoiding the water-splitting voltage window seen in aqueous electrolytes.[20, 45] While still useful, NAORFBs present several major technical challenges for practical applications, four of which are outlined here.[24] (1) The use of flammable organic solvents is not only a safety concern, but also adds additional capital costs.[44-45] (2) Because of the lack of selective ion conductive exchange membranes in organic solvents, NAORFBs commonly run into a severe crossover problem of the redox active molecules that results in significant capacity decay. To minimize this crossover, a mixture of anolyte molecules and catholyte molecules are used as both the catholyte and anolyte in flow battery studies.[46-47] However, this strategy doubles the use of redox active molecules, making NAORFBs more expensive to implement. It is contended that developing selective ion conductive exchange membranes for organic electrolytes is a major challenge for practical applications of NAORFBs. (3) Largely due to low conductivities of organic electrolytes (ca. 10 mS/cm vs. >100 mS/cm for aqueous electrolytes), NAORFBs are typically operated at low current densities (<35 mA/cm^2) to achieve reasonable energy efficiency, but the power density performance of NAORFBs is still unclear.[20, 45] (4) In organic solvents, organic radicals are easily subjected to radical side reactions that lead to capacity decay, even in the state-of-the-art NAORFBs.[46-47] In terms of battery performance, NAORFBs are still in the proof-of-concept stage. For example, the state-of-the-art NAORFBs reported by Wei et al. demonstrated limited cycling tests ($\leq$ 50 cycles at 10 to 35 mA/cm^2 using 0.5 M active materials) with capacity retention less than 99.98% per cycle.[46-47] In the near future, it is anticipated that it will remain very challenging to develop a NAORFB system of 4-5 M active materials at a cost of $5/kg, 3.0 V cell voltage,

and area specific resistance of 5 $\Omega \cdot cm^2$, to meet the cost target of RFBs for large-scale energy storage.[44-45] From the above comparison, it can be reasonably argued that AORFBs are more promising for practical applications in the near future.

Catalytic Energy Storage Systems. The increasing global energy demands are accompanied by increased energy consumption that further depletes economically-accessible fossil fuel reserves while reducing air-quality.[48-49] It becomes vital to have sustainable energy conversion systems that positively impact the worldwide carbon balance by recycling CO_2 to reusable fuels.[50-51] Inspiring approaches to ameliorate these obstacles are the electrochemical reduction of CO_2 or the elegant sunlight-to-fuel process of photochemical reduction of CO_2 into fuels and precursors such as carbon monoxide, formic acid, methanol, or methane.[51-55] The conversion from power to synthetic natural gas constitutes a desirable method to recycle fossil fuels while reducing CO_2 emissions as a sustainable energy storage cycle.[49, 56-57] In addition to recycling emissions and fuel production, the electrocatalytic reduction of CO_2 can produce C_1 building blocks for the synthesis of inexpensive organic chemicals.[58-59]

While early efforts focused on trace metals such as Re, Ru, and Pd, recently, the major focus has shifted to the earth-abundant metals, Mn, Fe, Co, and Ni to achieve the catalytic reduction of CO_2.[60] By the application of appropriate ligands and tuning of the conditions, these metals have rivaled their heavier homologues in the homogeneous electrocatalytic reduction of CO_2.[61-63] In this approach (Scheme 1-1), current is supplied to the electrode to reduce the solvated catalyst at a specific potential, preferably close to that of the thermodynamic reduction potential of CO_2 at the given conditions to minimize overpotential.[64-65] Overpotential is the difference between the minimum thermodynamic

potential required to reduce CO_2 and the observed reduction potential.[64] The reduced catalyst then goes on to reduce the solvated CO_2 to form CO or other further reduced products given the presence of a suitable proton donor.[63]

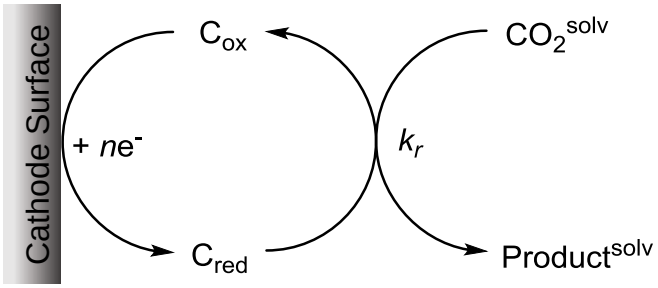

Scheme 1-1. Cycle for the homogeneous electrocatalytic reduction of CO_2.

The homogeneous electrocatalytic reduction of CO_2 is no trivial task due to the large number of reaction pathways and high overpotentials of the cathodic process encountered with the lowest overpotentials *ca.* 0.3 V to 0.45 V.[60, 66-67] To demonstrate a few select reaction pathways, Table 1-1 shows the typical one-, two-, four-, six-, and eight-electron reduction products of CO_2 and their required standard reduction potentials in aqueous solutions. Furthermore, the primary undesirable competitive side reaction in the electrochemical reduction of CO_2 is the hydrogen evolution reaction (HER).[60] There are several influences on the selectivity including the electrode, proton source, and concentration of the system.[60, 63, 65, 68] Many CV studies use the platinum electrode, however, it is exceptionally active towards the HER making it a poor choice for electrocatalytic reduction of CO_2.[60] In contrast, Hg electrodes offer a broad potential window for electrocatalytic studies, however, environmental and safety concerns have led to the wide use of glassy carbon (GC) electrodes.[60] The solvent, proton source, and pH of

the system have been shown to have significant influences on selectivity and is typically optimized as a main parameter for increased selectivity.[52, 65, 69] In some studies, the sustained formation of CO was only achieved with the addition of Brönsted acids, however, proton transfers in the coordination sphere of the homogeneous catalyst increases the possibility of catalyzing the acid to dihydrogen.[65, 70-72] By decreasing the strength of the acid from common donors such as Et_3NH^+, propanol, water, and trifluorethanol[73] and extending the acid range to phenol, CO faradaic yields close to 100% have been achieved.[64-65, 74]

Table 1-1. Standard Reduction Potentials for Selected CO_2 Reduction Process in Aqueous Media.[50, 54, 69]

Reduction Process	$E°'$ (V vs NHE) in water	$E°'$ (V vs NHE) in MeCN
$CO_2 + e^- = CO_2^{\bullet-}$	–1.90	
$CO_2 + 2H^+ + 2e^- = CO + H_2O$	–0.53	–0.12
$CO_2 + 2H^+ + 2e^- = HCO_2H + H_2O$	–0.61	
$CO_2 + 4H^+ + 4e^- = HCHO + H_2O$	–0.48	
$CO_2 + 6H^+ + 6e^- = CH_3OH + H_2O$	–0.38	
$CO_2 + 8H^+ + 8e^- = CH_4 + 2H_2O$	–0.24	+0.15

Few catalysts have been found to be selective for multi-electron processes greater than two electrons. Berben and co-worker's catalyst is notable for being one of the few to electrocatalytically convert CO_2 to formate in water with a Faradaic Efficiency (FE) of 95% (Figure 1-1).[75-76] Using a cobalt catalyst, Artero *et al.* achieved the selective formation of formic acid in DMF/water mixtures with a cyclopentanedienyl cobalt catalyst

demonstrating TOF_{max} numbers of up to 1000 s^{-1} and overpotentials of 500-700 mV using the half-wave potential, $E_{1/2}$.[77] While there have been several other accounts of the electroreduction of CO_2 beyond two electrons, there have been no reported homogeneous catalysts that can electrochemically reduce CO_2 to methane.[60]

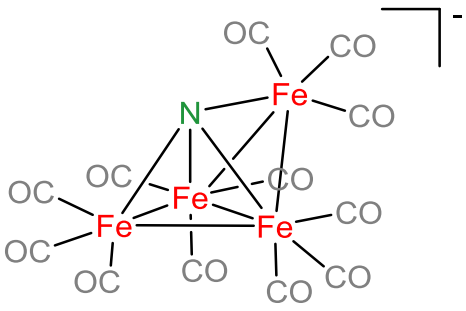

Figure 1-1. Butterfly-shaped $[Fe_4N(CO)_{12}]^-$ cluster proposed by Berben *et al.* to catalyze the selective reduction of CO_2 to formate.[75]

While there have been no reported homogeneous molecular catalysts that can electrochemically convert CO_2 to methane, a recent study demonstrates the first homogeneous catalyst to photochemically reduce CO_2 to methane using an iron porphyrin catalyst with TEA as a proton donor and an $Ir(ppy)_3$ photosensitizer (Figure 1-2).[49, 78] In this method, a photosensitizer is used that has a sufficient excited-state reduction potential in combination with a sacrificial electron and proton donor, and a catalyst active towards CO_2 reduction.[78] As shown in Scheme 2-1, the photosensitizer is first excited with light increasing its reduction potential sufficient to reduce the active catalyst and subsequently regenerated using a sacrificial electron donor, completing the photochemical cycle.[79] The reduced active catalyst forms the CO_2 adduct and undergoes multiple electron reductions

provided by the excited photosensitizer while being supplied protons from the proton source (Scheme 2-1).[78] While this is a promising approach for CO_2-to-fuel conversion, the selectivity and catalyst lifetime requires further development.

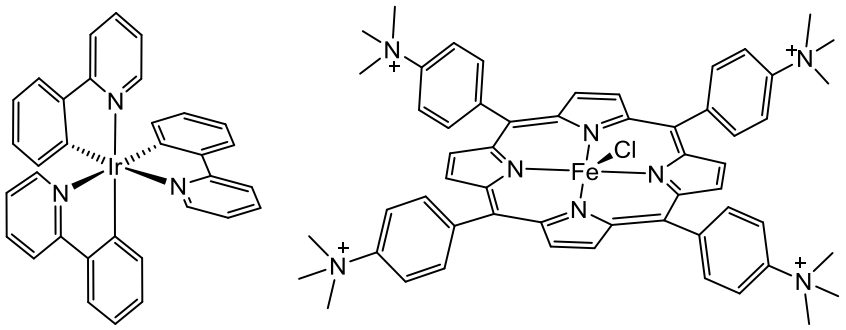

Figure 1-2. Iron porphyrin catalyst and photosensitizer used by Rao *et al.* in the photochemical reduction of CO_2 to methane.[78]

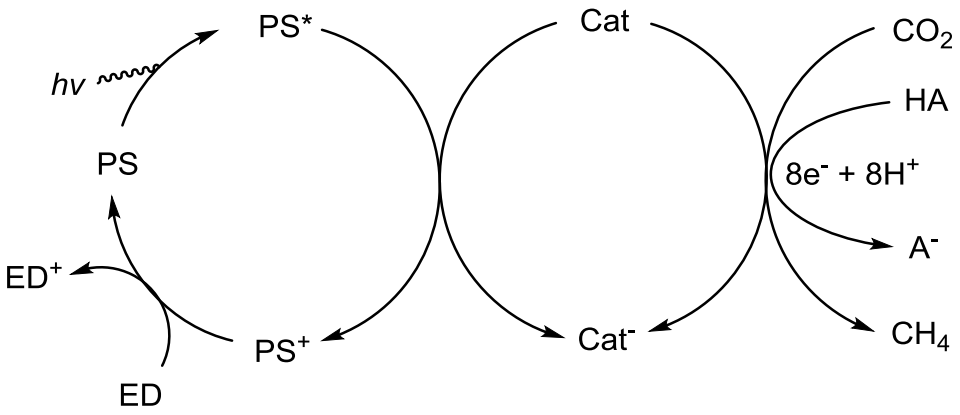

Scheme 1-2. The photochemical reduction cycle of CO_2 where PS is the photosensitizer, ED is the sacrificial electron donor, Cat is the catalyst, and HA is the proton donor.

Summary of Chapters. The research presented herein emphasizes the art of molecular engineering for energy storage systems as they relate to Mg batteries, redox flow batteries (RFBs), and catalyst development for CO_2 reduction.

Chapter 2 details a comprehensive investigation on the solvation chemistry of Mg-Cl/Al-Cl electrolytes in THF by applying density functional theory (DFT) at the M06-2x/6-31+G(d) level to elucidate the most thermodynamically favorable solution product. To determine the thermodynamic solvated species, all Mg-Cl and Al-Cl structures were optimized using an ultrafine integration grid while simultaneously applying a dielectric field to model the implicit solvent using the universal solvation model, SMD. Although this approach is computationally expensive, the cost was deemed necessary to accurately determine the thermodynamic favorability of Mg-Cl dimers and trimer formation in THF solution.

Chapter 3 demonstrates that rational molecular engineering yielded a series of efficient two-electron storage viologen molecules as anolyte materials for AORFBs. DFT was used to model the electrostatic surface potential as a means to investigate cation exchange membrane compatibility. Theoretical reduction potentials of viologen were calculated using methyl viologen (MV) as the relative reference molecule. This method was found to be in excellent experimental agreement for known viologens demonstrating its effectiveness in predicting redox potentials of never-before-synthesized viologen derivatives. These synthetic and computational chemistry provided in this study opens up new avenues for the development of high voltage, and high-power and energy-dense anolyte materials for AORFBs.

Chapter 4 describes the synthesis, characterization, and catalytic chemistry of a new tetradentate polypyridine iron(II) complex used for the electrochemical and photochemical reduction of CO_2 to generate energy-rich products. The characterization includes a complete paramagnetic resonance assignment of the ^{1}H NMR spectrum supported by a 2D ^{1}H DQF-COSY spectrum. Investigation of the catalytic performance and optimization towards the electrochemical and photochemical reduction of CO_2 revealed formation of CO and CH_4 upon GC analysis at a relatively small overpotential. The catalyst exhibited fast kinetics upwards of 120,000 s^{-1} during the reduction of acids to dihydrogen, albeit at a moderate overpotential. Based on the polypyridine backbone with two pendent amines present in the ligand, a rationale is proposed for the eight-electron reduction of the CO_2 adduct.

References

1. Armand, M.; Tarascon, J. M. *Nature* **2008**, *451*, 652-657.
2. Goodenough, J. B.; Park, K.-S. *J. Am. Chem. Soc.* **2013**, *135*, 1167-1176.
3. Chu, S.; Cui, Y.; Liu, N. *Nature Materials* **2016**, *16*, 16.
4. Dunn, B.; Kamath, H.; Tarascon, J.-M. *Science* **2011**, *334*, 928-935.
5. Yang, Z.; Zhang, J.; Kintner-Meyer, M. C. W.; Lu, X.; Choi, D.; Lemmon, J. P.; Liu, J. *Chem. Rev.* **2011**, *111*, 3577-3613.
6. Feng, D.-M.; Zhu, Y.-P.; Chen, P.; Ma, T.-Y. *Catalysis* **2017**, *7*, 373-391.
7. Xu, W.; Wang, J.; Ding, F.; Chen, X.; Nasybulin, E.; Zhang, Y.; Zhang, J.-G. *Energy Environ. Sci.* **2014**, *7*, 513-537.
8. Liu, B.; Zhang, J.-G.; Xu, W. *Joule* **2018**, *2*, 833-845.

9. Yoo, H. D.; Shterenberg, I.; Gofer, Y.; Gershinsky, G.; Pour, N.; Aurbach, D. *Energy Environ. Sci.* **2013**, *6*, 2265-2279.

10. Muldoon, J.; Bucur, C. B.; Gregory, T. *Chem. Rev.* **2014**, *114*, 11683-11720.

11. Canepa, P.; Sai Gautam, G.; Hannah, D. C.; Malik, R.; Liu, M.; Gallagher, K. G.; Persson, K. A.; Ceder, G. *Chem. Rev.* **2017**, *117*, 4287-4341.

12. He, S.; Nielson, K. V.; Luo, J.; Liu, T. L. *Energy Storage Mater.* **2017**, *8*, 184-188.

13. Rajput, N. N.; Seguin, T. J.; Wood, B. M.; Qu, X.; Persson, K. A. *Top. Curr. Chem.* **2018**, *376*, 19.

14. Liu, T.; Shao, Y.; Li, G.; Gu, M.; Hu, J.; Xu, S.; Nie, Z.; Chen, X.; Wang, C.; Liu, J. *J. Mat. Chem. A* **2014**, *2*, 3430-3438.

15. Liu, T.; Cox, J. T.; Hu, D.; Deng, X.; Hu, J.; Hu, M. Y.; Xiao, J.; Shao, Y.; Tang, K.; Liu, J. *Chem. Commun.* **2015**, *51*, 2312-2315.

16. Canepa, P.; Jayaraman, S.; Cheng, L.; Rajput, N. N.; Richards, W. D.; Gautam, G. S.; Curtiss, L. A.; Persson, K. A.; Ceder, G. *Energy Environ. Sci.* **2015**, *8*, 3718-3730.

17. Soloveichik, G. L. *Chem. Rev.* **2015**, *115*, 11533-11558.

18. Wang, W.; Luo, Q.; Li, B.; Wei, X.; Li, L.; Yang, Z. *Adv. Funct. Mater.* **2013**, *23*, 970-986.

19. Darling, R. M.; Gallagher, K. G.; Kowalski, J. A.; Ha, S.; Brushett, F. R. *Energy Environ. Sci.* **2014**, *7*, 3459-3477.

20. Winsberg, J.; Hagemann, T.; Janoschka, T.; Hager, M. D.; Schubert, U. S. *Angew. Chem. Int. Ed.* **2016**, *56*, 686-711.

21. Ding, Y.; Yu, G. *Angew. Chem. Int. Ed.* **2017**, *56*, 8614-8616.

22. Huskinson, B.; Marshak, M. P.; Suh, C.; Er, S.; Gerhardt, M. R.; Galvin, C. J.; Chen, X.; Aspuru-Guzik, A.; Gordon, R. G.; Aziz, M. J. *Nature* **2014**, *505*, 195-198.

23. Yang, B.; Hoober-Burkhardt, L.; Wang, F.; Surya Prakash, G. K.; Narayanan, S. R. *J. Electrochem. Soc.* **2014**, *161*, A1371-A1380.

24. Liu, T.; Wei, X.; Nie, Z.; Sprenkle, V.; Wang, W. *Adv. Energy Mater.* **2016**, *6*, 1501449.

25. Janoschka, T.; Martin, N.; Martin, U.; Friebe, C.; Morgenstern, S.; Hiller, H.; Hager, M. D.; Schubert, U. S. *Nature* **2015**, *527*, 78-81.

26. Lin, K.; Gómez-Bombarelli, R.; Beh, E. S.; Tong, L.; Chen, Q.; Valle, A.; Aspuru-Guzik, A.; Aziz, M. J.; Gordon, R. G. *Nature Energy* **2016**, *1*, 16102.

27. Ding, Y.; Yu, G. *Angew. Chem. Int. Ed.* **2016**, *55*, 4772-4776.

28. Janoschka, T.; Martin, N.; Hager, M. D.; Schubert, U. S. *Angew. Chem. Int. Ed.* **2016**, *55*, 14427-14430.

29. Hu, B.; DeBruler, C.; Rhodes, Z.; Liu, T. L. *J. Am. Chem. Soc.* **2017**, *139*, 1207-1214.

30. Beh, E. S.; De Porcellinis, D.; Gracia, R. L.; Xia, K. T.; Gordon, R. G.; Aziz, M. J. *ACS Energy Lett.* **2017**, *2*, 639-644.

31. Wei, X.; Xu, W.; Vijayakumar, M.; Cosimbescu, L.; Liu, T.; Sprenkle, V.; Wang, W. *Adv. Mater.* **2014**, *26*, 7649-7653.

32. Wei, X.; Cosimbescu, L.; Xu, W.; Hu, J. Z.; Vijayakumar, M.; Feng, J.; Hu, M. Y.; Deng, X.; Xiao, J.; Liu, J.; Sprenkle, V.; Wang, W. *Adv. Energy Mater.* **2015**, *5*, 1400678.

33. Huang, J.; Cheng, L.; Assary, R. S.; Wang, P.; Xue, Z.; Burrell, A. K.; Curtiss, L. A.; Zhang, L. *Adv. Energy Mater.* **2015**, *5*, 1401782.

34. Sevov, C. S.; Hickey, D. P.; Cook, M. E.; Robinson, S. G.; Barnett, S.; Minteer, S. D.; Sigman, M. S.; Sanford, M. S. *J. Am. Chem. Soc.* **2017**, *139*, 2924-2927.

35. Gong, K.; Fang, Q.; Gu, S.; Li, S. F. Y.; Yan, Y. *Energy Environ. Sci.* **2015**, *8*, 3515-3530.

36. Zhao, Y.; Ding, Y.; Li, Y.; Peng, L.; Byon, H. R.; Goodenough, J. B.; Yu, G. *Chem. Soc. Rev.* **2015**, *44*, 7968-7996

37. Sevov, C. S.; Brooner, R. E. M.; Chénard, E.; Assary, R. S.; Moore, J. S.; Rodríguez-López, J.; Sanford, M. S. *J. Am. Chem. Soc.* **2015**, *137*, 14465-14472.

38. Ding, Y.; Li, Y.; Yu, G. *Chem* **2016**, *1*, 790-801.

39. Orita, A.; Verde, M. G.; Sakai, M.; Meng, Y. S. *Nat. Commun.* **2016**, *7*, 13230.

40. Ding, Y.; Zhao, Y.; Li, Y.; Goodenough, J. B.; Yu, G. *Energy Environ. Sci.* **2017**, *10*, 491-497.

41. Hu, B.; Seefeldt, C.; DeBruler, C.; Liu, T. *J. Mat. Chem. A* **2017**, *139*, 1207-1214.

42. Xu, Y.; Wen, Y.; Cheng, J.; Yanga, Y.; Xie, Z.; Cao, G., Novel Organic Redox Flow Batteries using Soluble Quinonoid Compounds as Positive Materials. In *World Non-Grid-Connected Wind Power and Energy Conference*, IEEE: Nanjing, China, 2009; 1-4.

43. Lin, K.; Chen, Q.; Gerhardt, M. R.; Tong, L.; Kim, S. B.; Eisenach, L.; Valle, A. W.; Hardee, D.; Gordon, R. G.; Aziz, M. J.; Marshak, M. P. *Science* **2015**, *349*, 1529-1532.

44. Dmello, R.; Milshtein, J. D.; Brushett, F. R.; Smith, K. C. *J. Power Sources* **2016**, *330*, 261-272.

45. Leung, P.; Shah, A. A.; Sanz, L.; Flox, C.; Morante, J. R.; Xu, Q.; Mohamed, M. R.; Ponce de León, C.; Walsh, F. C. *J. Power Sources* **2017**, *360*, 243-283.

46. Wei, X.; Xu, W.; Huang, J.; Zhang, L.; Walter, E.; Lawrence, C.; Vijayakumar, M.; Henderson, W. A.; Liu, T.; Cosimbescu, L.; Li, B.; Sprenkle, V.; Wang, W. *Angew. Chem. Int. Ed.* **2015**, *54*, 8684-8687.

47. Wei, X.; Duan, W.; Huang, J.; Zhang, L.; Li, B.; Reed, D.; Xu, W.; Sprenkle, V.; Wang, W. *ACS Energy Lett.* **2016**, *1*, 705-711.

48. Okabe, Y.; Lee, S. K.; Kondo, M.; Masaoka, S. *J. Biol. Inorg. Chem.* **2017**, *22*, 713-725.

49. Steinlechner, C.; Junge, H. *Angew. Chem. Int. Ed.* **2018**, *57*, 44-45.

50. Benson, E. E.; Kubiak, C. P.; Sathrum, A. J.; Smieja, J. M. *Chem. Soc. Rev.* **2009**, *38*, 89-99.

51. Benson, E. E.; Kubiak, C. P.; Sathrum, A. J.; Smieja, J. M. *Chem. Soc. Rev.* **2009**, *38*, 89-99.

52. Rountree, E. S.; McCarthy, B. D.; Eisenhart, T. T.; L., D. J. *Inorg. Chem.* **2014**, *53*, 9983-10002.

53. Sahara, G.; Ishitani, O. *Inorg. Chem.* **2015**, *54*, 5096-5104.

54. Sutin, N.; Creutz, C.; Fujita, E. *Comments Inorg. Chem.* **1997**, *19*, 67-92.

55. Morris, A. J.; Meyer, G. J.; Fujita, E. *Acc. Chem. Res.* **2009**, *42*, 1983-1994.

56. Amirante, R.; Distaso, E.; Iorio, S. D.; Sementa, P.; Tamburrano, P.; Vaglieco, B. M.; Reitz, R. D. *Energy Convers. and Manage.* **2017**, *143*, 338-347.

57. Olah, G. A.; Prakash, G. K. S.; Goeppert, A. *J. Am. Chem. Soc.* **2011**, *133*, 12881-12898.

58. Liu, Q.; Wu, L.; Jackstell, R.; Beller, M. *Nat. Commun.* **2015**, *6*, 5933.

59. Aresta, M. *Carbon Dioxide as Chemical Feedstock*, Wiley-VCH: Weinheim, **2010**.

60. Francke, R.; Schille, B.; Roemelt, M. *Chem. Rev.* **2018**, *118*, 4631-4701.

61. Smieja, J. M.; Sampson, M. D.; Grice, K. A.; Benson, E. E.; Froehlich, J. D.; Kubiak, C. P. *Inorg. Chem.* **2013**, *52*.

62. Sampson, M. D.; Kubiak, C. P. *J. Am. Chem. Soc.* **2016**, *138*, 1386-1393.

63. Costentin, C.; Drouet, S.; Robert, M.; Savéant, J.-M. *Science* **2012**, *338*.

64. Costentin, C.; Drouet, S.; Robert, M.; Savéant, J.-M. *J. Am. Chem. Soc.* **2012**, *134*, 11235-11242.

65. Costentin, C.; Robert, M.; Savéant, J.-M.; Tatin, A. *PNAS* **2015**, *112*, 6882-6886.

66. Lu, Q.; Jiao, F. *Nano Energy* **2016**, *29*, 436-456.

67. Zhang, W.; Hu, Y.; Ma, L.; Zhu, G.; Wang, Y.; Xue, X.; Chen, R.; Yang, S.; Jin, Z. *Adv. Sci.* **2018**, *5*, 1700275.

68. McCarthy, B. D.; Martin, D. J.; Rountree, E. S.; Ullman, A. C.; Dempsey, J. L. *Inorg. Chem.* **2014**, *53*, 8350-8361.

69. Pegis, M. L.; Roberts, J. A. S.; Wasylenko, D. J.; Mader, E. A.; Appel, A. M.; Mayer, J. M. *Inorg. Chem.* **2015**, *54*, 11883-11888.

70. Hammouche, M.; Lexa, D.; Savéant, J.-M.; Momenteau, M. *J. Electroanal. Chem.* **1988**, *249*.

71. Bhugun, I.; Lexa, D.; Saveant, J.-M. *J. Am. Chem. Soc.* **1994**, *116*, 5015-5016.

72. Bhugun, I.; Lexa, D.; Saveant, J.-M. *J. Am. Chem. Soc.* **1996**, *118*, 1769-1776.

73. Bhugun, I.; Lexa, D.; Savéant, J.-M. *J. Am. Chem. Soc.* **1996**, *118*, 3982-3983.

74. Costentin, C.; Drouet, S.; Passard, G.; Robert, M.; Savéant, J.-M. *J. Am. Chem. Soc.* **2013**, *135*, 9023-9031.

75. Taheri, A.; Thompson, E. J.; Fettinger, J. C.; Berben, L. A. *ACS Catal.* **2015**, *5*, 7140-7151.

76. Taheri, A.; Berben, L. A. *Chem. Commun.* **2016**, *52*, 1768-1777.

77. Roy, S.; Sharma, B.; Pecaut, J.; Simon, P.; Fontecave, M.; Tran, P. D.; Derat, E.; Artero, V. *J. Am. Chem. Soc.* **2017**, *139*, 3685-3696.

78. Rao, H.; Schmidt, L. C.; Bonin, J.; Robert, M. *Nature* **2017**, *548*, 74-77.

79. Koike, T.; Akita, M. *Inorg. Chem. Front.* **2014**, *1*, 562-576.

CHAPTER II

COMPUTATIONAL INSIGHTS INTO MAGNESIUM CHLORIDE COMPLEX ELECTROLYTES AND ALUMINUM CHLORIDE INTERACTIONS IN THF FOR RECHARGEABLE MAGNESIUM BATTERIES

Abstract

DFT calculations were conducted to provide insightful and unprecedented thermodynamic insights on THF solvation, isomerization, chloration, dimerization, and trimerization of possible Mg-Cl coordination species for the popular Mg-Cl electrolytes. Computational results using M06-2x functional with the 6-31+G(d) basis set indicate trigonal bipyramidal *e,e-cis-tbp*-$MgCl_2(THF)_3$ (I) dichloride species and octahedral $[MgCl(THF)_5]^+$ monochloride species are the dominant monomers. These two can combine to form the active dimer species, $[(\mu\text{-}Cl)_3Mg_2(THF)_6]^+$ with free energy -6.30 kcal/mol, which is calculated to be the dominant Mg-Cl species in solution but still in an equilibrium with *e,e-cis-tbp*-$MgCl_2(THF)_3$ (I) and $[MgCl(THF)_5]^+$ monomers. In addition, solvation chemistry of $AlCl_3$ Lewis acid was also studied at the same computational level, suggesting that *trans*-$AlCl_3(THF)_2$ is the major species and in an equilibrium with a minor ionic pair, [*trans*-$AlCl_2(THF)_4$][$AlCl_4$]. Three mono-cation species, $[(\mu\text{-}Cl)_3Mg_2(THF)_6]^+$ and $[MgCl(THF)_5]^+$ have comparable LUMO energies, thus all of them can act as active species for Mg deposition. However, the significant relative abundance of the dimer in the electrolyte indicates that it is the primary species involved in reversible Mg deposition. In addition, a Mg full-cell cycling mechanism of these electrolytes is proposed and discussed based on the present results and previous reports.

Introduction

Electrochemical deposition of Mg can be dated to the 1920's based on organomagnesium precursors including Grignard type complexes.[1-2] Early development in 1971 by Berand *et al*.[3] and in 1990 by Gregory *et al*.[4] reported the enhanced electrochemical performance of organomagnesium compounds (MgR_2 or RMgCl) by using Al or B Lewis acid additives. Since then there have been continuous efforts in developing advanced Mg-Cl complex electrolytes for rechargeable Mg batteries by a number of groups,[5-7] which achieved reversible Mg cycling with less than 300 mV overpotential and greater than 3 V vs Mg anodic stability. A common $[(\mu\text{-Cl})_3Mg_2(THF)_6]^+$ dimer crystal structure in electrochemically active Mg-Cl complex electrolytes in THF was identified and believed to be an active species or the precursor to the active species for Mg cycling.[6-15] More recently, there were a variety of Mg-Cl complex electrolytes developed by us[16-20] and other groups[11, 21-43]. In addition, it is worth noting that there have been ongoing efforts in developing Cl-free electrolytes. Simple Mg salts including $Mg(TFSI)_2$ and $Mg(PF_6)_2$, where TFSI is bis(trifluoromethane)sulfonimide and PF_6 is hexafluorophosphate, perform poorly for reversible Mg deposition due to the instability of anions with Mg metal.[13, 44] MgCB[45-46] and MgB[47-49] salts were reported as rare examples of chloride-free electrolytes for reversible Mg deposition.

We have put our efforts into developing new Mg-Cl electrolytes with improved oxidation stability and electrophile compatibility by avoiding the use of reactive and nucleophilic Mg sources such as Grignard reagents or dialkyl magnesium.[16-17, 19-20, 50] Based on a simple retrosynthesis analysis on the common $[(\mu\text{-Cl})_3Mg_2(THF)_6]^+$ dimer structure (see Scheme 1), we rationalized and experimentally confirmed a facile approach

(termed as mono-Cl abstraction, Scheme 1) using $MgCl_2$ and an Al Lewis acid ($AlCl_3$, $AlEtCl_2$, and $AlPh_3$) to produce high performance Mg electrolytes. In contrast to the reported formulations using organometallic magnesium precursors with the corresponding Al Lewis acids, the $MgCl_2$ / $AlCl_3$ Lewis acid electrolytes are much more synthetically feasible in terms of the cost of the starting materials, purification requirements, and waste management with improved electrochemical performance. It should be noted that the all-inorganic $MgCl_2$ / $AlCl_3$ electrolyte represents the simplest Mg electrolyte formula to date and has attracted several other groups to study it experimentally[23-24, 29, 34, 43] and theoretically.[51] More recently, using Mg powder as a scavenger to address contaminating issues of water and other deleterious impurities,[18, 52] we developed a series of ternary Mg / $MgCl_2$ / $AlCl_3$ electrolytes in THF, DME, and diglyme (termed MMAC electrolytes), which demonstrated outstanding electrochemical performance with Coulombic efficiency up to 100%, overpotential less 220 mV, and anodic stability up to 3.8 V vs Mg.[19]

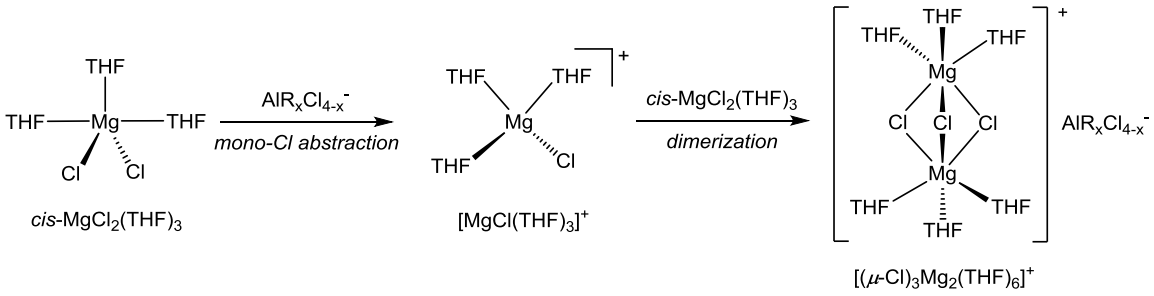

Scheme 2-1. Previously proposed mono-chloride abstraction and dimerization of $MgCl_2$ / $AlCl_3$ electrolyte in THF solution.[17]

For the popular dimer electrolytes, $[(\mu\text{-Cl})_3Mg_2(THF)_6]^+$ dimer was proposed to be in equilibrium with $MgCl_2(THF)_3$ and $[MgCl(THF)_3]^+$.[16, 50, 53] It remains in debate whether

the dimer or the monomeric $[MgCl(THF)_5]^+$ is the active species responsible for electrochemical Mg cycling.[6, 16, 18, 54-55] However, there are very limited experimental studies to examine the chemical constituents of the dimer electrolytes in the solution phase. One major challenge is the dynamic behaviors of labile THF coordination with Mg^{2+} cation, and thus, it is difficult to apply a suitable spectroscopic tool to pinpoint individual molecular species in the electrolyte solution. Arthur *et al*. applied XAS studies to show that the dominant cation species in Mg-Cl complex electrolytes including EtMgCl / Et_2AlCl and $[(\mu\text{-}Cl)_3Mg_2(THF)_6][AlCl_4]_2$ is the dimer.[56] We have reported the use of a soft mass spectrometry technique to identify a $[MgCl(THF)_3]^+$ species present in the $[(\mu\text{-}Cl)_3Mg_2(THF)_6]^+$ dimer electrolyte, providing the first experimental indication for the mononuclear $[MgCl]^+$ species in the electrolyte solution.[16] Sa *et al*. reported the detection of the dimer species using mass spectrometry in the $MgCl_2$ / $Mg(TFSI)_2$ (2:1 ratio) electrolyte in THF.[38] Andrew *et al*. suggested the existence of the $[(\mu\text{-}Cl)_3Mg_2(THF)_6]^+$ dimer in the $MgCl_2$ / $AlCl_3$ solution through X-ray pair distribution function (PDF) analysis.[57] The above experimental results are inspiring, but do not definitively elucidate the solution nature of the $[(\mu\text{-}Cl)_3Mg_2(THF)_6]^+$ dimer electrolyte. In short, we still lack a full picture on the solution species of the Mg dimer electrolyte. Herein, we report an investigation of this system using a DFT computational approach. In addition to further understanding experimental results, DFT calculations can provide insights into the most prevalent Mg species in solution and shed light on the active species participating in Mg battery cycling.

During the time of this computational work, Canepa *et al.* published DFT studies aimed at elucidating the structure and solvation chemistry of Mg-Cl complexes in THF at

the B3LYP level of theory.[54] Their results concluded that the Mg dimer and trimer are only formed in solution upon solvent evaporation, however, the most dominant monochloride Mg-Cl species in solution is $[MgCl(THF)_3]^+$, and finally, the most dominant dichloride Mg-Cl species is $MgCl_2(THF)_2$. However, there are several factors that give rise to considerable uncertainty with these results. The first being that B3LYP is well known to give unreliable results for calculations concerning thermodynamic data such as Gibbs free energies of reaction or solvation.[58] Selecting an appropriate, cost-effective functional is no trivial task. It is no surprise that methods are selected by others simply based on popularity but deemed outdated in the theoretical community.[58-60] Other concerns for these results lie in how the calculations were modeled. In the previous work, the structures were optimized (relaxed) in the gas phase, and a THF solvent correction using the continuous polarizable model (CPM) was done on the gas-phase relaxed structures to model solvated molecules. However, considerable error is introduced using this method since the geometry of these structures differ significantly to those optimized directly in the implicit THF solvent instead of the gas phase. This was most likely done due to the complications that arise from optimizing geometries during self-consistent reaction field (SCRF) calculations. Furthermore, performing such optimizations in the solvent phase can dramatically increase computational cost as well as give various convergence issues. As shown in this study, we determined the more expensive computations were necessary to examine this system in more scrutinous detail using a different, more suitable theoretical method. This report demonstrates how the level of theory can significantly affect conclusions derived from such solvation studies. Furthermore, we have determined that both the solvation process and the most stable Mg-Cl species largely depend on the interaction of the Al Lewis acid.

Therefore, it is essential for this study to gain a better understanding of not only the structure of $AlCl_3$ in THF, but also consider the free energy pathways of the combinations of the solvated Mg-Cl complexes and the solvated Lewis acids in order to provide evidence for the true Mg-Cl active species present in such electrochemical systems.

In this study, we adopted the M06-2x functional with 6-31+G(d) basis set and SMD solvation model to elucidate the solution chemistry of the Mg electrolytes. Our DFT study provides comprehensive results to: 1) elucidate the chemical nature of the $MgCl_2$ / $AlCl_3$ electrolyte in solution; 2) offer a systematic evaluation of structural isomers of both compounds in THF, which has never been done before; and 3) gain a better computational understanding of the solvation and structural chemistry of the aluminum chloride Lewis acid in THF, giving valuable insights to previous experimental works done on this system[21-25]. Consistent with experimental results[56], but contrary to previous DFT results[54, 61], our comprehensive DFT calculations on THF solvation, isomerization, chloration, and dimerization of possible Mg-Cl species reveal that the $[(\mu\text{-}Cl)_3Mg_2(THF)_6]^+$ dimer is the most dominant Mg-Cl species in solution, but is unlikely to be the active species involved in charge transfer at the anode. Additionally, a comprehensive diagram has been proposed for the Mg battery cycling in the $MgCl_2$ / $AlCl_3$ in THF system based on the results herein and other reports. The presented study on the coordination chemistry of the Mg-dimer electrolytes will inspire designing the next generation of Mg electrolytes.

Experimental

Computational Methods. Calculations of the Mg and Al Lewis acid systems were performed using the Gaussian 09 package.[62] The molecules and complexes were modeled

as isolated molecules at 298.15 K, unless specified otherwise. The electron correlation method was calculated using M06-2x[60] functional, Minnesota '06 2x global hybrid functional with 54% Hartree-Fock exchange, with a basis set of 6-31+G(d)[63-64]. The M06-2x functional has been shown to be a more suitable choice for calculations involving thermodynamic data in main group elements and significantly outperforms B3LYP when involved in coordination chemistry of organometallics.[65-67] Therefore, the M06-2x method was used instead of B3LYP since it has been well established that M06-2x has a much better correlation to experimental data involving main group elements, especially when thermodynamic data is considered.[4, 58, 66-67] An ultrafine integration grid was used to increase the accuracy of all calculations. Real minima were confirmed for all optimized geometries by verifying the absence of negative frequencies using Chemcraft visualization software.

The molecular geometries were relaxed in the implicit THF solvent using SMD[68] at the M06-2x / 6-31+G(d) level of theory. While it is known that one can use a gas-phase optimized structure in the single-point calculation with the SCRF calculation to decrease computational cost at the expense of some intrinsic error, one should use caution when using such a method as the magnitude of this error increases with molecule size and decreases with rigidity since the dielectric reaction field can impose significant geometrical changes due to differences of thermal motion (*e.g.*, vibrational frequencies) in solution.[69-70] In the case of comparing the solvation coordination of molecules and ions as described here and in other related systems[54], the target molecules used for relative comparison are both increasing in size and have varying degrees of rigidity. This can lead to significant computational error that can potentially change the outcome of solvated species without

solvent optimization. Therefore, it was deemed necessary to use the solvent-optimized geometries for free energy of solvation calculations to explicitly account for these geometrical and vibrational differences.

Solvation of Mg and Al Complexes in THF. To gain understanding of the chemical equilibrium of the Mg dimer in the presence or absence of external Cl^-, comprehensive DFT calculations were conducted to obtain thermodynamic data such as Gibbs free energies for various Mg species. To increase computation accuracy, all geometries were optimized in the THF solvent implicitly using the SMD[68] solvation model with the basis set of 6-31+G(d)[63-64] and the M06-2x[60] functional. The energy minimum of each optimized structure was confirmed by checking for the absence of negative vibrational frequencies which indicate false minima. THF molecules were added to each Mg-Cl or Al-Cl complex one at a time (explicitly) until fully coordinated (*i.e.*, six ligands for each metal center) while considering all isomers.

Results

Solvation Chemistry of $MgCl_2$. For the formation of the $[(\mu\text{-}Cl)_3Mg_2(THF)_6][AlCl_4]$ dimer electrolyte, the $MgCl_2$ reactant is the Mg precursor. Thus, the solvation chemistry of $MgCl_2$ in THF was modeled by adding THF molecules for coordination one at a time in THF solvent until fully coordinated with $MgCl_2$, as seen in Scheme 2-2 where the free energies of reaction are given in kcal/mol. Solvation of $MgCl_2$ with one THF to form $MgCl_2(THF)$ gives a large free energy of reaction of -12.61 kcal/mol, which is reasonable since solvation of solid $MgCl_2$ is highly spontaneous. Adding another THF to form $MgCl_2(THF)_2$ leads to a tetrahedral geometry at a favorable free energy of

-12.11 kcal/mol. Further solvation of the tetrahedral monomer can form two isomers, *cis* or *trans*, of which six different minima were found. To distinguish between the square planar and trigonal bipyramidal geometries, the geometry index was calculated based on the two greatest bonding angles within each found minima as described in Addison's work.[71] Values below 0.5 indicate geometries closer to square planar and above 0.5 are closer to trigonal bipyramidal. The most favorable isomer is the *e,e-cis-tbp*-$MgCl_2(THF)_3$ (I) species where both chloride ligands are in the equatorial position with a free energy of -3.08 kcal/mol. However, the *a,a-trans-tbp*-$MgCl_2(THF)_3$ isomer could not be optimized with the M06-2x functional since this conformation freely decayed to the *e,e-cis-tbp*-$MgCl_2(THF)_3$ (I) geometry. Therefore, *a,a-trans-tbp*-$MgCl_2(THF)_3$ was optimized at the B3LYP level with all other parameters and basis set kept the same as the other calculations followed by a single point calculation with the M06-2x theory. The *a,a-trans-tbp*-$MgCl_2(THF)_3$ isomer was calculated to be the least favorable by 7.15 kcal/mol. This is consistent with the other observed minima where the free energies were less favorable when the geometry index was close to 1 or 0 (*i.e.*, fully trigonal bipyramidal or fully square planar). The structure becomes most relaxed when the geometries are between the indices of 0.5 to 0.7 giving the least amount of steric hinderance from the bulky THF ligands.

Further solvation of the more stable *e,e-cis-tbp*-$MgCl_2(THF)_3$ (I) geometry leads to two fully coordinated octahedral *cis* and *trans* isomers. Both isomers were found to solvate unfavorably by 5.28 kcal/mol for the *trans* and 4.70 kcal/mol for the *cis* being the more stable of the two.

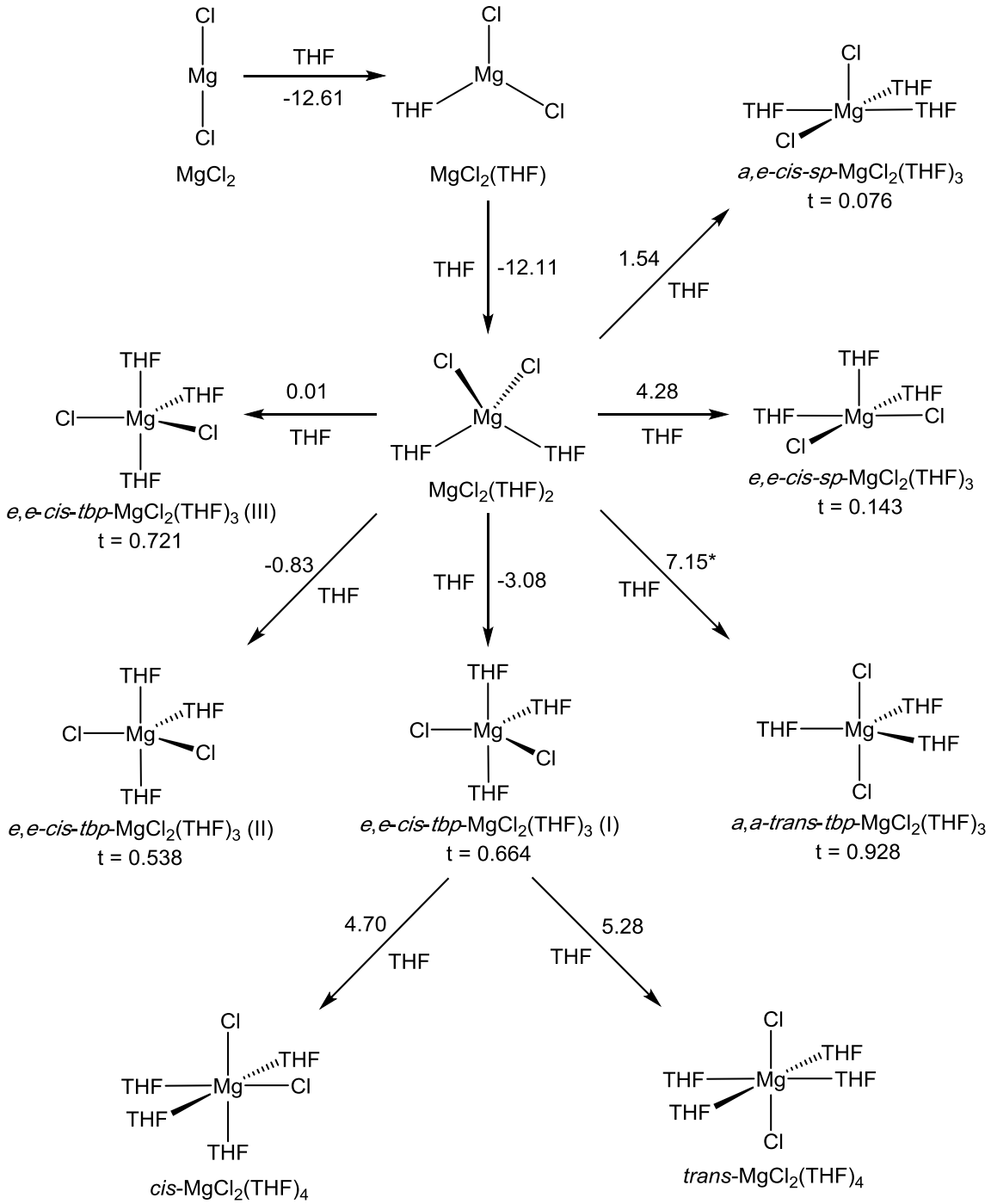

Scheme 2-2. Solvation of $MgCl_2$ species in THF. Free energies given in kcal/mol. Free energies marked with an asterisk involved optimization of the product at the B3LYP / 6-31+G(d) / SMD level followed by a single point calculation at the M06-2x / 6-31+G(d) / SMD level.

Hence, the DFT results suggests *e,e-cis-tbp*-$MgCl_2(THF)_3$ (I) is the most populated solvated $MgCl_2$ species and will be the conformation considered in further calculations. These results are qualitatively consistent with previously DFT results reported by Burk *et al.*[72] using B3LYP functional with a 6-31+G(d) basis set but different from what was reported by others.[54, 61] In the DFT studies reported by Wan[61] and Ceder[54] performed at the PBE and B3LYP levels, respectively, structural isomerization was not considered of various Mg-Cl and Al-Cl species. In chemistry, it is commonly known structural isomers can have distinguished free energies, and thus, present other viable avenues for which a Mg-Cl dimer could be formed in THF solution.

Solvation Chemistry of $[MgCl]^+$ Species. As previously proposed,[16] *e,e-cis-tbp*-$MgCl_2(THF)_3$ (I) needs to undergo mono-Cl abstract with a Lewis acid such as $AlCl_3$ to form THF solvated $[MgCl]^+$ species to form the dimer, $[(\mu\text{-}Cl)_3Mg_2(THF)_6]^+$. Therefore, Mg monochloride species were considered to characterize relevant reactions. The solvation of $[MgCl]^+$ in THF is shown in Scheme 2-3 as a step-wise process. Adding a THF to $[MgCl]^+$ to form the linear $[MgCl(THF)]^+$ is highly spontaneous by -13.87 kcal/mol. Addition of another THF to form the trigonal planar $[MgCl(THF)_2]^+$ species experiences a similar thermodynamic favorability of -14.89 kcal/mol, and one more THF forms the tetrahedral $[MgCl(THF)_3]^+$ at -16.74 kcal/mol. Further solvation of the tetrahedral monomer formed five isomers with the chloride either in the *axial* position or the *equatorial* position. Addison's geometry index was used to distinguish between square pyramidal and trigonal bipyramidal isomers.[71] The most favorable isomer is *a-sp*-$[MgCl(THF)_4]^+$ with a free energy of -7.86 kcal/mol where the Mg atom is left with a vacant site.

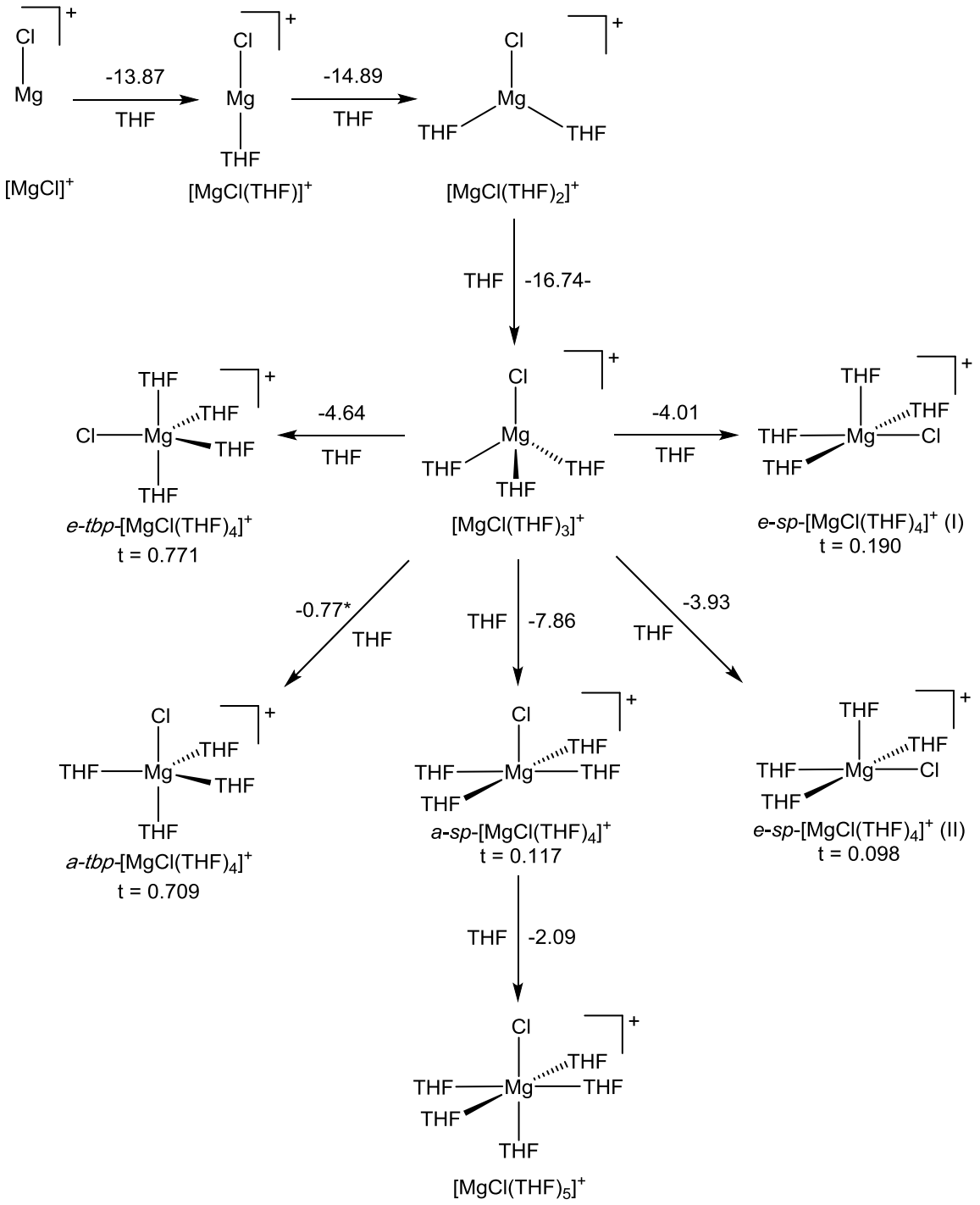

Scheme 2-3. Solvation of $[MgCl]^+$ species in THF. Free energies in kcal/mol. Free energies marked with an asterisk involved optimization of the product at the B3LYP / 6-31+G(d) / SMD level followed by a single point calculation at the M06-2x / 6-31+G(d) / SMD level.

The *a-tbp*-$[MgCl(THF)_4]^+$ isomer could not be optimized with the M06-2x functional since this isomer freely decayed to the *a-sp*-$[MgCl(THF)_4]^+$ square pyramidal geometry. Therefore, it was optimized at the B3LYP level with all other parameters kept the same as previous calculations followed by a single point calculation at the M06-2x level of theory. This isomer was calculated to be the least favorable by -0.77 kcal/mol. Moving from the *axial* square pyramidal geometry of *a-sp*-$[MgCl(THF)_4]^+$ to form the octahedral six-coordinate species $[MgCl(THF)_5]^+$ is favorable by -2.09 kcal/mol. Hence, the octahedral six-coordinate, fully-coordinate-saturated species is the most populated Mg monochloride species in THF solution. According to these DFT calculations results, removal of one chloride from *e,e-cis-tbp*-$MgCl_2(THF)_3$ (I) yields $[MgCl(THF)_3]^+$ species as the product, which will experience further solvation to form more stable $[MgCl(THF)_5]^+$. Further solvation forms two interesting *axial*- and *equatorial*-square pyramidal isomers with free energies of -7.86 kcal/mol and -4.01 kcal/mol, respectively, where the Mg atom is left with a vacant site. Adding THF to the *axial*-square pyramidal geometry of *a-sp*-$[MgCl(THF)_4]^+$ favorably forms the octahedral six-coordinate species $[MgCl(THF)_5]^+$ at -2.09 kcal/mol. Hence, the octahedral six-coordinate species is the most populated Mg monochloride species in THF solution. According to these DFT calculations results, removal of one chloride from *e,e-cis-tbp*-$MgCl_2(THF)_3$ (I) yields $[MgCl(THF)_3]^+$ as the product which will undergo further solvation to form the more stable $[MgCl(THF)_5]^+$ species.

Solvation Chemistry of $AlCl_3$ in THF. Since $[MgCl(THF)_5]^+$ is essentially produced from the mono-Cl abstraction process in a Lewis acid battery, it is important to understand the reaction nature of the mono-Cl abstraction process between $MgCl_2(THF)_3$ and a Lewis acid.[16] Here, $AlCl_3$ is explored for the mono-Cl abstraction, as it is a simple

Lewis acid to model and forms the well-known $MgCl_2$ / $AlCl_3$ fully inorganic electrolyte in the literature.[16-17, 24, 29, 34, 54] A detailed DFT analysis of the aluminum chloride in THF was performed to find the most stable solvated species to participate in the mono-Cl abstraction reaction. In addition to further understanding the active mono-chloride abstracting species for Mg-Cl electrolytes, a comprehensive DFT analysis on the complete equilibrium of all solvated $AlCl_3$-THF isomers may be of considerable interest since there has been much ambiguity and uncertainty in previous experimental studies due to the challenging nature of *in-situ* analysis and characterization.[17, 73-79] Thus, proposing the thermodynamics of reaction of all known isomers of $AlCl_3$ in THF by a free energies comparison may provide key insights and additional support to this system.

A study done in 1977 by Derouault, using ^1H NMR and Raman spectroscopy revealed $AlCl_3$ exists in various equilibria while in solution with THF to give $AlCl_3$(THF), $AlCl_3(THF)_2$, and $[AlCl_4][AlCl_2THF_4]$, all of the mixture of which is concentration and temperature dependent with $AlCl_3(THF)_2$ being the major species.[75-76] In attempts to further confirm these results, Cowley and co-workers in 1981 were able to only obtain the $AlCl_3(THF)_2$, however, using a slightly different system.[74] Means and Atwood in 1987 investigated the homolytic and heterolytic cleavage of the well-known Al_2Cl_6 solid dimer (solid $AlCl_3$) in THF and isolated Derouault's compound $[AlCl_4][AlCl_2(THF)_4]$ from toluene mixtures and verified using single crystal X-ray diffraction.[78] In 1990, Cotton predicted the $[AlCl_2(THF)_4]^+$ species was actually the $[AlCl_2(THF)_2]^+$ species.[73] Means' results also confirmed the presence of $AlCl_3(THF)_2$ isomers in the $AlCl_3$-THF solution, and Han in 1990 confirmed the presence of $AlCl_3(THF)_2$ and its two isomers, *cis*-$AlCl_3(THF)_2$ and *trans*-$AlCl_3(THF)_2$.[78] However, the relative abundance of each isomer has led to varied

results. According to the reported ^{27}Al NMR data from Derouault, the self-ionization of two $AlCl_3(THF)_2$ to $[AlCl_4][AlCl_2(THF)_4]$ is estimated have a dissociation constant of $K_{diss.}$ = 2.6 (± 0.3) x 10^{-3} (3.5 kcal/mol) at 24 °C and 0.5 M, as represented in Eq 1:

$$2\ \textit{trans}\text{-}AlCl_3(THF)_2 \rightleftharpoons [AlCl_4]^- + [AlCl_2(THF)_4]^+ \quad (1)$$

A more recent study in 1998, Lefebvre found the relative abundance of the ion pair to be *ca.* 15% by ^{27}Al NMR at 25 °C and 0.5 M, yielding a dissociation constant of $K_{diss.}$ = 4 (± 2) x 10^{-2} from which the free energy of dissociation can be calculated to be 1.9 kcal/mol. Derouault's underestimation of the dissociation constant is likely due to the older NMR technology where parameters such as acquisition time were not specified beyond the mention of a new LOCK system.[76, 79] It is more reasonable to assume Lefebvre's estimation as there was a detailed report of all used NMR parameters and using NMR technology two decades newer than Derouault's, the effects of which can be seen in the broadness of the $[AlCl_4]^-$ peak at 103 ppm in Derouault's study compared to that of Lefebvre's and Han's.[76-77, 79] This is important since equilibrium calculations are sensitive to proper acquisition times and shimming which allow nuclei to fully relax as well as to minimize overlapping of broad peaks, respectively, both of which can interfere with quantitative integration.

By comparing our DFT results with the experimental findings, we can establish the accuracy and predictive reliability of the computational model employed for these systems. Furthermore, a comparative DFT investigation adds further insight and support to previously varied studies. First, the thermodynamics of formation of the Al_2Cl_6 dimer was investigated, as this has not been studied by DFT until now. The free energy of dimerization was modeled by relaxing $AlCl_3$ in the gas phase, and sequentially, in a separate calculation, placing two of these optimized $AlCl_3$ monomer units in proximity to each other and

allowing the two to interact through self-consistent field (SCF) optimizations. The formation of the Al_2Cl_6 dimer in the gas phase was calculated to be a favorable process by -20.08 kcal/mol (Scheme 2-4). These DFT results support the experimental and other theoretical observations that gas-phase aluminum chloride exists as a dimer.[78, 80-81]

From the gas-phase Al_2Cl_6 dimer, the solvation process was investigated by first calculating the free energy of solvation in THF and subsequently adding THF molecules sequentially to the system. Through the optimization steps, it was observed that the more electron density THF donated to the Al centers (through the addition of more explicit THF molecules) the more the dimer separated into monomers. This is in good agreement with the experimentally observed cleavage products in the Lewis acid-base reaction of the Al_2Cl_6 dimer and THF[78, 80], and provides a good model through which solid-phase lattice sheets of polymeric Al_2Cl_6 can be cleaved by THF to the monomers in the solvation process of the solid.[82-83] According to the previous studies of $AlCl_3$ in THF, solvation of the Al_2Cl_6 dimer in THF leads to symmetrically cleaved $AlCl_3$, and asymmetrically cleaved $[AlCl_2]^+$ and $[AlCl_4]^-$ species.[78, 83]

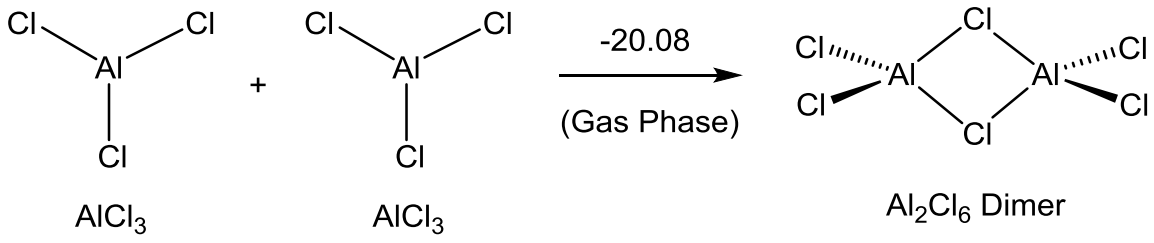

Scheme 2-4. Dimerization of aluminum chloride in the gas phase at 298.15 K. Free energies given in kcal/mol.

Therefore, to confirm the most stable Al-Cl species, the solvation process of both the symmetrically ($AlCl_3$) and asymmetrically ($[AlCl_2]^+$ and $[AlCl_4]^-$) cleaved aluminum chloride monomer species were investigated at the same computational level as the Mg-Cl species.

Solvation of $AlCl_3$ in THF was first modeled by the stepwise addition of THF ligands. The coordination of a THF molecule to the $AlCl_3$ monomer forms a tetrahedral geometry that is stabilized by -32.66 kcal/mol, as seen in Scheme 2-5.

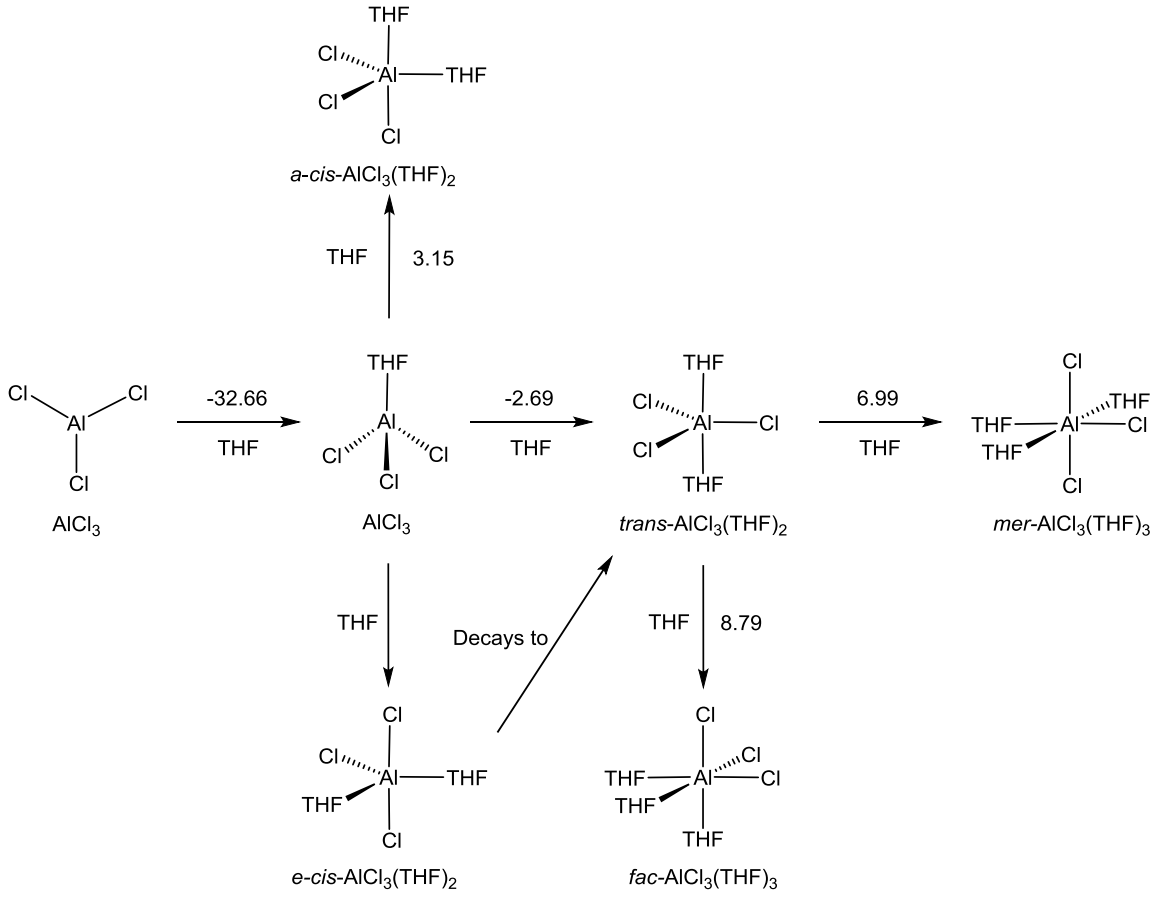

Scheme 2-5. Solvation of $AlCl_3$ in THF. Free energies given in kcal/mol.

Further solvation of $AlCl_3THF$ can potentially form three trigonal bipyramidal isomers, *trans*-$AlCl_3(THF)_2$, *e-cis*-$AlCl_3(THF)_2$ where the two THF ligands are in the equatorial plane, and *a-cis*-$AlCl_3(THF)_2$ where the two THF ligands are orthogonal. The *trans* isomer, *trans*-$AlCl_3(THF)_2$, was the most thermodynamically stable aluminum trichloride species by -2.69 kcal/mol; a thermodynamic equilibrium that confirms Derouault's and Cowley's findings.[74-76] However, for the other two possible isomers, only *a-cis*-$AlCl_3(THF)_2$ minima could be found with an unfavorable free energy of 3.15 kcal/mol. The initial *e-cis*-$AlCl_3(THF)_2$ structure, due to steric repulsion factors, tended to decay to the *trans* configuration which indicates the most stable isomer is indeed *trans*-$AlCl_3(THF)_2$. Further coordination of THF resulted in unfavorable solvation of 6.99 kcal/mol for the *mer*-$AlCl_3(THF)_3$ and 8.79 kcal/mol for the *fac*-$AlCl_3(THF)_3$ isomers.

Asymmetric cleavage of aluminum chloride results in two ionic species, a $[AlCl_2]^+$ cation and a $[AlCl_4]^-$ anion. The dichloroaluminum cation undergoes favorable solvation in THF as shown in Scheme 2-6. Allowing a single THF molecule to coordinate to an $[AlCl_2]^+$ monomer is highly favorable by -66.49 kcal/mol forming a trigonal planar species. The second coordination of THF forms a favorable tetrahedral geometry by -40.72 kcal/mol. Further solvation leads to either an *axial-cis* or an *equatorial-cis* trigonal bipyramidal structure with a free energy of -1.45 and -8.36 kcal/mol, respectively. A local minima could not be found for the *trans* species as the steric repulsion was too great for the bulkier THF ligands to withstand being in the same plane, thus, spontaneously decaying to the more stable *equatorial-cis* configuration.

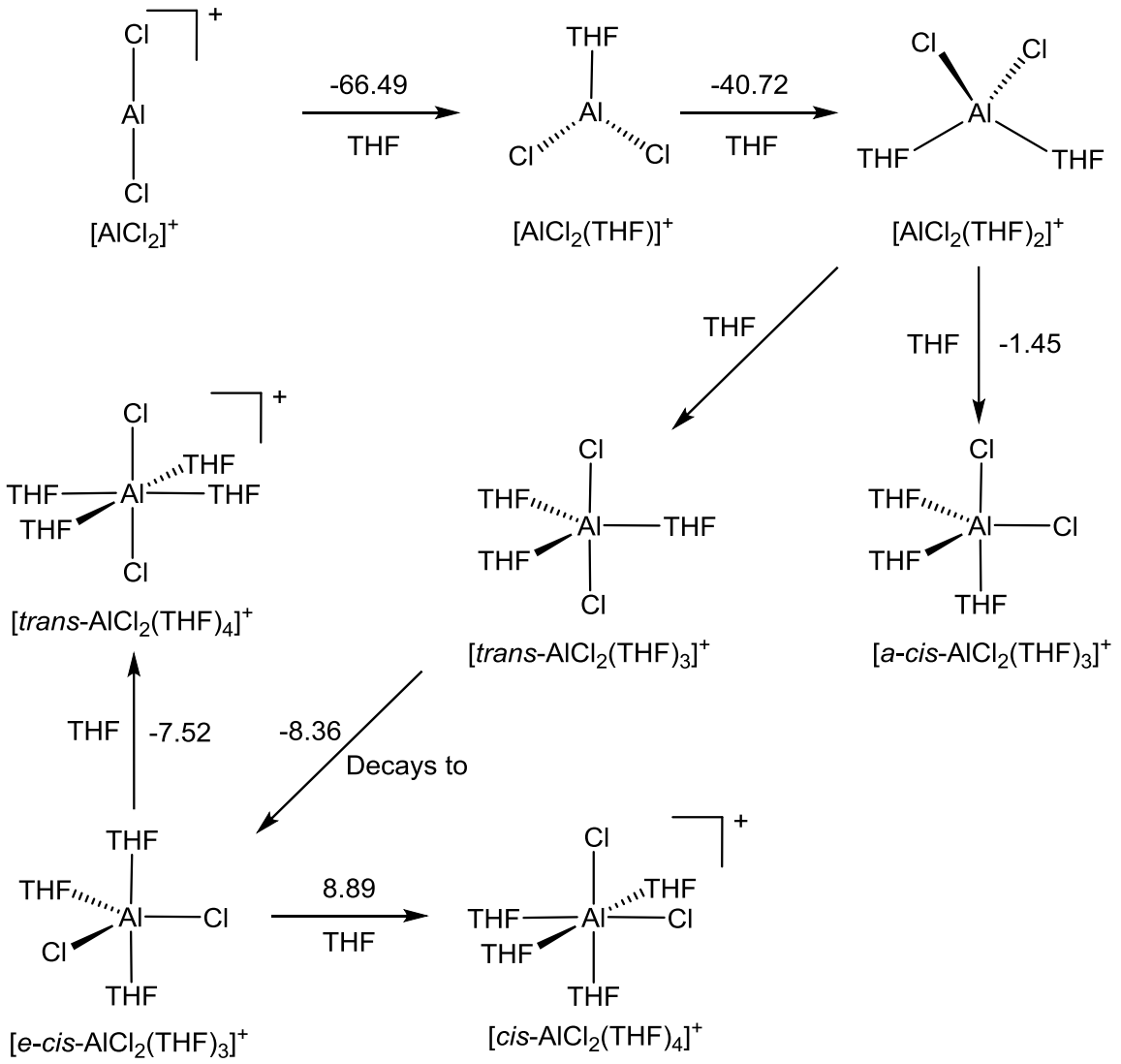

Scheme 2-6. Solvation of $[AlCl_2]^+$ in THF. Free energies in kcal/mol.

The coordination of a fourth THF molecule leads to two isomers with $[cis\text{-}AlCl_2(THF)_4]^+$ being 8.89 kcal/mol uphill and $[trans\text{-}AlCl_2(THF)_4]^+$ being -7.52 kcal/mol downhill, hence suggesting the fully coordinated *trans* aluminum dichloride cation to be the most stable solvated species for asymmetric cleavage. This data is in good agreement with Means' results on the dissolution of aluminum chloride in THF where the $[trans\text{-}AlCl_2(THF)_4]^+$ species was shown to be the most populated cationic species compared to the four-

coordinated [*trans*-$AlCl_2(THF)_2]^+$, unlike Cotton's predictions.[73, 78] Moreover, the geometry of the dichloroaluminum species matched that of Means' single crystal structure of [*trans*-$AlCl_2(THF)_4]^+$ where the coordinated THF molecules were in a symmetric propeller-type orientation[78], giving further evidence of the predictive power to the computational of the method used herein. The tetrachloroaluminum anion did not undergo further coordination with THF. This is expected since the electron density around the aluminum center is saturated due to the four coordinating chloride anions making further donation of electron density from THF unfavorable. Further solvation of $[AlCl_4]^-$ to [*trans*-$AlCl_4(THF)]^-$ was verified in Scheme 2-7 to be highly unfavorable by 10.14 kcal/mol.

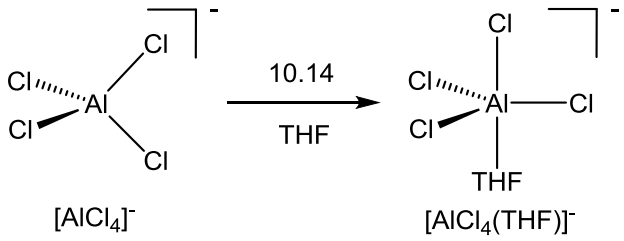

Scheme 2-7. Solvation of $[AlCl_4]^-$ in THF. Free energies in kcal/mol.

Evaluating the overall solvation of the Al-Cl dimer based on the free energies suggests the symmetrically cleaved product, *trans*-$AlCl_3(THF)_2$, is the most abundant species in THF solution. This species is stabilized by -56.02 kcal/mol while the asymmetrically cleaved species, [*trans*-$AlCl_2(THF)_4]^+$ and $[AlCl_4]^-$, is slightly less favorable at -54.75 kcal/mol, as shown in Scheme 2-8.

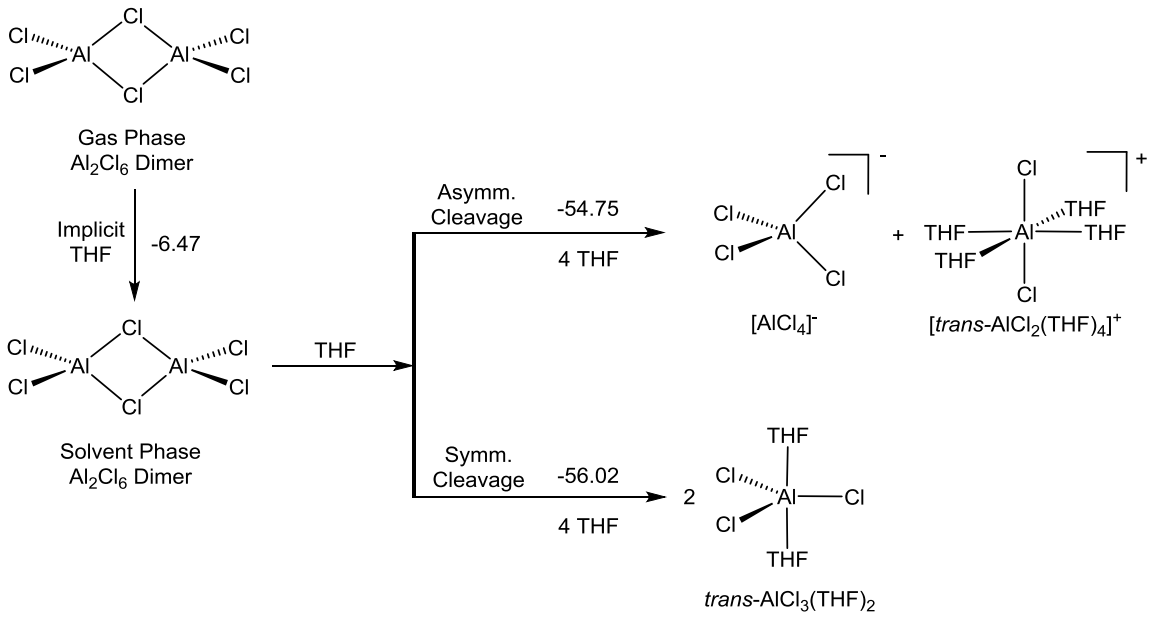

Scheme 2-8. Solvation and cleavage of the aluminum chloride dimer in THF. Free energies given in kcal/mol.

The small difference in free energies of 1.27 kcal/mol indicates coexistence of [*trans*-$AlCl_2(THF)_4]^+$, $[AlCl_4]^-$, and *trans*-$AlCl_3(THF)_2$ in an equilibrium. Qualitatively, these DFT results are consistent with the above-mentioned experimental observations of $AlCl_3$ in THF in concluding the correct major species.[74-76, 78-79] Quantitatively, these predictions are in excellent agreement to Lefebvre's experimental determination of the equilibrium constant at 0.5 M and 298 K (that is, *ca*. 15% relative abundance for the ionic pair, $K_{diss.} = 4 (\pm 2) \times 10^{-2}$, and $\Delta G_{diss.} = 1.9$ kcal/mol); while the theoretical results produced here are within 0.6 kcal/mol giving $K_{diss.} = 1 \times 10^{-1}$, *ca*. 25% relative abundance for the formation of the *trans*-$AlCl_3(THF)_2$ and the $[AlCl_4]$[*trans*-$AlCl_2(THF)_4$] ionic pair.[79] Temperature dependent studies also show that self-ionization is decreased with the increase of temperature.[76] The enthalpy of reaction, ΔH_r, for self-ionization was calculated to be

exothermic at a reasonable -1.42 kcal/mol, indicating that decreased temperature will favor the ionic pair, consistent with Derouault's findings.[76]

Mg-Cl and Al-Cl Lewis Acid-Base Reactions. Determining the most thermodynamically stable THF solvated products of both Mg-Cl complexes and Al-Cl complexes allows for a comprehensive study of Cl^- transfer reactions between them. The most relevant reaction regarding the formation of the $[(\mu\text{-Cl})_3Mg_2(THF)_6]^+$ dimer is between *e,e-cis-tbp*-$MgCl_2(THF)_3$ (I) and *trans*-$AlCl_3(THF)_2$, shown in Scheme 2-9. The mono-Cl abstraction between *e,e-cis-tbp*-$MgCl_2(THF)_3$ (I) and *trans*-$AlCl_3(THF)_2$ to generate $[MgCl(THF)_5]^+$ has a change in free energies of 4.41 kcal/mol. Mono-Cl abstraction of *e,e-cis-tbp*-$MgCl_2(THF)_3$ (I) by [*trans*-$AlCl_2(THF)_4]^+$ to give $[MgCl(THF)_5]^+$ and *trans*-$AlCl_3(THF)_2$ is uphill by 3.14 kcal/mol. Initially, these results indicate that the dimerization reaction is unable to occur. However, due to the large energy of dimerization between *e,e-cis-tbp*-$MgCl_2(THF)_3$ (I) and $[MgCl(THF)_5]^+$, the mono-Cl reaction can be driven by this equilibrium (see discussion below in the section of Formation of the $[(\mu\text{-Cl})_3Mg_2(THF)_6]^+$ Dimer).

Further mono-Cl abstraction of $[MgCl(THF)_5]^+$ by *trans*-$AlCl_3(THF)_2$ reveals a significant uphill free energy of 11.26 kcal/mol (Scheme 2-10). These results suggest that the formation of $[MgCl(THF)_5]^+$ from either *trans*-$AlCl_3(THF)_2$ or [*trans*-$AlCl_2(THF)_4]^+$ is qualitatively comparable. While *trans*-$AlCl_3(THF)_2$ is more populated than *trans*-$[AlCl_2(THF)_4]^+$, the data suggests that [*trans*-$AlCl_2(THF)_4]^+$ is the more active Lewis acid for the mono-Cl abstraction for *e,e-cis-tbp*-$MgCl_2(THF)_3$ (I), which is consistent with the greater Lewis-acidic nature of the more electron-deficient [*trans*-$AlCl_2(THF)_4]^+$ species. Additionally, it is a reasonable suggestion as experimental work shows the

[*trans*-$AlCl_2(THF)_4$][AlCl4] ion pair is in solution at a considerable *ca*. 15% via ^{27}Al NMR, and will continually replenish itself through self-ionization of the *trans*-$AlCl_3(THF)_2$ complex via Le Chatelier's principle.[78-79]

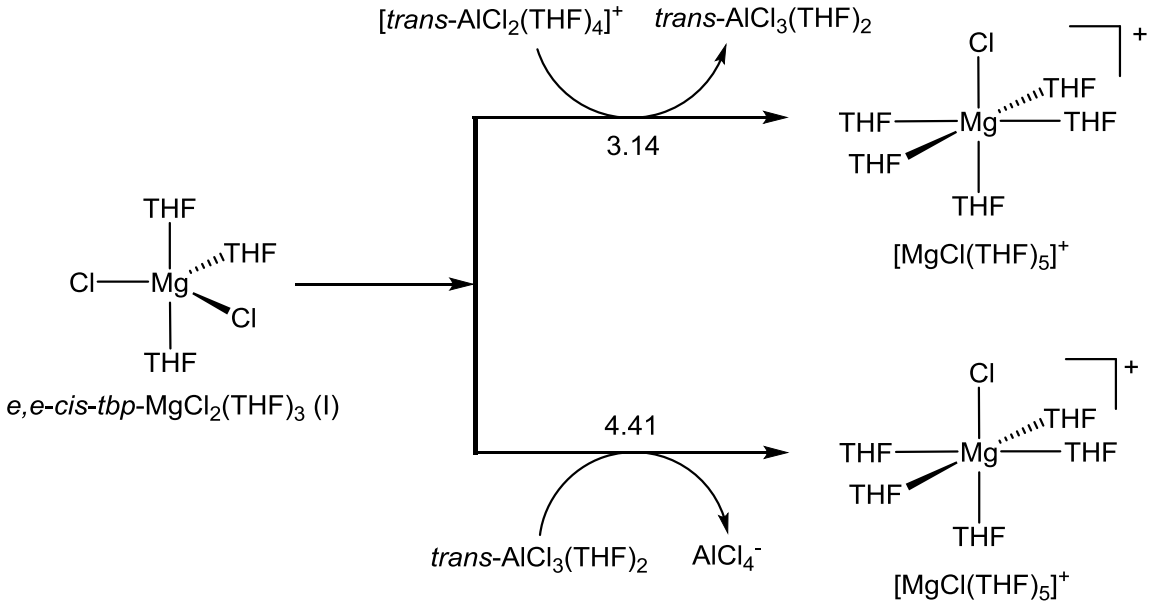

Scheme 2-9. Mono-chloride abstraction of *e,e-cis-tbp*-$MgCl_2(THF)_3$ (I) via the two major aluminum chloride species in solution. Free energies given in kcal/mol.

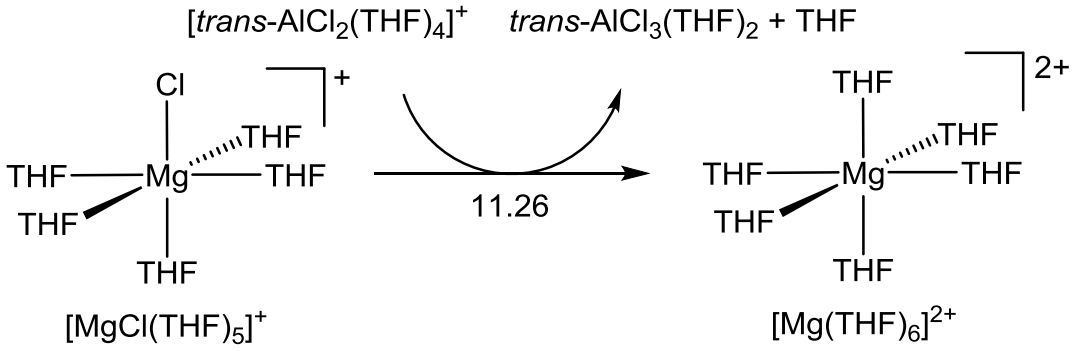

Scheme 2-10. Further mono-chloride abstraction from the $[MgCl(THF)_5]^+$ species. Free energies in kcal/mol.

Solvation of Various Dimers and Trimers. In order to achieve a comprehensive understanding of the complex equilibria of Mg-Cl / Al-Cl in THF and possible active stripping/deposition species, the thermodynamics of solvation of theorized dimers[61] and trimers[24] were studied, as shown in Scheme 2-11. Starting with the simplest stable dimer, $[(\mu\text{-Cl})_2\text{Mg}_2]^{2+}$, sequential additions of two THF molecules until coordinately saturated gave favorable reactions of -29.72, -34.28, -25.64, and finally reaching saturation at -4.28 kcal/mol. Of the dichloro-bridging dimers, $[(\mu\text{-Cl})_2\text{Mg}_2(\text{THF})_8]^{2+}$ is the most favorable in THF solution. For the more common trichloro-bridging dimers, $[(\mu\text{-Cl})_3\text{Mg}_2]^{+}$, stepwise additions of two THF molecules gave free energy differences of -29.03, -24.31, and -20.53 kcal/mol. Hence, the six-coordinate, $[(\mu\text{-Cl})_3\text{Mg}_2(\text{THF})_6]^{+}$, was theorized to be highly favorable over the $[(\mu\text{-Cl})_3\text{Mg}_2(\text{THF})_4]^{+}$ dimer by -20.53 kcal/mol, consistent with the experimental observations found in solution and crystallized products.[6, 54] Solvation of the bare $[(\mu\text{-Cl})_5\text{Mg}_3]^{+}$ cation by incremental additions by three THF molecules gave highly favorable free energies at -45.93 kcal/mol for the first step and -40.71 kcal/mol for the second, revealing the $[(\mu\text{-Cl})_5\text{Mg}_3(\text{THF})_6]^{+}$ species as the most stable solvated trimer.

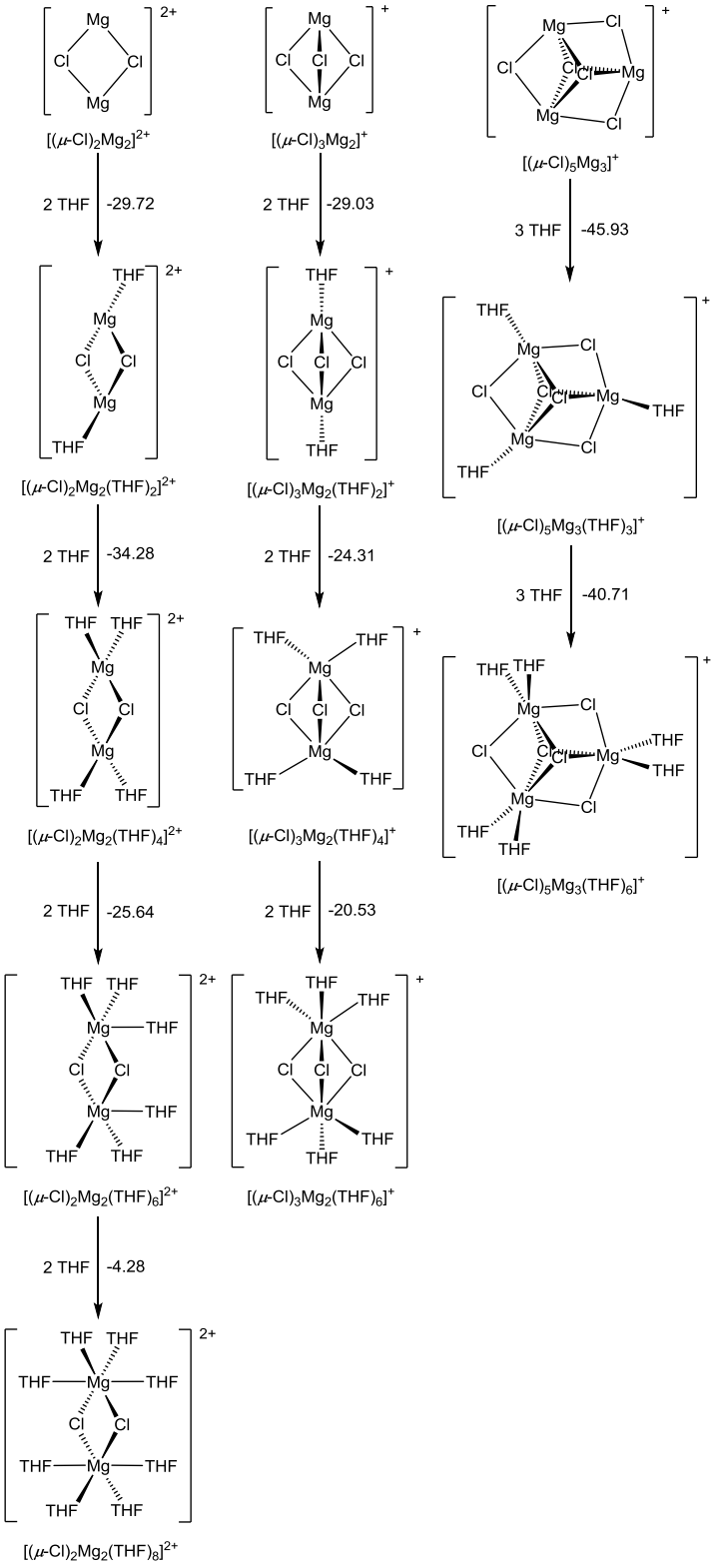

Scheme 2-11. Solvation of the two common Mg-Cl dimers and the Mg-Cl trimer by the stepwise addition of THF. Free energies in kcal/mol.

Formation of the $[(\mu\text{-Cl})_3Mg_2(THF)_6]^+$ Dimer. The formation of dimerization was then considered to compare the overall thermodynamics of such reaction in THF. Dimerization is statistically expected to form by combination of the two most populated $[MgCl]^+$ and $MgCl_2$ species in solution. Access to the Mg monochloride species through the proposed monochloride abstraction of the *e,e-cis-tbp*-$MgCl_2(THF)_3$ (I) species allows dimerization to the $[(\mu\text{-Cl})_3Mg_2(THF)_6]^+$ species. As shown in Scheme 2-12, formation of the dimer from $MgCl_2(THF)_3$ and $[MgCl(THF)_5]^+$ is substantially spontaneous by -6.30 kcal/mol, which accounts for why the dimer has been commonly observed in single crystal XRD studies and is also consistent with other spectroscopic studies.[56-57]

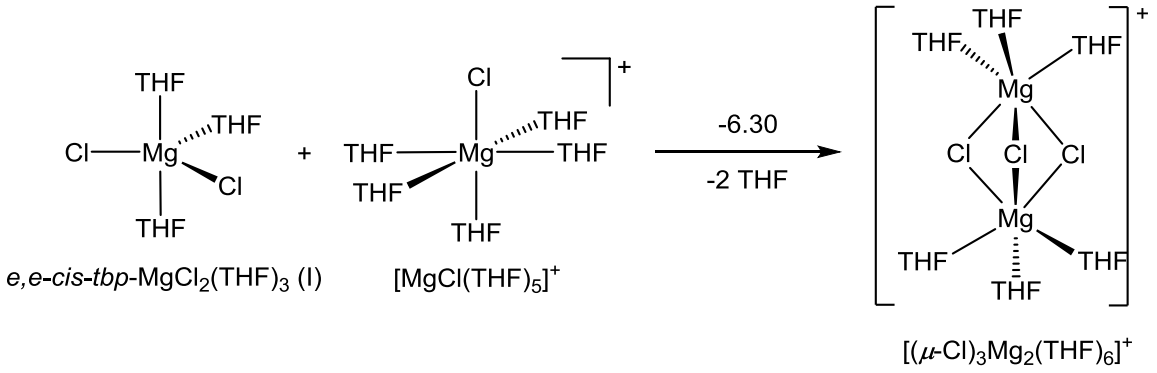

Scheme 2-12. Reaction of the most thermodynamically favorable dichloride and monochloride Mg-Cl species to form the $[(\mu\text{-Cl})_3Mg_2(THF)_6]^+$ dimer. Free energies in kcal/mol.

Formation of the $[(\mu\text{-Cl})_2Mg_2(THF)_8]^{2+}$ Dimer. The thermodynamic favorability of forming the dimer with two bridging chlorides was calculated from the combination of two *e,e-cis-tbp*-$MgCl_2(THF)_3$ (I) species that have both undergone mono-Cl abstraction. The free energy of reaction for the $[(\mu\text{-Cl})_2Mg_2(THF)_8]^{2+}$ dimer from two $[MgCl(THF)_5]^+$

monomers is an unfavorable process by 10.90 kcal/mol, as shown in Scheme 2-13. The $[(\mu\text{-Cl})_2Mg_2(THF)_8]^{2+}$ dimer was calculated to be the least favorable of the observed dimers. This is probably due to the formation of a highly-charged +2 species in comparison to the singly-charged tri-chloride bridging dimer or the trimer.

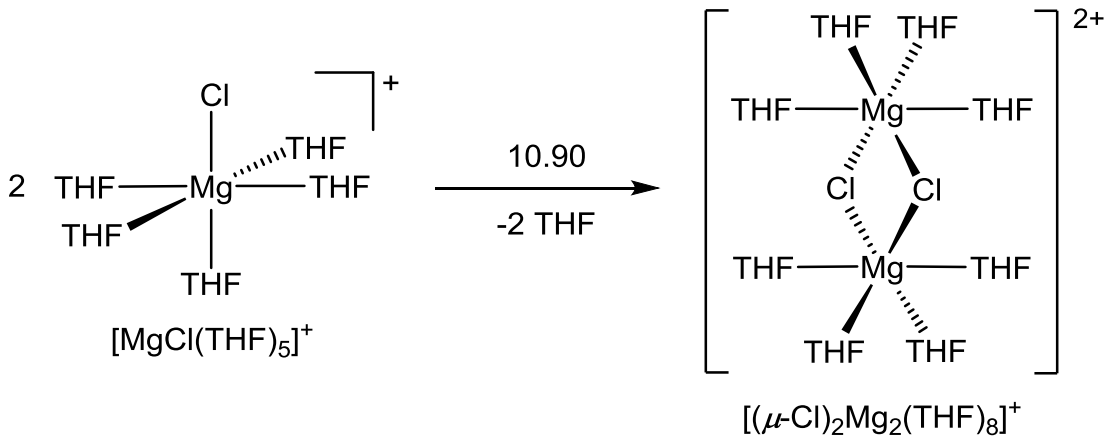

Scheme 2-13. Formation of the $[(\mu\text{-Cl})_2Mg_2(THF)_8]^{2+}$ dimer. Free energies in kcal/mol.

Formation of the $[(\mu\text{-Cl})_5Mg_3(THF)_6]^+$ Trimer. Trimerization through interaction between the $[(\mu\text{-Cl})_3Mg_2(THF)_6]^+$ dimer and the *e,e-cis-tbp*-$MgCl_2(THF)_3$ (I) monomer is an unfavorable process by 4.18 kcal/mol, as seen in Scheme 2-14. Termolecular reactions of monomers were disregarded as these are highly improbable. According to the free energies of reaction, it is therefore assumed that $[(\mu\text{-Cl})_3Mg_2(THF)_6]^+$ is the most favorable dimer of the potential dimers or trimers that can be formed in THF solution.

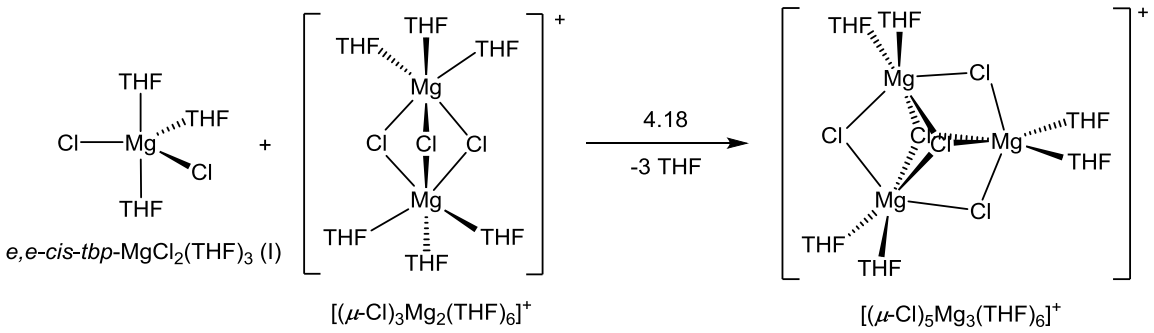

Scheme 2-14. Formation of the $[(\mu\text{-Cl})_5Mg_3(THF)_6]^+$ trimer. Free energies in kcal/mol.

Validation of Method. It is important to compare the accuracy of the selected DFT method to experimental observations in order to establish the validity of a method. In addition to the overarching comparisons throughout this text to other studies, we used a two-pronged approach: one for the Al-Cl system and another for the Mg-Cl system. Our method is in excellent agreement with Lefebvre's measurement of the self-ionization of aluminum chloride in THF with a small deviance of 0.6 kcal/mol, as previously discussed. The Mg-Cl chemistry is more complex as the structural characterization of solution-phase complexes remains an issue. Therefore, Table 2-1 compares the bond lengths of the optimized structures to X-ray crystallographic data from obtained crystal of several known structures. Not only are the bond-lengths in good agreement, but the predicted orientation of the coordinated THF molecules match the structures as well.

Table 2-1. Structural Comparison of DFT Relaxed Structures to X-Ray Crystallography Data

Compound	Bond	Calculated Bond Length (Å)[a]	Experimental Bond Length (Å)[b]
[2]*trans*-$MgCl_2(THF)_4$	Mg-Cl	2.456	2.445
	Mg-THF	2.124	2.104
[3]$[MgCl(THF)_5]^+$	Mg-Cl	2.400	2.396
	Mg-THF	2.098	2.134
[4]$[Mg(THF)_6]^{2+}$	Mg-THF	2.070	2.103
[5]$[(\mu\text{-}Cl)_3Mg_2(THF)_6]^+$	Mg···Mg	3.105	3.145
	Mg-Cl	2.514	2.504
	Mg-THF	2.059	2.086

[a] Calculated bond lengths were taken as an average within the same type of bond. [b] Experimental bond lengths are taken as an average within the same type of bond. [1]CCDC #: 96363. [2]CCDC #: 1144637. [3]CCDC #: 1192834. [4]CCDC #: 1433360. [5]CCDC #: 963637.

Complete Reaction of Mg-Cl/Al-Cl in THF. Since the Mg-Cl species are in complex equilibrium with the various Lewis acid species and Mg-Cl monomers, alternative pathways were considered to give a comprehensive perspective of the overall equilibrium of the Mg-Cl/Al-Cl in THF system and the viability of formation of the $[(\mu\text{-}Cl)_3Mg_2(THF)_6]^+$ dimer. By using the most favorable of each calculated species, a complete reaction scheme can be developed that represents the overall thermodynamic equilibria for the formation of the $[(\mu\text{-}Cl)_3Mg_2(THF)_6]^+$ dimer, as seen in Scheme 2-15. In the first step, mono-Cl abstraction must occur to form a Mg monochloride species, calculated as an uphill reaction of 4.41 kcal/mol. Any quantity of $[MgCl(THF)_5]^+$ can then go on to react with the abundant Mg dichloride species to form the dimer at a significantly favorable step of -6.30 kcal/mol, subsequently, allowing further equilibrium to be established with respect to the formation of the Mg monochloride species through mono-Cl abstraction due to Le Chatelier's principle. The entire process via the *trans*-$AlCl_3(THF)_2$ species is an overall -1.89 kcal/mol.

Another favorable route to obtain the $[(\mu\text{-Cl})_3Mg_2(THF)_6]^+$ dimer is through mono-Cl abstraction via the $[\textit{trans}\text{-}AlCl_2(THF)_4]^+$ Lewis acid. Similarly, Scheme 2-16 reveals the overall process of dimerization to be -3.16 kcal/mol. Since it is experimentally known that this Lewis acid species is in solution at *ca*. 15% for the ionic pair relative to the neutral aluminum chloride monomer[79], it is reasonable to assume this species will have a significant contribution to the formation of the dimer, as any reacted $[\textit{trans}\text{-}AlCl_2(THF)_4]^+$ will be replaced through self-ionization of *trans*-$AlCl_3(THF)_2$ by the Le Chatelier's principle. However, the relative concentration of each Al-Cl species is different and will affect the equilibrium of dimerization differently than initially predicted. Additionally, any mono-Cl abstraction reaction will cause a buildup of $[AlCl_4]^-$ that will cause a shift of equilibrium of self-ionization slightly back towards the reactants, hence, describing the complex equilibria in the changing dynamics of dimer formation seen in Schemes 2-15 and 2-16. It is important to note that the counter-anion, $[AlCl_4]^-$, produced from the self-ionization of *trans*-$AlCl_3(THF)_2$ or mono-Cl abstraction balances the charge of the produced $[MgCl(THF_5)]^+$ species, which will maintain charge balance in solution after formation of the $[(\mu\text{-Cl})_3Mg_2(THF)_6]^+$ dimer, contrary to that previously concluded in the literature that dimer formation does not occur favorably.[54] Further investigation of the complex equilibria was complimented by calculation of relative abundances and equilibrium constants.

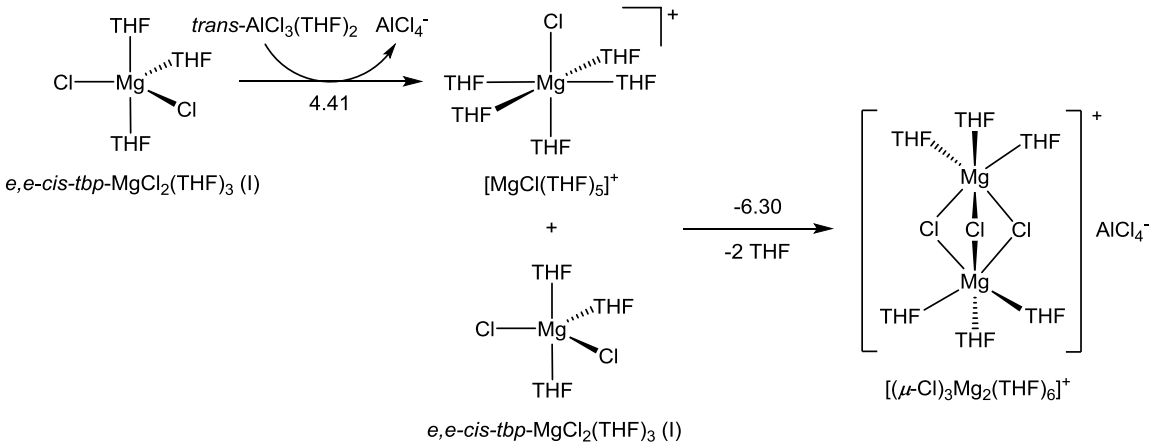

Scheme 2-15. Complete reaction for Mg-Cl dimerization with the *trans*-$AlCl_3(THF)_2$ species. Free energies in kcal/mol.

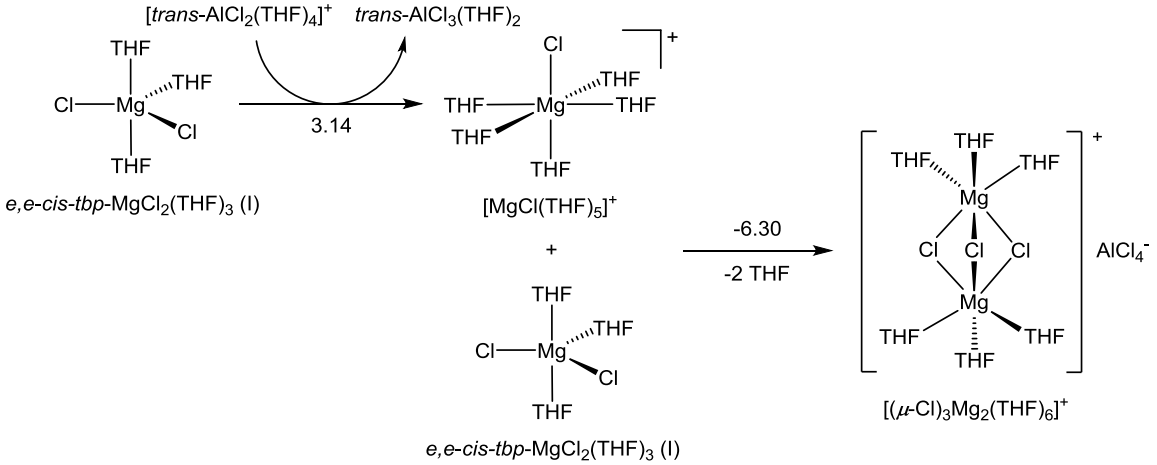

Scheme 2-16. Complete reaction for Mg-Cl dimerization with the [*trans*-$AlCl_2(THF)_4$]$^+$ species. Free energies in kcal/mol.

With a free energy of 3.14 kcal/mol for the rate-limiting mono-chloride abstraction in Scheme 2-16, the equilibrium constant was calculated as 5 x 10^{-3} using Eq 2-1,

$$K_{eq} = e^{-\Delta G/RT} \qquad (2\text{-}1)$$

where ΔG is the free energy of mono-Cl abstraction from the first step in Scheme 2-16, R is the gas constant, T is the temperature of 298.15 K, and K_{eq} is the equilibrium constant. Assuming the solubility limit of 0.06 M for $MgCl_2$ and a 1 : 1 molar ratio of $AlCl_3$,[19] the relative abundance of the Mg monochloride species in thermodynamic equilibrium was then calculated to be *ca*. 7% using Eq 2-2,

$$K_{eq} = y^2(0.06-y)^{-2} \quad (2\text{-}2)$$

where y is the amount of $[MgCl(THF)_5]^+$ formation.

Simultaneously, a free energy of 4.41 from Scheme 2-15 produces a relative abundance of the monochloride Mg species of *ca*. 2% using Eqs 2-1 and 2-2, which will also contribute to the formation of $[MgCl(THF)_5]^+$. This species can then go on to form the $[(\mu\text{-}Cl)_3Mg_2(THF)_6]^+$ dimer at -6.30 kcal/mol pushing the reaction to favorably form the dimer, hence, allowing the equilibrium to produce more Mg monochloride species through mono-Cl abstraction restoring further thermodynamic equilibrium. However, these assumptions do not account for the relative concentration of each Al-Cl species that will affect the equilibrium. From this analysis, it can be concluded that the intermediate, $[MgCl(THF)_5]^+$, will be between ca. 2% and 7%. This value can be estimated since it is known the $[trans\text{-}AlCl_2]^+$ species is only *ca.* 15% at $AlCl_3$ at *ca.* 85%. Therefore, the average free energy of mono-Cl abstraction can be calculated to be 4.22 kcal/mol, as shown in Eq 2-3:

$$85\%(4.41\ kcal/mol) + 15\%(3.14\ kcal/mol) = 4.22\ kcal/mol \quad (2\text{-}3)$$

Using Eq 2-2 gives an equilibrium constant of 8×10^{-4} relative concentration of 3% for $[MgCl(THF)_5]^+$, which is a reasonable quantity to actively go onto producing the dimer in significant quantities to play major roles in Mg battery cycling.

As both Lewis acid species are present in THF solution, *trans*-$AlCl_3(THF)_2$ and [*trans*-$AlCl_2(THF)_4]^+$, they will both contribute to the overall formation of the Mg dimer species. The overall contributed free energy of dimerization can be approximated as -2.08 kcal/mol by subtracting the calculated average free energy of mono-Cl abstraction of 4.22 kcal/mol from the free energy of dimer formation (-6.30 kcal/mol). This represents a description of the overall most favorable species found in THF solution for the Al-Cl and Mg-Cl mixture. Therefore, the approximate relative abundance of the dimer species in equilibrium can be calculated from Eqs 2-1 and 2-4,

$$K_{complete} = y^2(0.06\text{-}y)^{-1}(0.06\text{-}2y)^{-2} \quad (2\text{-}4)$$

where $K_{complete}$ is the equilibrium constant for the overall equilibrium in Schemes 2-14 and 2-15, and y is the relative amount of dimer formation while assuming a 1 : 1 molar ratio of $MgCl_2$ and $AlCl_3$ at the solubility limit.[19, 76, 79] With a free energy of -2.08 kcal/mol, $K_{complete}$ is calculated to be 3.4×10^1 using Eq 2-1 giving a relative abundance of the dimer of *ca*. 53% relative to Mg-Cl concentration. Therefore, given enough reaction time, all viable pathways indicate dimerization is favorable. During normal battery operation and electrolyte plating/stripping, these assumptions do not account for kinetic effects establishing these complex thermodynamic equilibria, hence, one may experience variable electrolyte performance based on age of electrolyte, charge/discharge rates, and relative Lewis acid concentration.

Relative LUMO Energies of Potential Electroactive Species for Platting in Mg-Cl Electrolytes. With the described equilibria above, there may be various active electrolyte species with different Mg platting/stripping species in battery cycling. Evaluation of the different electrolyte species in equilibrium will give a basis for which

species are most easily reduced. While it has been established herein the most thermodynamically abundant species is the $[(\mu\text{-Cl})_3Mg_2(THF)_6]^+$ dimer, depending on kinetics of the equilibria, different species may be available for reduction and platting during charging operation.

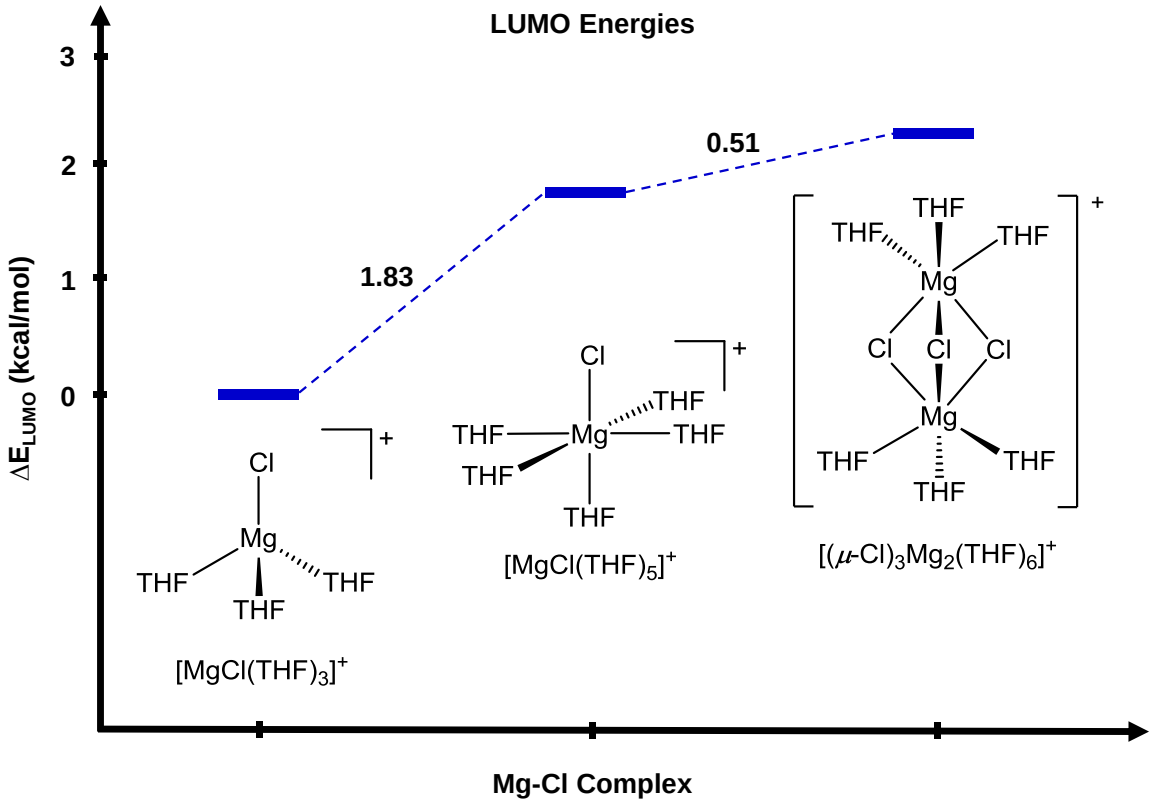

Figure 2-1. Relative LUMO energies of select Mg-Cl complexes. Changes in LUMO energies given in kcal/mol.

By comparing LUMO energies, Figure 2-1 indicates both $[MgCl(THF)_5]^+$ and $[(\mu\text{-Cl})_3Mg_2(THF)_6]^+$ dimer are likely active species for Mg deposition and stripping with the dimer requiring 0.51 kcal/mol (5.3 mV) more potential energy than the monomer. While the $[MgCl(THF)_3]^+$ species is theorized to have low abundance in solution due to

further solvation, it was added as a relative reference being more easily reduced than the prior monomer by 1.83 kcal/mol (79 mV), as it is a potential electroactive species due to the presence of an anodic potential causing dimer cleavage.

Platting/Stripping, Insertion/Extraction, and Equilibrium Considerations. The previous discussion gave a comprehensive analysis of the solvation chemistry of Mg-Cl / Al-Cl interactions in THF, but the Mg battery cycling mechanism has yet to be evaluated. Several cycles have been proposed with minimal detail or segments of the cycle in the literature[16-17, 51, 54, 56, 84]. Furthermore, the cycles and segments proposed using *ab initio* molecular dynamics (MD) were based on optimized structures of Mg-Cl in the gas phase with lower levels of DFT theory and continuum type-3 solvation models such as EIF-PCM[85] or CPCM[86-88], which have been demonstrated elsewhere to be generally less accurate than type-4 universal solvation models such as SM8[89], SM8AD[90], and SMD[68] since these newer models adjust the non-bulk-electrostatic terms independently to be consistent with a particular choice of each solvent cavity.[88] Therefore, the calculations performed in this study were utilized to assist in depicting the cycling mechanism for Mg-Cl / Al-Cl in THF electrolytes. We propose a comprehensive Mg-Cl / Al-Cl cycling mechanism in THF that accounts for previously controversial literature and findings, describing solution equilibria and reactions that occur in the bulk solution before and after stripping/platting at the anode and extraction/insertion at the cathode. Anode and Cathode interactions were described from a combination of our results and an evaluation of literature findings as discussed below. The cycling mechanism is displayed as Scheme 2-17.

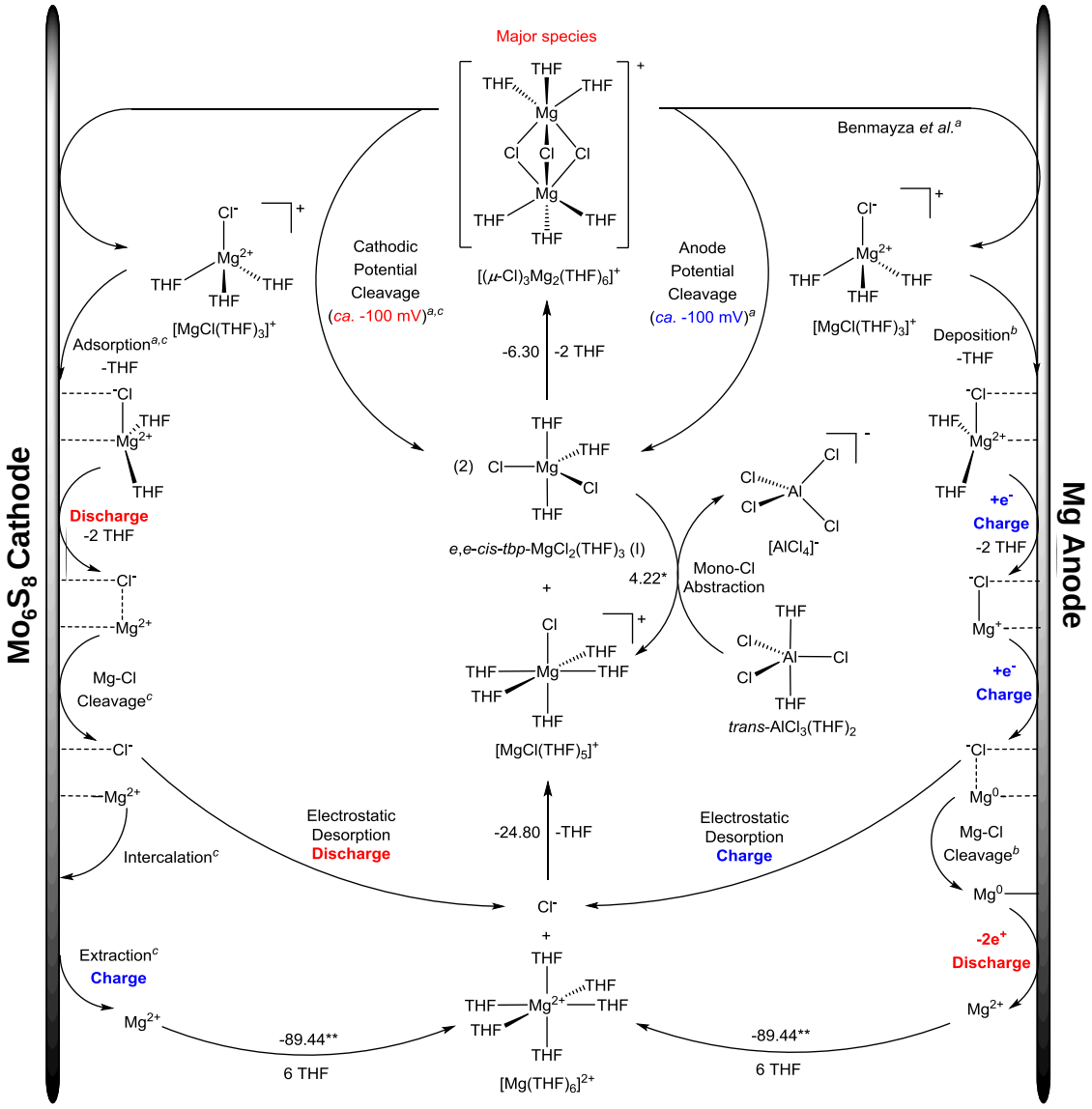

Scheme 2-17. Mg platting/stripping mechanistic cycle considering a Mo_6S_8 cathode consistently combining present results and previous reports. Free energies in kcal/mol. *Average free energy from aluminum chloride self-ionization contributions. **Solvation free energy considerations only. [a] Experimental observations of dimer formation and anodic intermediates from Benmayza *et al.*[56] [b] Theoretical work of anodic deposition by Canepa *et al.*[51] [c] Experimental and theoretical work for cathodic intercalation and extraction energies by Wan *et al.*[91]

First, aluminum chloride will self-ionize to the ion pair and undergo mono-Cl abstraction of *e,e-cis-tbp*-$MgCl_2(THF)_3$ (I) with a collective free energy of 4.22 kcal/mol to yield $[MgCl(THF)_5]^+$ at a relative abundance of 3% (charge balanced by $[AlCl_4]^-$). The Mg-Cl monomer can then go on to form the $[(\mu\text{-}Cl)_3Mg_2(THF)_6]^+$ dimer by combining with another equivalent of Mg dichloride at a favorable step of -6.30 kcal/mol, representing the overall most thermodynamically favorable and abundant species in solution. This dimer can then act as the dominant charge carrier to participate as the charge-balancing ion during the charge/discharge cycles. The dimer as the major charge carrier is in good agreement with the experimental observations of lower ionic conductivity and transference measurements found for this system by Benmayza *et al.*[56], ascribing the dimer for the low ion mobility.

During the charge cycle, electrons are removed from the cathode and moved to the anode through an external circuit. At the anode, the $[(\mu\text{-}Cl)_3Mg_2(THF)_6]^+$ dimer is attracted to electric charge buildup and subsequently involved in cleavage and reduction. Wan et al. demonstrates that inhomogeneous, highly localized charge will build up near the cation due to electrostatic attraction and cause strong repulsion of nearby THF molecules.[91] One may imagine that this electric image field is likely to cause cleavage of the dimer and/or promote partial (de)solvation.[84] Consistent with experimental studies, Benmayza *et al*. demonstrated through X-ray absorption and Hittorf experiments that polarization from the electric field in proximity to the electrode is sufficient for favorable dimer cleavage in the presence of at an electrochemical potential of *ca.* -100 mV, which is below the deposition potential for Mg.[56] Specifically, it was observed in their XANES and *K*-edge XAS studies that the dimer undergoes first-shell scattering at the anode with a potential of -100 mV and

larger potentials showing a reduction in the dimer peak with the development of several new peaks, suggesting further dimer cleavage and formation of unknown interfacial Mg intermediates, proposed as $[MgCl(THF)_5]^+$.[56] After cleavage, their combined Hittorf and ionic conductivity results indicate the cleaved monomer intermediate species undergoes a two-electron reduction leaving the Mg dichloride species in solution, confirming the dimer is not the electroactive species but reformed in the bulk solution as the charge carrier.[56] These results are in good agreement with the calculated LUMO energies, as seen in Figure 2-1, which suggests $[MgCl(THF_3)]^+$ is the most easily-reduced electrolyte species followed by $[MgCl(THF)_5]^+$ at a difference of 1.83 kcal/mol and the dimer close behind differing by 0.53 kcal/mol. However, the true active species involved in adsorption and charge transfer is still unknown and may involve more than one species, as the overpotential required to reduce each of three species shown in Figure 2-1 is within 101 mV. Based on equilibria defined in this study, both the $[MgCl(THF)_5]^+$ monomer and $[(\mu\text{-}Cl)_3Mg_2(THF)_6]^+$ dimer species are likely to be available at the time of anode adsorption depending on the time allowed for further solvation before adsorption. Additionally, monomer products from potential dimer cleavage may inhibit further solvation of $[MgCl(THF)_3]^+$ since the electron-rich anode will repel THF molecules forming the Helmholtz double-layer, as indicated by Wan *et al*.[91] It is important to note that one must use caution when predicting the active species in charge transfer since the effects of applied electrochemical potential on solvation could change the most abundant solvated species at the electrode.[51, 56, 84, 91] Figure 2-1 demonstrates these conformational changes can have significant energy differences in reduction potentials.

While Cenapa *et al.* cites Benmayza *et al.* saying the dimer does not approach the electrode surface[54], it is clear from *K*-edge XANES experiments that the dimer is altered in proximity to the anode to form an unknown active Mg monomer species[56, 92]. As represented in Scheme 2-17, the active Mg monomer intermediate, a monomer between $[MgCl(THF)_3]^+$ and $[MgCl(THF)_5]^+$, is subsequently adsorbed to the surface of the anode to undergo monochloride abstraction and reduction. The details of adsorption were calculated using *ab initio* MD by Canepa *et al.* wherein both the Cl and Mg atoms adsorb favorably to the anode followed by the favorable release of THF until the most favorable species is reached with two coordinated THF, which was proposed as the active species involved in charge transfer.[51] It is important to note that the adsorption study did not explicitly account for applied electrochemical potentials, which will likely change the active charge-transfer species.[51, 56, 92] However, it does shed some light on reaction events that occur before charge transfer.[51] Reduction of the anode-tethered Mg^{2+}-Cl species is proposed to lose the two coordinated THF as the Mg atom becomes more negative and a weaker Lewis acid.[51] The Mg^+-Cl is then reduced further which will cause cleavage of the Mg-Cl bond allowing the Cl^- anion to be released back into solution to balance the charge at the cathode. While various studies have shown chloride can bind at the anode causing slight passivation, it should only be viewed as a minor mode of decay since the theoretical studies done did not account for the buildup of electrons on the anode which will cause significant electrostatic repulsion and exergonic release and solvation of most of chloride anions. [23-24, 51, 93-94]

In accordance the study done by Wan et al.[91], charging at the Mo_6S_8 cathode moves electrons to the anode causing the favorable extraction of the intercalated Mg^{2+}, which can

then favorably solvate to the $[Mg(THF)_6]^{2+}$ species with a free energy of -89.44 kcal/mol (excludes stripping energy), as shown in Scheme 2-18. The favorability of stripping energy was not of concern since it is obvious stripping takes place in order for battery cycling to be observed experimentally with cyclic voltammetry.[16, 19] To confirm the six-coordinate species is truly the most thermodynamically favorable solvated Mg^{2+} species, a comparison to the square planar five-coordinate species was done revealing further solvation of the $[sp\text{-}Mg(THF)_5]^{2+}$ species with a free energy of -8.53 kcal/mol, confirming our predictions (Scheme 2-18). Simultaneously upon charging, the stripped chloride anion goes on to react with this solvated $[Mg(THF)_6]^{2+}$ cation from the to form the $[MgCl(THF)_5]^{+}$ species with a free energy of -24.80 kcal/mol (Scheme 2-19). The Mg monochloride species can then go on to (re)form the dimer, completing the charge cycle.

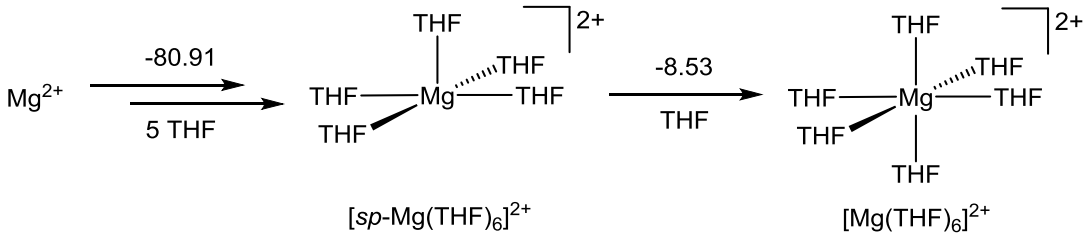

Scheme 2-18. Solvation of the Mg^{2+} ion in THF. Free energies in kcal/mol.

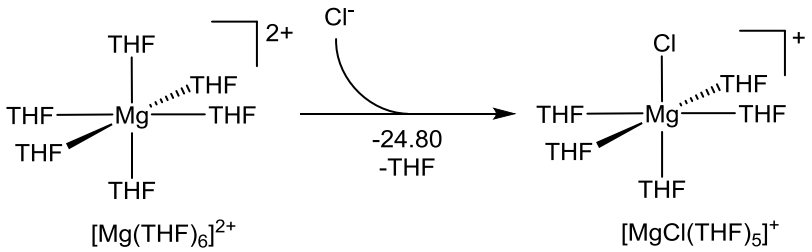

Scheme 2-19. Reaction of stripped chloride anion from the anode with extracted solvated Mg^{2+} cation from the cathode. Free energies in kcal/mol.

During discharge of the Mg battery, electrons are moved from the anode to the cathode causing the cathode to become electron rich and the anode electron poor. At the cathode, the $[(\mu\text{-Cl})_3Mg_2(THF)_6]^+$ dimer is likely to cleave in a similar manner, as discussed above, in proximity to the electrode with application of a cathodic potential to form the *e,e-cis-tbp*-$MgCl_2(THF)_3$ (I) and $[MgCl(THF)_3]^+$ species.[84, 91] The $[MgCl(THF)_3]^+$ species will continue to (de)solvate as it approaches the surface of the cathode and adsorbed in a similar manner to the anode, detailed in a the theoretical study done by Wan *et al*.[51, 91] The highly localized charge at the cathode will cause strong repulsion of the THF and the Mo_6S_8 will catalyze the fully (de)solvated adsorbed $[MgCl]^+$ species to undergo Mg-Cl scission and Mg^{2+} intercalation.[91] The chloride will then be released to react with the solvated Mg^{2+} cation from the anode side with a free energy of -24.80 kcal/mol (Scheme 2-19). The (re)solvated Mg monochloride species can then react with the neutral Mg dichloride species to form the $[(\mu\text{-Cl})_3Mg_2(THF)_6]^+$ dimer at -6.30 kcal/mol, completing the cycle once again. These results are in excellent agreement with the ionic conductivity, XAS, XANES, and Hittorf experiments done by Benmayza *et al.* and others.[23-24, 29, 51, 56, 79, 84, 92-93]

Discussion

The solvation of $AlCl_3$ in THF has been an intriguing topic for various using single crystal X-ray diffraction and NMR studies.[21-25] The above DFT calculations on the equilibrium of *trans*-$AlCl_3(THF)_2$, $[AlCl_4]^-$, and [*trans*-$AlCl_2(THF)_4]^+$ has remarkable agreement with Lefebvre's NMR results.[79] These correlations give strong evidence that the

DFT methods and parameters in this study is a good benchmark for modeling such solvated systems.

According to above DFT results, solvated $MgCl_2$ primarily exists as *trans*-$MgCl_2(THF)_3$ and can undergo mono-Cl abstraction reaction with a Lewis acid to yield the $[MgCl(THF)_3]^+$ species, which is subsequently stabilized to $[MgCl(THF)_5]^+$ through further solvation. In our previous study[16], identification of $[MgCl(THF)_3]^+$ by SPIN-MS confirms the mono-Cl abstraction reaction taking place between *trans*-$MgCl_2(THF)_3$ and a Lewis acid, which confirms the DFT ionic calculation giving an average free energy of 4.22 kcal/mol. As $[MgCl(THF)_5]^+$ is 10.7 kcal/mol more stable than $[MgCl(THF)_3]^+$, the later species detected by SPIN-MS is believed to be formed from $[MgCl(THF)_5]^+$ during ionization and gasification at the subambient pressures required for the technique.[16-17] Additionally, the DFT results indicate further removal of another THF from $[MgCl(THF)_3]^+$ is more difficult, requiring 16.74 kcal/mol to break the Mg-THF bond.

Formation of the dimer, $[(\mu\text{-}Cl)_3Mg_2(THF)_6]^+$, from *trans*-$MgCl_2(THF)_3$ and $[MgCl(THF)_5]^+$ in THF is thermodynamically favorable by -6.30 kcal/mol, representing the major species in the bulk solution. However, Figure 2-1 indicates the dimer is not the likely active species involved in charge transfer at the anode but is close enough in energy that could be involved to a certain extent. These theoretical calculations are in excellent agreement with the electrochemical measurements performed by Benmayza *et al.*[56] where it was demonstrated that formation dominates the bulk transport properties of the electrolyte while a distinct intermediate species is formed at the anode in the presence of an applied potential, which is proposed here and elsewhere to polarize and cleave the dimer

into the $[MgCl(THF)_3]^+$ monomer species.[51, 84, 91] This intermediate species can proceed in further solvation or (de)solvation and adhere to the anode for reduction and (de)solvation through electrostatic attraction. However, the true species active in charge transfer is unknown as the applied electrochemical potential is shown to significantly influence the stable species in solution as observed with the dimer cleavage at the anode.[56] After stripping, the Mg^{2+} ion can diffuse back into solution to reform the dimer through reaction with the stripped chloride anion from the cathode by a favorable -24.80 kcal/mol (Scheme 2-19), restoring the dimer species in the bulk solution. As the dimer is predicted to be the most abundant in solution as supported here, it is logical to assume the $[(\mu\text{-}Cl)_3Mg_2(THF)_6]^+$ dimer is the primary charge carrier species during battery cycling explaining the slower diffusivity and ionic conductivity observed.[56] Using a combination of previous studies discussed prior and the DFT results presented here, a comprehensive battery cycling mechanism has been proposed for the Mg-Cl / Al-Cl in THF system (Scheme 2-17).

Conclusions

DFT computational studies provided a detailed picture on coordination chemistry of Mg-Cl complexes and their ligand exchange reactivities in the $[(\mu\text{-}Cl)_3Mg_2(THF)_6]^+$ electrolyte solution. Dimerization of *e,e-cis-tbp*-$MgCl_2(THF)_3$ (I) and $[MgCl(THF)_5]^+$ to form $[(\mu\text{-}Cl)_3Mg_2(THF)_6]^+$ is calculated to be thermodynamically favorable in the bulk solution. In addition, the solvation chemistry of aluminum chloride in THF was invested to provide a comprehensive examination of of mono-Cl abstraction with *e,e-cis-tbp*-$MgCl_2(THF)_3$ (I) and $[MgCl(THF)_5]^+$. Complementary to the previous studies,

the DFT results suggest that the $[(\mu\text{-Cl})_3Mg_2(THF)_6]^+$ dimer is the dominant species primarily involved in Mg deposition as well as the primary charge carrier species in the bulk solution. To confirm the primary electroactive species, future studies should focus their attention on the effects of applied potentials on the solvated Mg-Cl species in proximity to the electrodes during the deposition process. The present DFT study provides a comprehensive, in-depth understanding of the Mg-Cl/Lewis acid dimer electrolytes and can inspire new designs of Mg electrolytes for Mg rechargeable batteries.

References

1. Gaddum, L. W.; French, H. E. *J. Am. Chem. Soc.* **1927**, *49*, 1295-1299.
2. Connor, J. H.; Reid, W. E.; Wood, G. B. *J. Electrochem. Soc.* **1957**, *104*, 38-41.
3. Brenner, A. *J. Electrochem. Soc.* **1971**, *118*, 99-100.
4. Gregory, T. D.; Hoffman, R. J.; Winterton, R. C. *J. Electrochem. Soc.* **1990**, *137*, 775-780.
5. Aurbach, D.; Suresh, G. S.; Levi, E.; Mitelman, A.; Mizrahi, O.; Chusid, O.; Brunelli, M. *Adv. Mater.* **2007**, *19*, 4260-4267.
6. Kim, H. S.; Arthur, T. S.; Allred, G. D.; Zajicek, J.; Newman, J. G.; Rodnyansky, A. E.; Oliver, A. G.; Boggess, W. C.; Muldoon, J. *Nat. Commun.* **2011**, *2*, 2-6.
7. Guo, Y.; Zhang, F.; Yang, J.; Wang, F.; NuLi, Y.; Hirano, S. *Energy Environ. Sci.* **2012**, *5*, 9100-9106.
8. Lu, Z.; Schechter, A.; Moshkovich, M.; Aurbach, D. *J. Electroanal. Chem.* **1999**, *466*, 203-217.

9. Mizrahi, O.; Amir, N.; Pollak, E.; Chusid, O.; Marks, V.; Gottlieb, H.; Larush, L.; Zinigrad, E.; Aurbach, D. *J. Electrochem. Soc.* **2008**, *155*, A103-A109.

10. Pour, N.; Gofer, Y.; Major, D. T.; Aurbach, D. *J. Am. Chem. Soc.* **2011**, *133*, 6270-6278.

11. Mohtadi, R.; Matsui, M.; Arthur, T. S.; Hwang, S.-J. *Angew. Chem. Int. Ed.* **2012**, *51*, 9780-9783.

12. Muldoon, J.; Bucur, C. B.; Oliver, A. G.; Zajicek, J.; Allred, G. D.; Boggess, W. C. *Energy Environ. Sci.* **2013**, *6*, 482-487.

13. Aurbach, D.; Weissman, I.; Gofer, Y.; Levi, E. *Chem. Rec.* **2003**, *3*, 61-73.

14. Muldoon, J.; Bucur, C. B.; Oliver, A. G.; Sugimoto, T.; Matsui, M.; Kim, H. S.; Allred, G. D.; Zajicek, J.; Kotani, Y. *Energy Environ. Sci.* **2012**, *5*, 5941-5950.

15. Sakamoto, S.; Imamoto, T.; Yamaguchi, K. *Org. Lett.* **2001**, *3*, 1793-1795.

16. Liu, T.; Cox, J. T.; Hu, D.; Deng, X.; Hu, J.; Hu, M. Y.; Xiao, J.; Shao, Y.; Tang, K.; Liu, J. *Chem. Commun.* **2015**, *51*, 2312-2315.

17. Liu, T.; Shao, Y.; Li, G.; Gu, M.; Hu, J.; Xu, S.; Nie, Z.; Chen, X.; Wang, C.; Liu, J. *J. Mat. Chem. A* **2014**, *2*, 3430-3438.

18. He, S.; Luo, J.; Liu, T. L. *J. Mat. Chem. A* **2017**, *5*, 12718-12722

19. Luo, J.; He, S.; Liu, T. L. *ACS Energy Lett.* **2017**, *2*, 1197-1202.

20. Bi, Y.; Luo, J.; Hu, B.; He, S.; Nielson, K.; Liu, T. L. *ECS Trans.* **2017**, *80*, 343-348.

21. Shao, Y.; Liu, T.; Li, G.; Gu, M.; Nie, Z.; Engelhard, M.; Xiao, J.; Lv, D.; Wang, C.; Zhang, J.-G.; Liu, J. *Sci. Rep.* **2013**, *3*, 3130.

22. Zhao-Karger, Z.; Zhao, X.; Fuhr, O.; Fichtner, M. *RSC Adv.* **2013**, *3*, 16330-16335.

23. Doe, R. E.; Han, R.; Hwang, J.; Gmitter, A. J.; Shterenberg, I.; Yoo, H. D.; Pour, N.; Aurbach, D. *Chem. Commun.* **2014**, *50*, 243-245.

24. Barile, C. J.; Barile, E. C.; Zavadil, K. R.; Nuzzo, R. G.; Gewirth, A. A. *J. Phys. Chem. C* **2014**, *18*, 27623–27630.

25. Carter, T. J.; Mohtadi, R.; Arthur, T. S.; Mizuno, F.; Zhang, R.; Shirai, S.; Kampf, J. W. *Angew. Chem. Int. Ed.* **2014**, *53*, 3173-3177.

26. Ha, S.-Y.; Lee, Y.-W.; Woo, S. W.; Koo, B.; Kim, J.-S.; Cho, J.; Lee, K. T.; Choi, N.-S. *ACS Appl. Mater. Interf.* **2014**, *6*, 4063-4073.

27. Lv, D.; Tang, D.; Duan, Y.; Gordin, M. L.; Dai, F.; Zhu, P.; Song, J.; Manivannan, A.; Wang, D. *J. Mat. Chem. A* **2014**, *2*, 15488-15494.

28. Nelson, E. G.; Brody, S. I.; Kampf, J. W.; Bartlett, B. M. *J. Mat. Chem. A* **2014**, *2*, 18194-18198.

29. Barile, C. J.; Nuzzo, R. G.; Gewirth, A. A. *J. Phys. Chem. C* **2015**, *119*, 13524-13534.

30. Liao, C.; Sa, N.; Key, B.; Burrell, A. K.; Cheng, L.; Curtiss, L. A.; Vaughey, J. T.; Woo, J.-J.; Hu, L.; Pan, B.; Zhang, Z. *J. Mat. Chem. A* **2015**, *3*, 6082-6087.

31. McArthur, S. G.; Geng, L.; Guo, J.; Lavallo, V. *Inorg. Chem. Front.* **2015**, *2*, 1101-1104.

32. Pan, B.; Zhang, J.; Huang, J.; Vaughey, J. T.; Zhang, L.; Han, S.-D.; Burrell, A. K.; Zhang, Z.; Liao, C. *Chem. Commun.* **2015**, *51*, 6214-6217.

33. Zhao-Karger, Z.; Zhao, X.; Wang, D.; Diemant, T.; Behm, R. J.; Fichtner, M. *Adv. Energy Mater.* **2015**, *5*, 1401155-1401163.

34. Cheng, Y. W.; Stolley, R. M.; Han, K. S.; Shao, Y. Y.; Arey, B. W.; Washton, N. M.; Mueller, K. T.; Helm, M. L.; Sprenkle, V. L.; Liu, J.; Li, G. S. *PCCP* **2015**, *17*, 13307-13314.

35. Brouillet, E. V.; Kennedy, A. R.; Koszinowski, K.; McLellan, R.; Mulvey, R. E.; Robertson, S. D. *Dalton Trans.* **2016**, *45*, 5590-5597.

36. Ha, J. H.; Adams, B.; Cho, J.-H.; Duffort, V.; Kim, J. H.; Chung, K. Y.; Cho, B. W.; Nazar, L. F.; Oh, S. H. *J. Mat. Chem. A* **2016**, *4*, 7160-7164.

37. Pan, B.; Huang, J.; He, M.; Brombosz, S. M.; Vaughey, J. T.; Zhang, L.; Burrell, A. K.; Zhang, Z.; Liao, C. *ChemSusChem* **2016**, *9*, 595-599.

38. Sa, N.; Pan, B.; Saha-Shah, A.; Hubaud, A. A.; Vaughey, J. T.; Baker, L. A.; Liao, C.; Burrell, A. K. *ACS Appl. Mater. Interf.* **2016**, *8*, 16002-16008.

39. Watkins, T.; Kumar, A.; Buttry, D. A. *J. Am. Chem. Soc.* **2016**, *138*, 641-650.

40. Herb, J. T.; Nist-Lund, C. A.; Arnold, C. B. *J. Mat. Chem. A* **2017**, *5*, 7801-7805.

41. Kang, S.-J.; Lim, S.-C.; Kim, H.; Heo, J. W.; Hwang, S.; Jang, M.; Yang, D.; Hong, S.-T.; Lee, H. *Chem. Mater.* **2017**, *29*, 3174-3180.

42. Mandai, T.; Akita, Y.; Yagi, S.; Egashira, M.; Munakata, H.; Kanamura, K. *J. Mat. Chem. A* **2017**, *5*, 3152-3156.

43. Li, W. F.; Cheng, S.; Wang, J.; Qiu, Y. C.; Zheng, Z. Z.; Lin, H. Z.; Nanda, S.; Ma, Q.; Xu, Y.; Ye, F. M.; Liu, M. N.; Zhou, L. S.; Zhang, Y. G. *Angew. Chem. Int. Edit.* **2016**, *55*, 6406-6410.

44. Shterenberg, I.; Salama, M.; Yoo, H. D.; Gofer, Y.; Park, J.-B.; Sun, Y.-K.; Aurbach, D. *J. Electrochem. Soc.* **2015**, *162*, A7118-A7128.

45. Tutusaus, O.; Mohtadi, R.; Arthur, T. S.; Mizuno, F.; Nelson, E. G.; Sevryugina, Y. V. *Angew. Chem. Int. Ed.* **2015**, *54*, 7900-7904.

46. McArthur, S. G.; Jay, R.; Geng, L.; Guo, J.; Lavallo, V. *Chem. Commun.* **2017**, *53*, 4453-4456.

47. Herb, J. T.; Nist-Lund, C. A.; Arnold, C. B. *ACS Energy Lett.* **2016**, *1*, 1227-1232.

48. Zhang, Z.; Cui, Z.; Qiao, L.; Guan, J.; Xu, H.; Wang, X.; Hu, P.; Du, H.; Li, S.; Zhou, X.; Dong, S.; Liu, Z.; Cui, G.; Chen, L. *Adv. Energy Mater.* **2017**, n/a-n/a.

49. Zhao-Karger, Z.; Gil Bardaji, M. E.; Fuhr, O.; Fichtner, M. *J. Mat. Chem. A* **2017**, *5*, 10815-10820.

50. He, S.; Nielson, K. V.; Luo, J.; Liu, T. L. *Energy Storage Mater.* **2017**, *8*, 184-188.

51. Canepa, P.; Gautam, G. S.; Malik, R.; Jayaraman, S.; Rong, Z.; Zavadil, K. R.; Persson, K. P.; Ceder, G. *Chem. Mater.* **2015**, *27*, 3317-3325.

52. Connell, J. G.; Genorio, B.; Lopes, P. P.; Strmcnik, D.; Stamenkovic, V. R.; Markovic, N. M. *Chem. Mater.* **2016**, *28*, 8268-8277.

53. Yoo, H. D.; Shterenberg, I.; Gofer, Y.; Gershinsky, G.; Pour, N.; Aurbach, D. *Energy Environ. Sci.* **2013**, *6*, 2265-2279.

54. Canepa, P.; Jayaraman, S.; Cheng, L.; Rajput, N. N.; Richards, W. D.; Gautam, G. S.; Curtiss, L. A.; Persson, K. A.; Ceder, G. *Energy Environ. Sci.* **2015**, *8*, 3718-3730.

55. Aurbach, D.; Schechter, A.; Moshkovich, M.; Cohen , Y. *J. Electrochem. Soc.* **2001**, *148*, A1004-A1014.

56. Benmayza, A.; Ramanathan, M.; Arthur, T. S.; Matsui, M.; Mizuno, F.; Guo, J.; Glans, P.-A.; Prakash, J. *J. Phys. Chem. C* **2013**, *117*, 26881-26888.

57. See, K. A.; Chapman, K. W.; Zhu, L. Y.; Wiaderek, K. M.; Borkiewicz, O. J.; Barile, C. J.; Chupas, P. J.; Gewirth, A. A. *J. Am. Chem. Soc.* **2016**, *138*, 328-337.

58. Kruse, H.; Goerigk, L.; Grimme, S. *J. Org. Chem.* **2012**, *77*, 10824-10834.

59. Goerigk, L.; Grimme, S. *PCCP* **2011**, *13*, 6670-6688.

60. Zhao, Y.; Truhlar, D. G. *Acc. Chem. Res.* **2008**, *41*, 157-167.

61. Wan, L. F.; Prendergast, D. *J. Am. Chem. Soc.* **2014**, *136*, 14456-14464.

62. Frisch, M. J. **2009**.

63. Krishnan, R.; Binkley, J. S.; Seeger, R.; Pople, J. A. *J. Chem. Phys.* **1980**, *72*, 650-654.

64. Mclean, A. D.; Chandler, G. S. *J. Chem. Phys.* **1980**, *72*, 5639-5648.

65. Mardirossian, N.; Head-Gordon, M. *J. Chem. Theory Comput.* **2016**, *12*, 4303-4325.

66. Zhao, Y.; Truhlar, D. G. *Theor. Chem. Acc.* **2008**, *120*, 215-241.

67. Zhao, Y.; Truhlar, D. G. *Chem. Phys. Lett.* **2011**, *502*, 1-13.

68. Marenich, A. V.; Cramer, C. J.; Truhlar, D. G. *J. Phys. Chem. B* **2009**, *113*, 6378-6396.

69. Ho, J.; Ertem, M. Z. *J. Phys. Chem. B* **2016**, *120*, 1319-1329.

70. Guerard, J. J.; Arey, J. S. *J. Chem. Theor. Comput.* **2013**, *9*, 5046-5058.

71. Addison, A. W. R.; Nageswara, T.; Reedijk, J.; Rijn, J. V.; Verschoor, G. C. *J. Chem. Soc. Dalton Trans.* **1984**, *0*, 1349 – 1356.

72. Tammiku-Taul, J.; Burk, P.; Tuulmets, A. *J. Chem. Phys. A* **2003**, *108*, 133-139.

73. Cotton, F. A.; Wilkinson, G.; Murillo, C. A.; Bochmann, M. *Advanced Inorganic Chemistry, 6th ed.* **1990**, John Wiley & Sons, Inc.: New York, **1999**.

74. Cowley, A. H.; Cushner, M. C.; Davis, R. E.; Riley, P. E. *Inorg. Chem.* **1981**, *20*, 1179-1181.

75. Derouault, J.; Forel, M. T. *Inorg. Chem.* **1977**, *16*, 3207-3213.

76. Derouault, J.; Granger, P.; Forel, M. T. *Inorg. Chem.* **1977**, *16*, 3214-3218.

77. Han, O. C.; Oldfield, E. *Inorg. Chem.* **1990**, *29*, 3666-3669.

78. Means, N. C.; Means, C. M.; Bott, S. G.; Atwood, J. L. *Inorg. Chem.* **1987**, *26*, 1466-1468.

79. Lefebvre, M. C.; Conway, B. E. *J. Electroanal. Chem.* **1998**, *448*, 217-227.

80. Aarset, K.; Shen, Q.; Thomassen, H.; Richardson, A. D.; Hedberg, K. *J. Phys. Chem A* **1999**, *103*, 1644-1652.

81. Ketelaar, J. A. A. *Recl. Trav. Chim. Pays-Bas* **1947**, *66*, 501-512.

82. Bigelow, M. J. *J. Chem. Educ.* **1969**, *46*, 495.

83. Murthy, J. K.; Gross, U.; Rüdiger, S.; Rao, V. V.; Kumar, V. V.; Wander, A.; Bailey, C. L.; Harrison, N. M.; Kemnitz, E. *J. Phys. Chem B* **2006**, *110*, 8314-8319.

84. Yoo, H. D.; Liang, Y.; Dong, H.; Lin, J.; Wang, H.; Liu, Y.; Ma, L.; Wu, T.; Li, Y.; Ru, Q.; Jing, Y.; An, Q.; Zhou, W.; Guo, J.; Lu, J.; Pantelides, S. T.; Qian, X.; Yao, Y. *Nat. Commun.* **2017**, *8*, 339.

85. Cances, M. T.; Mennucci, B.; Tomasi, J. *J. Chem. Phys.* **1997**, *107*, 3032-3041.

86. Barone, V.; Cossi, M. *J. Phys. Chem. A* **1998**, *102*, 1995-2001.

87. Cossi, M.; Rega, N.; Scalmani, G.; Barone, V. *J. Comput. Chem.* **2003**, *24*, 669-681.

88. Ho, J.; Coote, M. L.; Cramer, C. J.; Truhlar, D. G. *O. Hammerich, B. Speiser (Eds.), Organic Electrochemistry (5th edition), Taylor and Francis Group* **2015**, 229-259.

89. Marenich, A. V.; Olson, R. M.; Kelly, C. P.; Cramer, C. J.; Truhlar, D. G. *J. Chem. Theor. Comput.* **2007**, *3*, 2011-2033.

90. Marenich, A. V.; Cramer, C. J.; Truhlar, D. G. *J. Chem. Theor. Comput.* **2009**, *5*, 2447-2464.

91. Wan, L. F.; Perdue, B. R.; Apblett, C. A.; Prendergast, D. *Chem. Mater.* **2015**, *27*, 5932-5940.

92. Arthur, T. S.; Glans, P.-A.; Matsui, M.; Zhang, R.; Ma, B.; Guo, J. *Electrochem. Commun.* **2012**, *24*, 43-46.

93. Cheng, S.-T.; Todorova, M.; Freysoldt, C.; Neugebauer, J. *Phys. Rev. Lett.* **2014**, *113*, 136102-136107.

94. Nist-Lund, C. A.; Herb, J. T.; Arnold, C. B. *J. Power Sources* **2017**, *362*, 308-314.

CHAPTER III

COMPUTATIONAL STUDIES ON VIOLOGEN DERIVATIVES AS BATTERY MATERIALS IN REDOX FLOW BATTERIES[1,2]

Abstract

Redox flow batteries using synthetically tunable and resource abundant organic molecules have gained increasing attention for large-scale energy storage. Herein our studies demonstrate that rational molecular engineering yielded a series of two-electron storage viologen molecules as anolyte materials for AORFBs. Density functional theory (DFT) modeling of the electrostatic charge surface of **$(SPr)_2V$** and its charged state, **$[(SPr)_2V]^{-1}$**, suggests charge repulsion and size exclusion enable their compatibility with a cation exchange membrane. DFT calculations revealed that the one-electron and two-electron reduced redox states of these molecules were stabilized by the high charge delocalization of their frontier SOMO or HOMO. Theoretical modeling of relative reduction potentials has been employed to examine electron donating and withdrawing effects of various viologen substituents using MV as a relative reference to obtain values vs NHE. The theoretical reduction potentials exhibited mean unsigned errors of 37 and 36 mV, respectively, for the first and second reductions compared to experimentally synthesized derivatives, which represents the lowest error for such calculations to date.

---

[1] Coauthored by Camden DeBruler, Bo Hu, Jared Moss, Xuan Liu, Jian Luo, Yujie Sun, and Tianbiao Leo Liu. Reproduced with permission from *Chem*, **2017**, *3*, 961-978. Copyright 2017 Elsevier Inc.

[2] Coauthored by Camden DeBruler, Bo Hu, Jared Moss, Jian Luo, and Tianbiao Leo Liu. Reproduced with permission from *ACS Energy Lett.*, **2018**, *3*, 663-668. Copyright 2018 American Chemical Society.

Potential energy loss from disproportionation and hydrogen evolution reactions have also been modeled for these designed viologen derivatives. The present findings expand the battery design of viologen AORFBs that represent attractive RFB technology for sustainable and benign renewable energy storage.

Introduction

In order to achieve high performance AORFBs, limited but ingenious synthetic work has been done to tune the redox potential, solubility, and stability of alloxazine,[1] TEMPO,[2] and ferrocene[3] molecules. However, only very few organic molecular electrolytes are capable of storing two electrons in AORFBs.[1, 4-5] To advance the art of molecular engineering in RFB materials, herein we report a class of rationally and computationally designed highly reductive and high-charge-capacity redox-active viologen molecules as two-electron storage anolyte materials. These two-electron storage viologen molecules provide charge capacities up to 96.5 Ah/L in H_2O (or 75.0 Ah/L in 2.0 M NaCl) and redox potentials down to -0.78 V vs NHE, among the highest values of the reduction potentials and charge capacity that have been experimentally determined in aqueous electrolytes. AORFB applications with two-electron storage viologen anolytes in neutral and non-corrosive NaCl delivered a cell voltage up to 1.38 V, an impressive power density of up to 130 mW/cm^2, energy efficiency of up to 65%, and capacity retention of 99.99% per cycle at 60 mA/cm^2. The RFB design and schematic is shown in Figure 3-1.

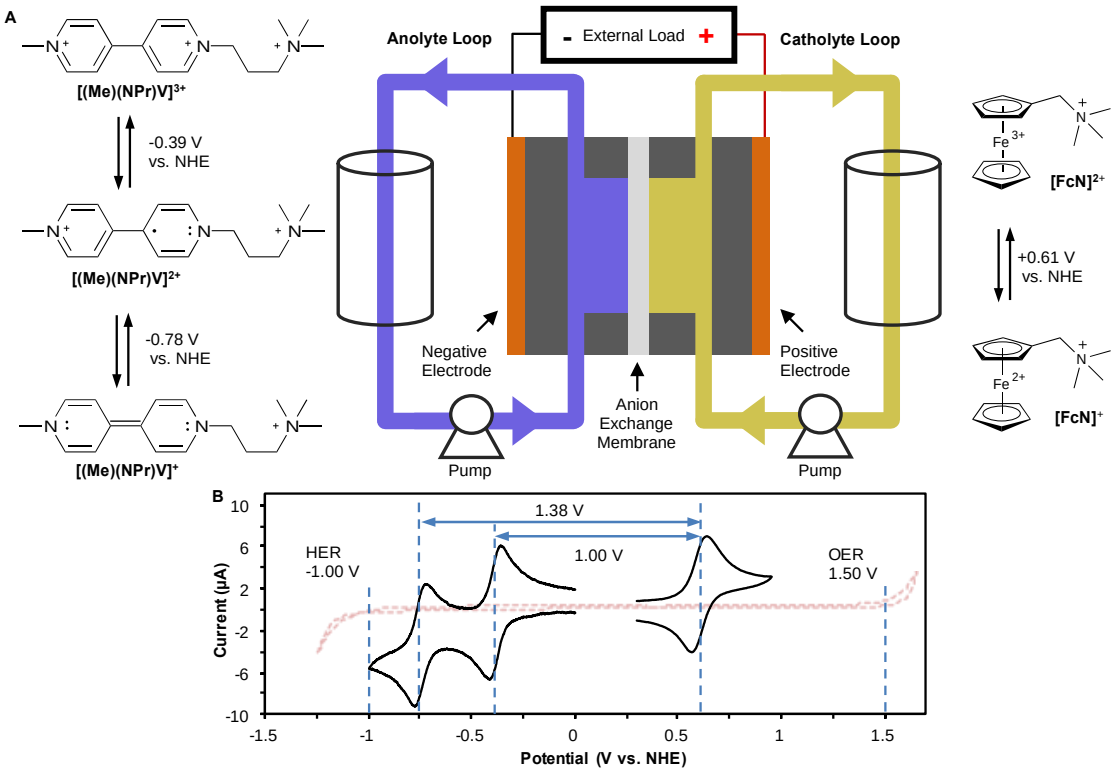

Figure 3-1. Design of **[(Me)(NPr)V]Cl$_3$**/FcNCl AORFB with electrochemical data of **[(Me)(NPr)V]Cl$_3$** anolyte and FcNCl catholyte. (A) Schematic of the **[(Me)(NPr)V]Cl$_3$**/FcNCl AORFB with structural drawings showing the cell reactions of the **[(Me)(NPr)V]Cl$_3$** anolyte and the FcNCl catholyte. The color gradients in the reservoirs represent the solution color change during the charge/discharge process. (B) Cyclic voltammograms of 4 mM **[(Me)(NPr)V]Cl$_3$** (-0.39 V, -0.78 V) and 4 mM FcNCl (0.61 V) in 0.5 M NaCl aqueous electrolyte, and labels for the onset potentials for the hydrogen evolution reaction (-1.00 V) and oxygen evolution reaction (1.50 V).

With the aim of optimizing the performance of these two-electron storage anolyte materials, computational modelling was performed using density functional theory (DFT) to gain in-depth information about the chemical and electronic structures of the three redox

states of these molecules. DFT played a key role in developing new viologen derivatives that give larger operating potentials and performance. Since the cathode material is generally fixed throughout the study, calculated theoretical viologen derivatives that show more negative one- and two-electron reduction potentials will provide larger full-cell potentials. These insights, along with geometric and chemical factors, will help prioritize synthetic targets two-electron anolytes for AORFBs and NAORFBs.

Experimental

Computational Methods. All compounds were modeled as isolated molecules at 298.15 K using the Gaussian '09 package.[6] For all candidates, the ground state structure was optimized for the initial oxidation state, one-electron reduced oxidation state, and two-electron reduced oxidation state. Basis sets consisted of 6-31+G(d)[7-8] and the electron correlation method was calculated using M06-2x[9-11]: Minnesota '06 2x global hybrid functional with 54% Hartree-Fock exchange. All geometries were optimized in water or acetonitrile as the implicit solvent. To model the implicit solvent the universal solvation model, SMD, was used, which is based on the quantum mechanical charge density of a solute molecule interacting with a continuum description of the solvent.[12] Energy minimum of each optimized structure was confirmed by checking for negative vibrational frequencies which would indicate a transition state instead of a true local or global minimum.

Calculation of Theoretical Redox Potentials. Theoretical redox potentials were calculated directly versus MV using a method derived from the Born-Haber thermodynamic cycle.[13] Typically, methods for such calculations employ the

thermodynamic cycle shown in Figure 3-2 which involves optimizing the complexes in the gas phase and reoptimizing them in the solvent phase[13-19]:

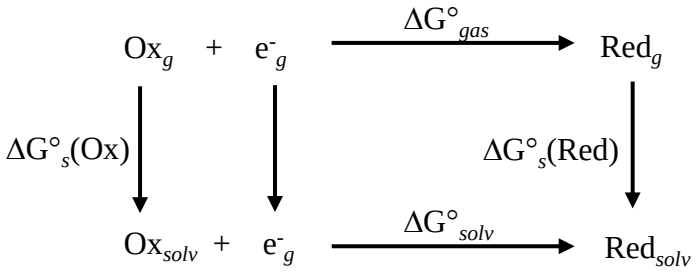

Figure 3-2. Born-Haber thermodynamic cycle for the theoretical reduction potential.[17]

Therefore, the theoretical redox potential can then be calculated by Eq 1[17]:

$$\Delta G°_{solv} = \Delta G°_{gas} + \Delta G°_{s}(Ox) - \Delta G°_{s}(Red) \quad (1)$$

However, simplification can be seen by expanding each term:

$$\Delta G°_{solv} = [G°_{g}(Red) - G°_{g}(Ox)] + [(G°_{s}(Ox) - G°_{g}(Ox)] - [G°_{s}(Red) - G°_{g}(Red)] \quad (2)$$

Cancelation of terms gives the simplified equation for the standard Gibbs free energy of a standard one-electron reduction of a compound in a given solvent,

$$\Delta G°_{solv} = G°_{s}(Ox) - G°_{s}(Red) \quad (3)$$

where $G°_{s}(Ox)$ is the unreduced compound optimized in the solvent and $G°_{s}(Red)$ is the reduced compound optimized in the same solvent.

The standard reduction potential of a half-cell can be obtained from the free energy change of reduction using the Nernst equation[20]:

$$\Delta G°_{abs} = -nFE°_{abs} \quad (4)$$

where F is the Faraday's constant, 23.06 kcal mol^{-1} V^{-1}, in the reduction, $E°$ is the standard reduction potential of a half-cell reaction, and n is the number of electrons in the half-

reaction. Using the calculated thermodynamic quantity in Eq 3 in the Nernst equation represents the *absolute* thermodynamic reduction potential of a half-reaction in a particular solvent, instead of a reduction potential relative to a reference electrode (Eq 4).

Experimentally, the conventional way of referencing an electrode potential in aqueous systems is the standard hydrogen electrode (SHE), which has been arbitrarily defined to be a potential of 0.00 V.[21] Standard conditions must be used to achieve this potential reproducibly, as shown in the schematic below:

$$Pt \mid H^{+}_{(aq)}\ (a_{H+} = 1);\ H_{2(g)}\ (p_{H2} = 1\ atm) \mid Ox(a_{Ox});\ Red(a_{Red}) \mid Pt$$

where the SHE electrode (left) is the anode where oxidation takes place, the cathode is the Ox/Red couple (right), and the vertical lines represent the phase boundaries. The cell voltage ($E_{Cathode} - E_{Anode}$) can then be calculated by the Nernst equation shown below,

$$E_{cell} = E°_{Ox/Red} - E°_{SHE} + RT/F\ (ln\ (a_{Ox}/a_{Red}) + Ej \quad (5)$$

If all the species are in their standard states and conditions then Eq 5 simplifies to:

$$E_{cell} = E°_{Ox/Red} - E°_{SHE} + E_j \quad (6)$$

where $E°_{Ox/Red}$ is the standard redox couple in Eq 4 and E_j is the liquid junction potential between the solvent/electrolyte system and the SHE. Since the physical set-up of the SHE electrode is cumbersome, more convenient secondary reference electrodes that have well-known reduction potentials vs SHE are used more often. Conversions of measured reduction potentials can then be performed to obtain standard reduction potentials vs SHE. For example, a common reference electrode is the standard calomel electrode (SCE) which has a standard reduction potential of 0.241 V relative to the SHE at 298.15 K and 1 atm.[22] Therefore, one can simply obtain a standard reduction potential vs SHE by subtracting the measured reduction potential with the SCE reference by 0.241 V. However, converting

theoretical absolute reduction potentials to SHE potentials is not as straight forward as it may initially seem. This is reflected by the fact experimental measurements are not obtained as isolated systems but in a solution matrix that has a measurable electronic potential relative to a reference electrode.[21]

For theoretical calculated absolute reduction potentials to have any experimental meaning, they must be converted to a potential relative to a reference reduction potential that can be reproduced in the laboratory. Such conditions can be difficult to obtain computationally as there are many factors involved in this process. Directly calculating this thermodynamic quantity via DFT results in several issues: (1) Proton transfer, hydrogen bonding, and other non-covalent interactions are not accounted for while modeling the compounds separately in an implicit solvent, especially when calculating the standard hydrogen electrode.[21] (2) Similar to the previous, pH of the solution, and hence, pKa of active species has a considerable effect of the reduction potential of the system in terms of the SHE.[13] (3) Liquid junction potentials need to be considered in theoretical calculations to ascertain whether or not a correction should be applied.[21] (4) Reversibility and irreversibility of a system, both thermodynamically and kinetically derived, present major problems of predicting redox potentials; more so that it may be impossible to measure the $E_{1/2}$ reduction/oxidation potential using cyclic voltammetry, in which case the theoretical quantity may be of more value but with limited practicality.[21] (5) The computational method used in the calculation should be appropriate for the application, otherwise predicted values can be far from the experimental. Theoretical reduction potentials require the calculation of the thermodynamic Gibbs free energy (as seen in Eq 2), and the accuracy of which is directly related to the accuracy of the resulting calculated reduction potential.

Some lower level functionals, including B3LYP, are not well-suited to achieve accurate free energy quantities but are suitable for comparing relative geometry optimizations, whereas M06 functionals perform much better at thermodynamic calculations.[9-11, 23-24] (6) Related to the previous, modeling the solvent is also of importance. The solvent can be modeled implicitly with relatively low computational cost compared to modeling each discrete solvent molecule explicitly in the system. Implicit solvent modeling is done by applying a polarized dielectric field across the reaction field of the solute. In continuum solvent models, such as EIF-PCM[25] and CPCM[26-27], the electrostatic term outside of the solvent cavity (bulk electrostatic term) is treated independently from the electrostatic term within the cavity boundary (non-bulk electrostatic term).[28] These are called type-3 solvent models and are generally less accurate than type-4 models, such as the universal solvation models, SM8[29], SM8AD[30], and SMD[12]. These newer type-4 models treat the non-bulk-electrostatic term as an intrinsic value unique to each cavity generated by use of an analytic surface area algorithm that accounts for solute geometry instead of relying on user input, hence, giving much more accurate solvent optimizations. This adjustment is necessary because the bulk electrostatic contribution is very sensitive to the cavity boundary. Hence, it is essentially required to use type-4 or related solvation models to accurately predict reduction potentials from thermodynamic calculations.[21] (7) Ionic pairs, such as the supporting electrolyte or the solute itself, may give rise to significant contributions to the electron reduction potential of a system that may be hard to predict due to the absence of the ion pair interactions in theoretical calculations.[31] (8) The Born-Haber thermodynamic cycle for a reduction (Figure 3-2) neglects a major part of the entropy of solvation, that is, the partial loss of translation

and rotation entropies due to constrictions from continual contact with neighboring solvent molecules.[32] However, including solvation effects into the calculations was shown to not improve theoretical reduction predictions.[15] (9) Calculating the theoretical SHE electrode, along with other similar electrochemical processes, do not account for the electron-transfer interaction at the electrode surface.[33] Omitting the effects given in (8) and (9) results in significant errors while calculating the absolute potential of the SHE.[34]

Attempts have been made to overcome the challenge of absolute reduction potential to be relative to the SHE, and one method is by using the thermodynamic cycle for the SHE shown in Figure 3-3. Each term within the cycle specifies either the gas phase or solvent phase calculation.

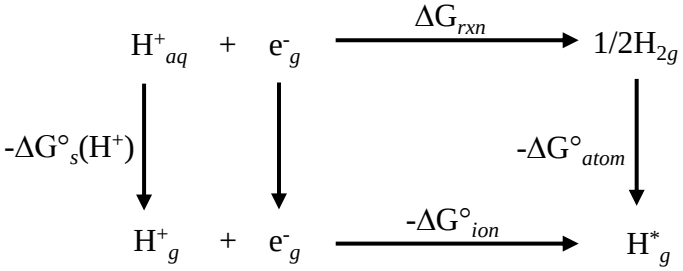

Figure 3-3. Thermodynamic cycle for the standard hydrogen electrode.

Therefore, the absolute reduction potential for the standard electrode can be calculated as[21]:

$$E_{SHE} = -\Delta G_{rxn}/F \quad (7)$$

where,

$$-\Delta G_{rxn} = \Delta G°_{ion} + \Delta G°_{atom} + \Delta G°_S(H^+) = \Delta_f G°(H^+) + \Delta G°_S(H^+) \quad (8)$$

Currently, the most common values of E_{SHE} used are 4.28 V[35] and 4.42 V[33]. However, there is still a large amount of uncertainty for this technique due to the inability to accurately predict the contribution associated with the surface potential of the solvent in the solvation of the ionic species, along with the prior considerations mentioned prior and others not discussed here.[21, 33, 36-38] Therefore, an alternative approach was used to calculate the theoretical redox potentials vs the normal hydrogen electrode (NHE) that has been known to give more accurate results than the purely theoretical methods mentioned above, that is, to calculate the *relative* reduction potentials.[21]

In this study, relative redox potentials were calculated by taking the theoretical half-cell reduction potential of a viologen derivative (abbreviated below as [V]) and subtracting the appropriate experimental (empirical) standard reduction potential (either first- or second-electron redox couple) of the internal reference, MV vs NHE.[39] In this way, increased accuracy of such calculations can be achieved due to a considerable amount of systematic error cancellation of up to 600 mV.[21] The added advantage is the calculation of $E°_{SHE}$ is no longer needed, as well as eliminating the need of optimizing molecules in the gas phase (since self-consistent reaction field (SCRF) calculations include the solvent free energy corrections) saving computational cost. The major disadvantage to this method is that the reference molecule being calculated has to be structurally similar to that of the compound of interest since this method relies on cancellation of systematic error, and an accurate standard reduction potential for a structurally similar compound may not always be available.[21] Hence, the closer the molecule is in structure to the target system the less systematic error there will be, therefore, giving more accurate calculated reduction potentials. Since this study focuses on the well-known MV compound and its theoretical

derivatives, calculating relative reduction potentials in this way should give good correlation to that of the experimental values.

The calculation of the theoretical relative redox potentials vs MV as a reference can be simplified as shown below. (a) Calculation of the first theoretical reduction potential of a viologen derivative, [V]:

Rxn 1: $[V]^{2+} + [MV]^{+} \rightarrow [V]^{+} + [MV]^{2+}$

The change in Gibbs free energy of the charge transfer, ΔG°_{CT}, for the first-electron reduction can be calculated from the respective solvent-relaxed geometries from Rxn 1:

$$\Delta G^{\circ}_{CT} = G^{\circ}_{[V]+} - G^{\circ}_{[V]2+} + G^{\circ}_{[MV]2+} - G^{\circ}_{[MV]+} = \Delta G^{\circ}_{[V]2+/+} + \Delta G^{\circ}_{[MV]+/2+} \quad (9)$$

The free energies of charge transfer can then be used in the Nernst equation representing the maximum work of electronic potential in the system:

$$\Delta G^{\circ}_{CT} = -nFE^{\circ}_{cell} \quad (10)$$

where n = 1, F = 23.061 kcal/mol·V, and E°_{cell} is the full-cell voltage ($E_{cathode} - E_{anode}$). Therefore, the theoretical first-electron reduction potential for a viologen derivative, $E^{\circ}_{calc[V]+/2+}$, can be calculated by subtracting the experimentally measured first-electron standard reduction potential of MV vs NHE, represented as $E^{\circ}_{exp[MV]+/2+}$ as shown in Eq 11:

$$\Delta G^{\circ}_{CT} = -nF(E^{\circ}_{calc[V]+/2+} - E^{\circ}_{exp[MV]+/2+}) \quad (11)$$

Rearrangement gives us the standard reduction potential for a viologen derivative in Eq 12:

$$E^{\circ}_{calc[V]+/2+} = -\Delta G^{\circ}_{CT}/nF + E^{\circ}_{exp[MV]+/2+} \quad (12)$$

where n = 1, F = 23.061 kcal/mol·V, and $E^{\circ}_{exp[MV]2+/+}$ = -0.45 V vs NHE is the measured experimental value. (b) Similarly, the second electron reduction ($E^{\circ}_{calc[V]+/0}$) of a viologen was calculated in the same fashion as the first. However, instead of using the experimental

measurement of the first-electron standard reduction potential of MV vs NHE, the second-electron potential was used, $E^{\circ}_{exp[MV]0/+}$. This is a necessary adjustment to further eliminate systematic computational error due to the electronic and structural differences of the viologens during the first- and second-electron reductions, and thereby can be effectively modelled as shown below:

Rxn 2: $[V]^{+} + [MV]^{0} \rightarrow [V]^{0} + [MV]^{+}$

$$\Delta G^{\circ}_{CT2nd} = G^{\circ}_{[V]0} - G^{\circ}_{[V]+} + G^{\circ}_{[MV]+} - G^{\circ}_{[MV]0} = \Delta G^{\circ}_{[V]+/0} + \Delta G^{\circ}_{[MV]0/+} \quad (13)$$

Applying Eq 10 to Eq 13 gives:

$$\Delta G^{\circ}_{CT2nd} = -nF(E^{\circ}_{calc[V]0/+} - E^{\circ}_{exp[MV]0/+}) \quad (14)$$

where $E^{\circ}_{exp[MV]0/+}$ = -0.76 V vs NHE. Therefore, the theoretical reduction potentials for the second electron can be calculated as:

$$E^{\circ}_{calc[V]0/+} = -\Delta G^{\circ}_{CT2nd}/nF + E^{\circ}_{exp[MV]0/+} \quad (15)$$

Relative redox potentials calculated in acetonitrile was done using the same method as above, except the experimental potentials of MV-TFSI in acetonitrile with 0.1 M $TBAPF_6$ supporting electrolyte vs $Fc^{0/+}$ were used for the first and second reductions and then converted vs NHE. The Fc redox couple of 0.641 V vs NHE was used, as obtained from the experimental value of Fc redox couple vs SCE in acetonitrile under the same conditions giving 0.40 V vs SCE.[40] The SCE is 0.241 V vs NHE, therefore, simple addition gives 0.641 V vs NHE for the Fc redox couple in acetonitrile with 0.1 M $TBAPF_6$ supporting electrolyte. Hence, the experimental reduction potentials for the first- and second-electron reductions of MV-TFSI in acetonitrile are -0.41 V and -0.86 V vs NHE, respectively.

Computation of the Disproportionation Reaction. DFT was used to predict the viability for the designed viologen derivatives to undergo disproportionation as a means to access the doubly reduced state which can go on to further react in hydrogen evolution, resulting in energy and capacity loss. The disproportionation reaction of a viologen derivative is shown in Rxn 3:

Rxn 3: $$2\,[V]^{+} \rightarrow [V]^{2+} + [V]^{0}$$

The free energy of disproportionation, $\Delta G^{\circ}_{Disp.}$, can be calculated by Eq 16:

$$\Delta G^{\circ}_{Disp.} = G^{\circ}_{[V]2+} + G^{\circ}_{[V]0} - 2(G^{\circ}_{[V]+}) \quad (16)$$

Computation of the Hydrogen Evolution Reaction. The second-electron reduced state of the viologen derivatives may have enough electronic potential to reduce protons dissolved in solution to produce dihydrogen. Hence, the hydrogen evolution reaction decreases energy efficiency of RFBs as energy storage devices. To avoid this issue, DFT was used to help eliminate viologen candidates that may show a higher tendency towards hydrogen evolution. The thermodynamics of the hydrogen evolution reaction was evaluated independently for both the first and second reductions of the viologen derivatives, as represented in Rxns 4 and 5:

Rxn 4: $$2\,[V]^{+}_{aq} + 2\,H^{+}_{aq} \rightarrow 2\,[V]^{2+}_{aq} + H_{2g}$$

Rxn 5: $$2\,[V]^{0}_{aq} + 2\,H^{+}_{aq} \rightarrow 2\,[V]^{+}_{aq} + H_{2g}$$

The calculation for the free energy of hydrogen evolution reaction is shown in Eqs 17 and 18:

$$\Delta G^{\circ}_{2V+/2H+} = 2(G^{\circ}_{[V]2+}) + G^{\circ}_{H2g} - 2(G^{\circ}_{[V]+}) + 2(G^{\circ}_{H+aq}) \quad (17)$$

$$\Delta G^{\circ}_{2V0/2H+} = 2(G^{\circ}_{[V]+}) + G^{\circ}_{H2g} - 2(G^{\circ}_{[V]0}) + 2(G^{\circ}_{H+aq}) \quad (18)$$

where $\Delta G^{\circ}_{2V+/2H+}$ is the change in free energies of the reduction of hydrogen via two singly-reduced viologens, $\Delta G^{\circ}_{2V0/2H+}$ is the change in free energies for the reduction of hydrogen via two doubly-reduced viologens, and the other terms specify the compound either in the gas-phase or solvent-phase. However, if modeled directly as shown in Eqs 17 and 18, the proton would be essentially a "free proton" in solution at infinite concentration. The resulting theoretical reaction would be highly thermodynamically favorable for hydrogen evolution at around -300 kcal/mol (calculated), which is unreasonable since this magnitude of inefficiency is not observed in these RFBs.[41-42] In reality, the proton source for hydrogen evolution reactions in AORFBs is from water, whose favorability is dependent on pH or proton concentration. However, Gaussian '09 software cannot model compounds at various pH's, as it gives electronic and thermodynamic quantities of single molecules. Therefore, since the pH is assumed to be 7, the most acidic proton will come from the autoprotolysis reaction of water, shown in Rxn 6 below:

Rxn 6: $H_2O_{aq} \rightarrow H^+_{aq} + OH^-_{aq}$ (autoprotolysis)

The autoprotolysis of water is only to a small extent, and therefore, the dissociation of water can effectually be modeled as an average percent dissociate of one water molecule, since this is in rapid exchange, as represented below in Rxn 7:

Rxn 7: $H_2O_{aq} \rightarrow H^{\delta+}\cdots OH^{\delta-}_{aq}$ (autoprotolysis)

Therefore, the change in free energies of Rxn 7 can be calculated by:

$$\Delta G^{\circ}_{Dissociation} = G^{\circ}_{H\cdots OHaq} - G^{\circ}_{H2Oaq} \quad (19)$$

Rearrangement gives the free energy for the term, $G^{\circ}_{H\cdots OHaq}$,

$$G^{\circ}_{H\cdots OHaq} = \Delta G^{\circ}_{Dissociation} + G^{\circ}_{H2Oaq} \quad (20)$$

The standard Gibbs free energy of autoprotolysis of water can be calculated since the pKa for the autoprotolysis of water is known, as shown in Eq 21:

$$\Delta G^{\circ}_{Dissociation} = 2.303RT \cdot pKa_{H2O} \quad (21)$$

where R is the gas constant in Hartrees (au), T is 298.15 K, and the pKa of water for autoprotolysis, assuming the conventional method of using the activity of water is unity, is pKa_{H2O} = 14.00.[43-44] Calculating Eq 21 with the pKa of water gives $\Delta G^{\circ}_{Dissociation}$ = -0.030442 au, which represents the degree of change in free energies during the self-ionization of water, or the extent of the water dissociation due to autoprotolysis.

One can rationally assume that the free energy of dissociation is somewhere between the completely deprotonated form of H_2O (analogous to completely acidic solutions) and the fully relaxed geometry of water (completely neutral solution with zero degree of autoprotolysis). These computational bounds were calculated by optimizing a free proton and a free hydroxide ion, separately, and adding the free energies to form the completely dissociated energy upper limit; and the theoretical free energy of fully relaxed water formed the lower energy limit, as shown in Eqs 22-24:

$$\Delta G^{\circ}_{OH^-} = -75.916012 \text{ au} \quad (22)$$

$$\Delta G^{\circ}_{H^+} = -0.225180 \text{ au} \quad (23)$$

The absolute free energy of complete dissociation is thus,

$$\Delta G^{\circ}_{Comp.Diss.} = \Delta G^{\circ}_{OH^-} + \Delta G^{\circ}_{H^+} = -76.141192 \text{ au} \quad (24)$$

The free energy of relaxed water,

$$\Delta G^{\circ}_{H2O} = -76.396262 \text{ au} \quad (25)$$

Comparing Eq's 24 and 25, it can be seen the free energy of the partially dissociated form of water, $G^{\circ}_{H\cdots OHaq}$, must be between ΔG°_{H2O} and $\Delta G^{\circ}_{Comp.Diss.}$. Adding the calculated free

energy of fully relaxed water (Eq 25) to the experimental free energy of autoprotolysis to Eq 21 yields Eq 26:

$$G^{\circ}_{H\cdots OHaq} = -76.365820\ au \quad (26)$$

This quantity is within good agreement to the predicted bounds shown in Eqs 24 and 25 in that it is much closer to Eq 24 since the autoprotolysis of water is small. To simplify further calculations of hydrogen evolution with viologen derivatives, a correction was added to H^{+}_{aq} to represent the *effective proton concentration* at pH = 7 by subtracting the absolute free energy of the hydroxide ion from $G^{\circ}_{H\cdots OHaq}$, as shown in Eq 27:

$$\Delta G^{\circ}_{H+corr.} = G^{\circ}_{H\cdots OHaq} - \Delta G^{\circ}_{OH-} = -0.449808\ au \quad (27)$$

The hydrogen evolution reaction with viologen derivatives shown in Rxns 4 and 5 then become:

Rxn 8: $$2\,[V]^{+}_{aq} + 2\,H^{+}_{corr.} \rightarrow 2\,[V]^{2+}_{aq} + H_{2g}$$

Rxn 9: $$2\,[V]^{0}_{aq} + 2\,H^{+}_{corr.} \rightarrow 2\,[V]^{+}_{aq} + H_{2g}$$

and Eqs 17 and 18 become:

$$\Delta G^{\circ}_{2V+/2H+} = 2(G^{\circ}_{[V]2+}) + G^{\circ}_{H2g} - 2(G^{\circ}_{[V]+}) + 2(G^{\circ}_{H+corr.}) \quad (28)$$

$$\Delta G^{\circ}_{2V0/2H+} = 2(G^{\circ}_{[V]+}) + G^{\circ}_{H2g} - 2(G^{\circ}_{[V]0}) + 2(G^{\circ}_{H+corr.}) \quad (29)$$

The hydrogen evolution reaction with viologen derivatives in non-aqueous (acetonitrile) systems was modeled using the same method described above with the exception that: (1) all compounds were optimized in acetonitrile and (2) there was no need to correct the free energy of proton dissociation of CH_3CN since the self-ionization is negligible ($pK_{HS} = 33.6$) giving only *ca.* 0.05 kcal/mol error.[45-46] Therefore, the free energy of the proton was calculated by the difference of the protonated and deprotonated acidic *beta*-proton on CH_3CN as shown in Eq 30:

$$\Delta G^{\circ}_{H+non\text{-}aq} = G^{\circ}_{CH3CN} - \Delta G^{\circ}_{CH2CN\text{-}} = -0.503000\ au \quad (30)$$

Results and Discussion

Electronic Structures and Geometries of Viologen Derivatives at Different Redox States. It is fundamentally important to understand structural evolution during the redox process for these charge storage molecules, to gain an in-depth understanding of their chemical properties. To this end, we conducted DFT calculations (using M06-2x functional, the 6-31+G(d) basis set, and the SMD solvation model) to define the chemical and electronic structures of **[(Me)(NPr)V]Cl$_3$**. Shown in Figure 3-4 are the optimized ground states (top view and side views), frontier orbitals, and assigned primary resonance structures of three redox states, **[(Me)(NPr)V]$^{3+}$**, **[(Me)(NPr)V]$^{2+}$**, and **[(Me)(NPr)V]$^{+}$**. **[(Me)(NPr)V]$^{3+}$** has two pyridinium rings that have almost identical bond distances (Figure 3-4 caption), indicating that N-(trimethylaminium)propyl and N-methyl groups have similar effects on the structure of the pyridinium ring. The C3-C8 bond between the two pyridinium rings is 1.483 Å, assigned as a C-C single bond. It is also noted that two pyridinium rings of **[(Me)(NPr)V]$^{3+}$** have a dihedral angle of 37.27° (<C4-C3-C8-C9). Both HOMO (highest occupied molecular orbital) and LUMO (lowest occupied molecular orbital) of **[(Me)(NPr)V]$^{3+}$** are symmetrically spread throughout the two pyridinium rings. The one-electron reduced species, **[(Me)(NPr)V]$^{2+}$**, exhibits a C3-C8 bond between two pyridine/pyridinium rings of 1.426 Å, ca. 0.05 Å shorter than that of **[(Me)(NPr)V]$^{3+}$**. By inspecting the SOMO (singly occupied molecular orbital) of **[(Me)(NPr)V]$^{2+}$** (Figure 3-4, middle), the shorter C3-C8 bond is attributed to the Pi-bonding interaction between C3 and

C8 atoms. In addition, it can be seen that the unpaired electron is highly delocalized within two pyridine/pyridinium rings.

Consistent with the two-ring delocalization and the Pi-bonding interaction, two pyridine/pyridinium rings are co-planar with a very small dihedral angle of 0.96°, a striking structural change from **[(Me)(NPr)V]$^{3+}$**. Two major resonance structures of **[(Me)(NPr)V]$^{2+}$** are shown in Figure 3-4 (right). Owing to the increased Pi-interaction of C3 and C8 atoms, two-electron reduced species, **[(Me)(NPr)V]$^{+}$**, has an even shorter C-C bond, 1.38 Å, between two rings, which is assigned as a C=C double bond in its resonance structure (Figure 3-4, middle). Its HOMO confirmed high charge delocalization within its two co-planar rings and an even smaller dihedral angle of 0.74°.

Importantly, according to the molecular orbital theory, the charge delocalization is essential to stabilize the energetic **[(Me)(NPr)V]$^{2+}$** and **[(Me)(NPr)V]$^{+}$** states, and echoes the observed electrochemical reversibility and stable battery performance of the **[(Me)(NPr)V]$^{3+/2+}$** and **[(Me)(NPr)V]$^{2+/+}$** redox couples. Consistently, similar chemical and electronic structure features were observed in the three redox states of **[(NPr)$_2$V]Br$_4$** (Figure 3-4).

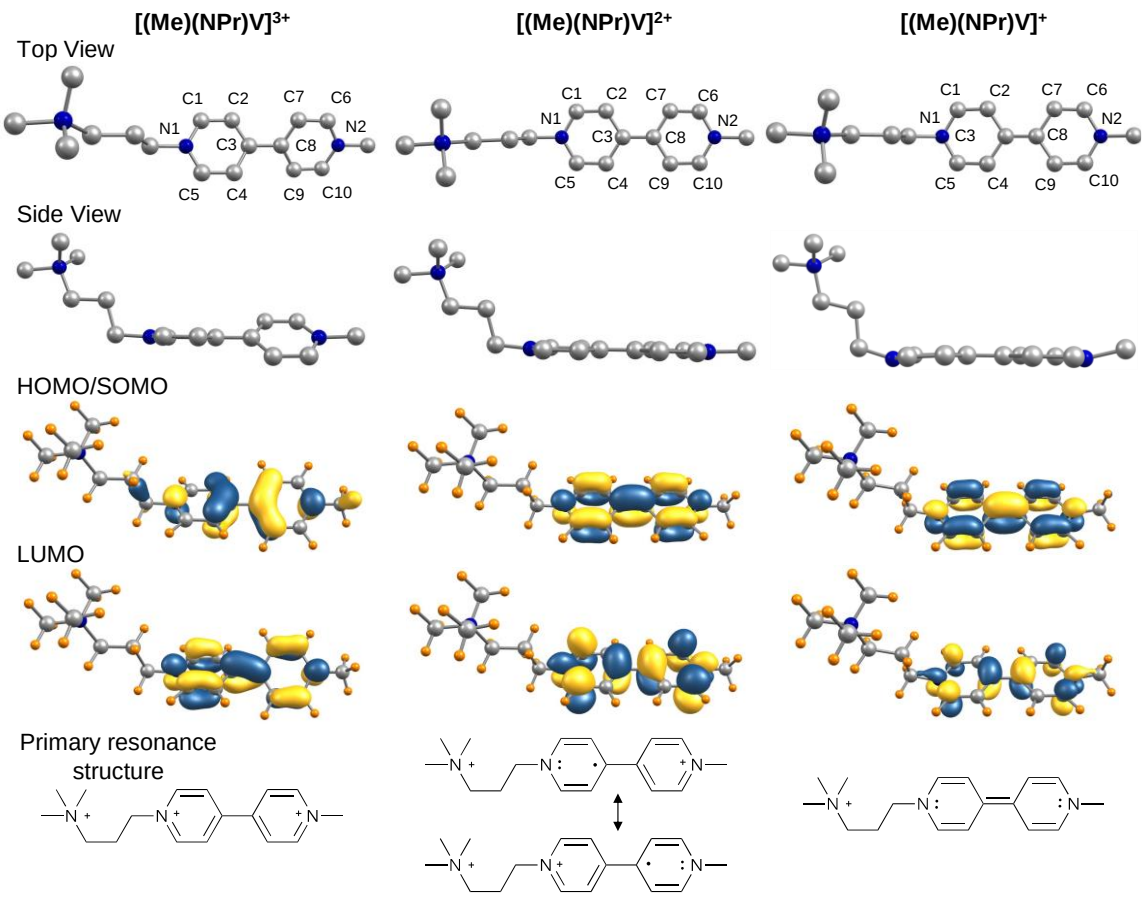

Figure 3-4. Optimized DFT structures (Top and Side Views: hydrogens were omitted for clarity), frontier HOMO/SOMO and LUMO orbitals, and assigned primary resonance structure of **[(Me)(NPr)V]$^{3+}$** (left), **[(Me)(NPr)V]$^{2+}$** (middle), and **[(Me)(NPr)V]$^{+}$** (right). Selected bonding distances (Å) for **[(Me)(NPr)V]$^{3+}$**: N1-C1, 1.347; N1-C5, 1.347; C1-C2, 1.380; C2-C3, 1.398; C3-C4, 1.398; C4-C5, 1.380; C3-C8, 1.483; N2-C6, 1.347; N2-C10, 1.346; C6-C7, 1.380; C7-C8, 1.397; C8-C9, 1.398; C9-C10, 1.381. Selected bonding distances for **[(Me)(NPr)V]$^{2+}$**: N1-C1, 1.366; N1-C5, 1.366; C1-C2, 1.365; C2-C3, 1.432; C3-C4, 1.432; C4-C5, 1.364; C3-C8, 1.426; N2-C6, 1.363; N2-C10, 1.365; C6-C7, 1.366; C7-C8, 1.430; C8-C9, 1.431; C9-C10, 1.364. Selected bonding distances for **[(Me)(NPr)V]$^{+}$**: N1-C1, 1.393; N1-C5, 1.393; C1-C2, 1.350; C2-C3, 1.465; C3-C4, 1.465;

C4-C5, 1.350; C3-C8, 1.375; N2-C6, 1.385; N2-C10, 1.385; C6-C7, 1.352; C7-C8, 1.464; C8-C9, 1.464; C9-C10, 1.352.

Computational Modeling of the Cation Exchange Membrane Compatibility of 1,1'-Bis[2-Sulfonatopropyl]-4,4'-Bipyridinium, $(SPr)_2V$. Experimental observations found that **(SPr)2V** does not crossover a Nafion cation exchange membrane while **(NPr)2V** exhibits a greater degree of crossover increasing capacity decay. To understand the exceptional compatibility of the charge-neutral $\mathbf{(SPr)_2V}$ with the Nafion cation exchange membrane whose ion channel structure is well understood,[47] DFT modeling was applied to calculate the formal charge distribution and molecular size of the neutral $\mathbf{(SPr)_2V}$ and its charged state, $\mathbf{[(SPr)_2V]^-}$. Shown in Figures 3-5A and 3-5B are the optimized structures of $\mathbf{(SPr)_2V}$ and $\mathbf{[(SPr)_2V]^-}$ encased with their electrostatic charge surface. The space-filling models of $\mathbf{(SPr)_2V}$ and $\mathbf{[(SPr)_2V]^-}$ (Figures 3-5C and 3-5D) have a 3-dimensional size ca. $0.6 \times 0.8 \times 2.2$ nm^3. For the neutral $\mathbf{(SPr)_2V}$, negative charge represented by red color is concentrated on the two terminal SO_3^- groups while the positive charge represented by blue color is delocalized throughout the bipyridine fragment. $\mathbf{[(SPr)_2V]^-}$ displays a dominant negative charge surface while the positive charge density centered on the bipyridine fragment is significantly decreased. According to the parallel water channel model of Nafion membranes, ion transport nano-channels of hydrated Nafion membranes have an averaged size around 2.4 nm (Figures 3-5C and 3-5D).[47] Regarding the probability of crossover, $\mathbf{(SPr)_2V}$ can adopt two basic orientations when approaching the nano-channels of a Nafion cation exchange membrane, namely perpendicular orientation and parallel orientation, as displayed in Figures 3-5C and 3-5D,

respectively. When **(SPr)$_2$V** adopts the perpendicular orientation, the native charge repulsion between both SO_3^- groups of **(SPr)$_2$V** and the SO_3^- groups of the cation exchange membrane applies, and also such orientation (2.2 nm) renders an unfavorable size match with the channel (2.4 nm) of the membrane to move in. When **(SPr)$_2$V** adopts the parallel orientation, the native charge repulsion between the SO_3^- group of **(SPr)$_2$V** and the SO_3^- groups of the cation exchange membrane also disfavors the crossover of **(SPr)$_2$V**. The parallel orientation (0.8 nm) can fit into the channel of the membrane and may have a higher chance than the perpendicular orientation to cross over. In addition, the irregularity of the ion channel size of the membrane can also minimize the crossover of the active species.[47] Overall, the proposed charge repulsion and size exclusion explains the observed non-crossover of **(SPr)$_2$V** during the long cycling battery testing. **[(SPr)$_2$V]$^-$** has one more net negative charge, the chance to crossover is even lower. Although the ion channel structure of the CSO is unknown, it is believed the membrane has the similar interactions with **(SPr)$_2$V**and **[(SPr)$_2$V]$^-$** to achieve the observed cycling stability.

In comparison to the anion exchange methyl viologen / ammonium functionalized ferrocene AORFBs previously reported,[3] the present cation exchange **(SPr)$_2$V** / KI delivered comparable current performance, cycling stability, even a higher energy efficiency and power density. It can be predicted that introduction of additional negative charge functionalities such a $-SO_3^-$ or $-PO_4^{2-}$ group can lead to new cation exchange viologen AORFBs. Furthermore, it is expected that the development of organic catholyte molecules with higher oxidation potential and higher solubility can further enlarge the cell voltage and energy density of the cation exchange viologen AORFBs.

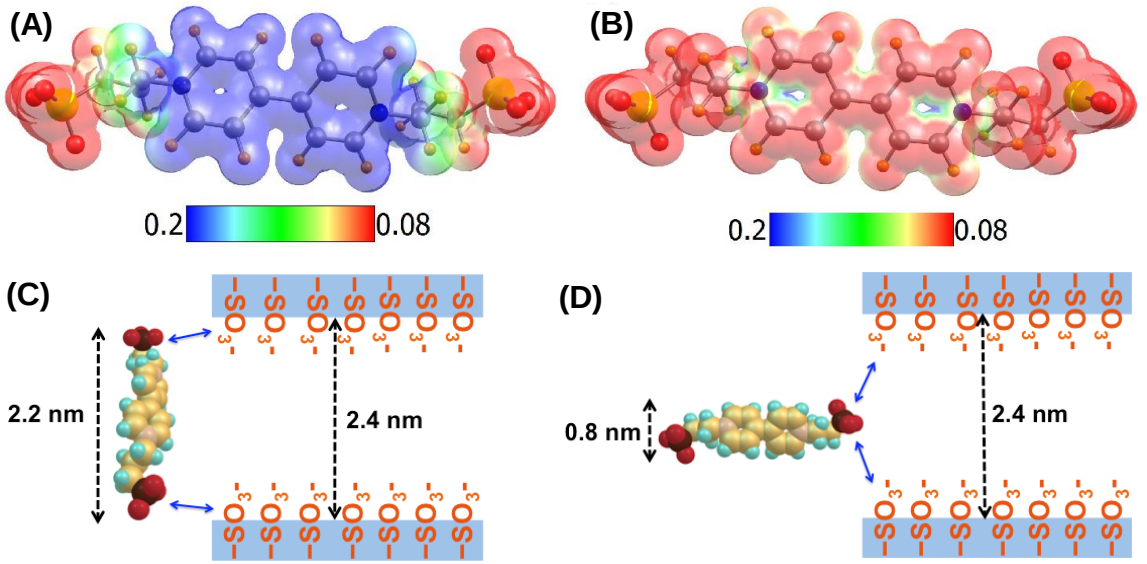

Figure 3-5. Electronic and physical characteristics of **$(SPr)_2V$**. (A) Electrostatic charge surface of the optimized ground state structure of **$(SPr)_2V$**; (B) Electrostatic charge surface of the optimized ground state structure of **$[(SPr)_2V]^-$**; (C) Proposed interaction of **$(SPr)_2V$** represented in a space-filling model adopting perpendicular orientation with the Nafion membrane; (D) Proposed interaction of **$(SPr)_2V$** represented in a space-filling model adopting parallel orientation with the Nafion membrane. The blue double-headed arrows indicate the negative charge repulsion.

Computational Prediction and Experimental Verification of New Two-Electron Storage Viologens. To expand the concept of two-electron storage viologens, we surveyed a number of designed two-electron storage viologen candidates (Figure 3-6) using DFT calculations to predict their redox potentials. These candidates were designed with at least one polar N-substituent, and a varied substituent on the second N atom. DFT calculations were conducted using the M06-2x functional and 6-31+G(d) bases sets with the SMD solvation model.

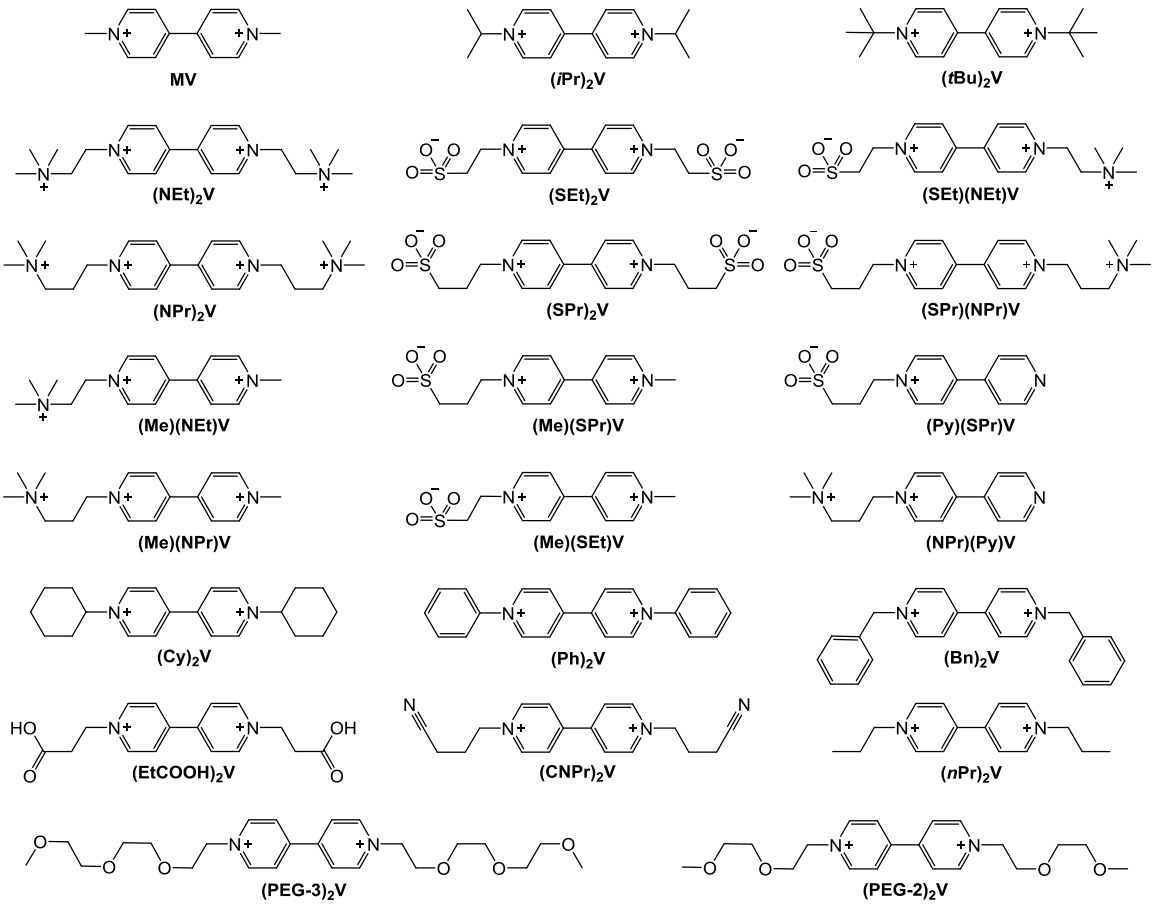

Viologen Derivative (H_2O)	$E°_{1st,calc}$ (V vs NHE)	$E°_{2nd,calc}$ (V vs NHE)	$E°_{1st,exp}$ (V vs NHE)	$E°_{2nd,exp}$ (V vs NHE)
MV	Ref.	Ref.	-0.45	-0.76
$(NPr)_2V$	-0.33	-0.64	-0.35	-0.72
$(PEG\text{-}3)_2V$	-0.30	-0.75	-0.38	-0.79
(NPr)(SPr)V	-0.36	-0.72	-0.37	-0.74
(Me)(NPr)V	-0.34	-0.73	-0.39	-0.78
$(PEG\text{-}2)_2V$	-0.30	-0.74	-0.37	-0.74
$(SPr)_2V$	-0.46	-0.73	-0.43	-0.79
Mean Unsigned Error (MUE)	-	-	37 mV	36 mV

Figure 3-6. (Top) Structural representations of designed two-electron storage viologen compounds used in DFT calculations. (Bottom) Comparison to synthesized viologens.

For the first-electron reduction of the viologens yielded an MUE of 37 mV with a lower and upper range of 10 to 80 mV error. The second-electron reduction showed an MUE of 36 mV with a lower and upper range 0 to 80 mV. The physical interpretation is to say a newly synthesized viologen derivative is likely have an experimental reduction potential within 37 mV of the predicted value, on average, and unlikely to be more than 80 mV from the theoretical. The calculated redox potentials (-0.36 and -0.72 V vs NHE) of **(NPr)(SPr)V** match well with the experimental (-0.37 V and -0.74 V), giving only 20 mV difference for both the first and second redox couples. This represents the lowest MUE for theoretical redox potentials for a given system to date, furthermore, without the need for any application of additional corrections.[13, 15, 17, 21, 33-34, 39, 46, 48-51]

For all candidates, the ground state structure was optimized for the initial oxidation state, one-electron reduced oxidation state, and two-electron reduced oxidation state.

The predicted redox potentials of six experimentally synthesized viologens were compared to their experimental redox potentials for comparison, as tabulated in Figure 3-6. The accuracy of the method used for this system can be realized by the calculation of the mean unsigned error (MUE) of the calculated redox potentials and the experimental redox potentials vs NHE for the experimentally synthesized viologen derivatives.

Theoretical Comparison of Redox Potentials and the Estimated Contribution of Disproportionation and Hydrogen Evolution During RFB Operation. To further strengthen the search for experimentally worthy viologen candidates, the comparison of the redox potentials along with disproportionation and hydrogen evolution factors should be evaluated. Thus, a comprehensive table below shows the theoretical redox potentials,

favorability of the disproportionation reaction, and thermodynamics of the hydrogen evolution for both redox states (Table 3-1).

(Ph)$_2$V with two phenyl electron-withdrawing substituents has the most positive predicted redox potentials at -0.21 and -0.49 V vs NHE for the first and second reductions, respectively. The ease of reduction predicted here is logical due to the strong withdrawing effects of the close-proximity phenyl substituents on the 4,4'-bipyridine, hence, making it much easier to transfer an additional electron to the ring system. **(SPr)$_2$V** and **(*n*Pr)$_2$V** have the most negative predicted redox potential values at -0.46 V vs NHE for the first electron, and **(*t*Bu)$_2$V** for the second electron at -0.73 V vs NHE, comparable to those of **MV**. However, **(SPr)$_2$V** is better suited for aqueous systems than **(nPr)$_2$V** since the solubility is likely to be much better due to being more ionic from the sulfate pendent arms. Viologens with mixed substituents possess negative redox potential values in between. One example is **(NPr)(SPr)V**, where the calculated redox potentials are -0.35 V and -0.72 V vs NHE for the first and second electrons, which corresponds within 20 mV of the experimental for both reductions (Figure 3-6).

The redox potentials for the two single-electron storage molecules, **(Py)(SPr)V** (-0.92 V vs NHE) and **(Py)(NPr)V** (-0.90 V vs NHE), appear to be outliers where the reduction potential for the singly-reduced state is much higher than the most negative doubly-reduced state of the two-electron storage molecules. While this large negative potential may still accurately reflect the experimental redox potential, it is deemed unlikely. This is probably due to the difference in electronic structure of the singly-substituted bipyridine in comparison to the calculated reference of MV, since the cancelation of error method relies on canceling out the uncertainties from ionic effects on the electrostatic term

in the implicit solvent. Conversely, as mentioned prior, the magnitude of error is unconfirmed and may still reflect the real redox potential, since this molecule has yet to be synthesized.

In further evaluating the designed viologen derivatives, a large cell voltage alone does not constitute an optimal viologen candidate; solubility and potential side reactions, such as the hydrogen evolution reaction, are also important factors to consider. As for the propensity of a newly designed viologen derivative to enable the hydrogen evolution reaction, the first and second reduced states were considered separately to account for multiple possible reaction pathways. As seen in Table 3-1, hydrogen evolution is an unfavorable process for all first-electron reduced states for the two-electron storage species by an average of 12.81 kcal/mol (excluding the single-electron storage molecules, **(Py)(SPr)V** and **(Py)(NPr)V**, for the reasons mentioned above). **$(SPr)_2$V** is the most thermodynamically favorable species to activate the hydrogen evolution reaction at 8.29 kcal/mol and **$(Ph)_2$V** is the most unfavorable at 20.06 kcal/mol, which is consistent with the predicted redox potentials. The data may indicate the reaction proceed to a small extent, in the case of **$(SPr)_2$V** and a few others, but this amount is unlikely to have a significant effect on the overall battery performance. These results seem reasonable considering that these singly-reduced species may not have a large enough reduction potential to initiate such a reaction.

The second-electron reduced state of all the calculated viologen derivatives were shown to have sufficient electronic potential to reduce protons dihydrogen in a favorable reaction of -12.81 kcal/mol on average (Table 3-1), which, coincidentally, calculated to be the exact opposite average degree of favorability as the singly-reduced species. The least

favorable of these species is the **(Ph)$_2$V** at -3.20 kcal/mol in relation to its small reduction potential, whereas the most favorable species is **(*i*Pr)$_2$V** with significant favorability of -18.88 kcal/mol. These values can explain some of the observed loss in performance for experimentally synthesized viologen derivatives used in AORFBs.[3, 41-42, 52]

While the second-electron reduced viologen derivates are considerably favorable towards the hydrogen evolution reaction, structural and intermolecular considerations must also be considered when evaluating hydrogen evolution in viologen derivatives. Such intermolecular interactions were not computationally modeled here, however, the dimerization of viologens have been known to occur in solution.[53-54] Additionally, Table 3-1 demonstrates singly-reduced viologen species are unfavorable towards hydrogen evolution, hence, a two-step proton reduction with a single doubly-reduced viologen is unreasonable since that would imply a favorable reduction of the first proton followed by a separate, unfavorable reduction of a second proton using the remaining singly-reduced viologen state ($1/2\ \Delta G_{2V+/2H+}$). Therefore, it was deemed reasonable that such a reaction is more likely to occur within the experimentally-observed dimerized adduct of a viologen derivative.[53-54] This two-step reduction process via a doubly-reduced dimerized viologen adduct is a much more thermodynamically favorable route for this pathway of energy loss with good or reasonable precedent.

Nevertheless, some viologens may dimerize more favorably. than others. As such, it is safe to assume that some viologens may show less coulombic efficiency in the second-electron reduced state than others, depending on its ability to dimerize. Since the dimerized adduct can perform both proton reductions in an exergonic process (Table 3-1), it is important to consider the intrinsic nature of the pendent arms. For example, negatively

charged pendent arms may decrease the ability to form a dimer. Additionally, bulky groups, such as **(*t*Bu)$_2$V** may experience dimerization to a lesser degree than MV, however, may exhibit decreased solubility in this case. Since the hydrogen evolution reaction results in increased concentration of the hydroxide anion, one could confirm the aforementioned conclusion by measuring the pH of the anolyte solution before and after continued cycling to the doubly-reduced charge state; the anolyte solution with the greater increase in pH is proposed to have experienced a greater degree energy loss through hydrogen evolution due to a greater degree of dimerization. Of course, the above would need be complemented by an in-depth DFT study on the free energies of dimerization and additional experimental post-analysis experiments on the AORFBs to confirm no crossover and anolyte degradation.

Another route singly-reduced viologens can access the hydrogen evolution is through disproportionation. Taking **MV** as an example, if only utilizing the singly-charged state in AORFB operation hydrogen evolution can still be a mode of energy loss via disproportionation to a ground state species and a doubly-reduced active species that can then go on to initiate the hydrogen evolution reaction.[53-55] According to Table 3-1, the most liable species to undergo disproportionation is **(Me)(NEt)V** at 10.33 kcal/mol while the most unfavorable is **(PEG-3)$_2$V** at 15.57 kcal/mol. For comparison, **(SPr)$_2$V** and **(NPr)$_2$V** have free energies of disproportionation of 11.28 and 13.33 kcal/mol, respectively. While these single-step reactions were all calculated to be unfavorable, they are still in equilibrium to some extent and may lead to slow hydrogen evolution via the Le Chatelier's principle. Any doubly-reduced specie can go on to reduce protons in a two-electron reduction with an overall change in free energy at a favorable -2.98 kcal/mol for **(SPr)$_2$V**

and overall uphill process of 3.09 kcal/mol for **(NPr)$_2$V**, further supporting the excellent experimental charge/recharge cycling efficiency seen for **(NPr)$_2$V**.[41-42]

Table 3-2 shows the same compounds found in Table 3-1 optimized in acetonitrile (MeCN). The free energies of the disproportionation reaction appear to have the similar trends to those solubilized in water, which was expected as there were no other differing parameters that would have significant effects on the process. The hydrogen evolution reaction was calculated to be much more limited in acetonitrile than in water, which good fit with experimental observations since the only proton donor in dry acetonitrile and it has a high pK_{HS} of 33.6 and a poor proton donor.[45-46] The poor proton donating properties of acetonitrile are reflected in the large uphill free energies for hydrogen evolution as seen in Table 3-2. For the two-electron storage species, **(SPr)$_2$V** is the most thermodynamically favorable towards hydrogen evolution at the singly-reduced state at 75.39 kcal/mol with the most negative reduction potential -0.51 V vs NHE, and **(NEt)$_2$V** is the least favorable at 95.86 kcal/mol with a reduction potential of -0.06 V vs NHE.

Table 3-1. Theoretical calculations of viologen derivatives in water. (1) The Gibbs free energies of the disproportionation reaction $2\ V^{+}_{(aq)} \rightarrow V^{0}_{(aq)} + V^{2+}_{(aq)}$, $\Delta G_{Disp.}$; (2) the free energies of the hydrogen evolution reaction, $2\ V^{+}_{(aq)} + 2\ H^{+}_{(aq)} \rightarrow 2\ V^{2+}_{(aq)} + H_{2(g)}$, $\Delta G_{2V+/2H+}$; (3) the free fnergies of the hydrogen evolution reaction, $2\ V^{0}_{(aq)} \rightarrow 2\ V^{+}_{(aq)} + H_{2(g)}$, $\Delta G_{2V0/2H+}$; (4) the theoretical reduction potential for the first electron vs NHE, $E°_{1st,calc}$; (5) the theoretical reduction potential for the first electron vs NHE, $E°_{2nd,calc}$. All calculations performed using M06-2x/6-31+G(d)/SMD.

Viologen Derivative (in H_2O)	$\Delta G_{Disp.}$ (kcal/mol)	$\Delta G_{2V+/2H+}$ (kcal/mol)	$\Delta G_{2V0/2H+}$ (kcal/mol)	$E°_{1st,calc}$ (V vs NHE)	$E°_{2nd,calc}$ (V vs NHE)
MV	12.37	8.96	-15.79	Ref.	Ref.
$(SPr)_2V$	11.28	8.29	-14.26	-0.46	-0.73
$(SEt)_2V$	10.96	10.89	-11.04	-0.41	-0.66
$(NPr)_2V$	13.33	14.53	-10.24	-0.33	-0.64
$(NEt)_2V$	12.51	19.53	-5.48	-0.22	-0.54
(NPr)(SPr)V	13.46	13.06	-13.85	-0.36	-0.72
(NEt)(SEt)V	13.11	16.21	-10.00	-0.29	-0.63
(Me)(SPr)V	12.48	11.04	-13.93	-0.40	-0.72
(Me)(SEt)V	12.26	9.97	-14.55	-0.43	-0.73
(Me)(NPr)V	14.16	13.81	-14.52	-0.34	-0.73
(Me)(NEt)V	10.33	12.79	-7.87	-0.37	-0.59
$(Ph)_2V$	11.63	20.06	-3.20	-0.21	-0.49
$(Cy)_2V$	13.47	9.46	-17.47	-0.44	-0.80
$(Bn)_2V$	12.53	12.33	-12.72	-0.38	-0.69
$(PEG\text{-}3)_2V$	15.57	15.80	-15.35	-0.30	-0.75
$(PEG\text{-}2)_2V$	15.48	15.89	-15.08	-0.30	-0.74
$(EtCOOH)_2V$	12.52	14.57	-10.48	-0.33	-0.64
$(i Pr)_2V$	15.48	12.09	-18.88	-0.38	-0.83
$(t Bu)_2V$	13.13	9.61	-16.65	-0.44	-0.78
$(CNPr)_2V$	12.58	11.81	-13.35	-0.39	-0.71
$(n Pr)_2V$	11.31	8.38	-14.24	-0.46	-0.73
(Py)(SPr)V	-	-12.84	-	-0.92	-
(Py)(NPr)V	-	-11.81	-	-0.90	-

Table 3-2. Theoretical calculations of viologen derivatives in MeCN. (1) The Gibbs free energies of the disproportionation reaction $2\ V^{+}_{(aq)} \rightarrow V^{0}_{(aq)} + V^{2+}_{(aq)}$, $\Delta G_{Disp.}$; (2) the free energies of the hydrogen evolution reaction, $2\ V^{+}_{(aq)} + 2\ H^{+}_{(aq)} \rightarrow 2\ V^{2+}_{(aq)} + H_{2(g)}$, $\Delta G_{2V+/2H+}$; (3) the free energies of the hydrogen evolution reaction, $2\ V^{0}_{(aq)} \rightarrow 2\ V^{+}_{(aq)} +$

$H_{2(g)}$, $\Delta G_{2V0/2H+}$; (4) the theoretical reduction potential for the first electron vs NHE, $E°_{1st,calc}$; (5) the theoretical reduction potential for the first electron vs NHE, $E°_{2nd,calc}$. All calculations performed using M06-2x/6-31+G(d)/SMD.

Viologen Derivative (in MeCN)	**$\Delta G_{Disp.}$ (kcal/mol)**	**$\Delta G_{2V+/2H+}$ (kcal/mol)**	**$\Delta G_{2V0/2H+}$ (kcal/mol)**	**$E°_{1st,calc}$ (V vs NHE)**	**$E°_{2nd,calc}$ (V vs NHE)**
MV	14.27	79.88	51.33	Ref.	Ref.
$(SPr)_2V$	13.96	75.39	47.48	-0.51	-0.94
$(SEt)_2V$	11.81	76.38	52.77	-0.49	-0.83
$(NPr)_2V$	14.58	89.41	60.25	-0.20	-0.67
$(NEt)_2V$	16.44	95.86	62.97	-0.06	-0.61
(NPr)(SPr)V	13.95	81.12	53.22	-0.38	-0.82
(NEt)(SEt)V	14.98	86.45	56.48	-0.27	-0.75
(Me)(SPr)V	13.86	79.46	51.73	-0.42	-0.85
(Me)(SEt)V	14.98	80.81	48.90	-0.39	-0.91
(Me)(NPr)V	14.43	84.44	55.58	-0.31	-0.77
(Me)(NEt)V	15.41	87.43	56.61	-0.25	-0.75
$(Ph)_2V$	11.69	89.13	65.74	-0.21	-0.55
$(Cy)_2V$	14.84	78.85	49.17	-0.43	-0.91
$(Bn)_2V$	16.61	86.20	52.97	-0.27	-0.82
$(PEG\text{-}3)_2V$	14.49	83.26	54.27	-0.34	-0.80
$(PEG\text{-}2)_2V$	17.66	88.88	53.55	-0.21	-0.81
$(EtCOOH)_2V$	11.09	79.38	57.21	-0.42	-0.73
$(iPr)_2V$	14.00	78.44	50.43	-0.44	-0.88
$(tBu)_2V$	13.50	79.98	52.99	-0.41	-0.82
$(CNPr)_2V$	14.50	83.35	54.36	-0.33	-0.79
$(nPr)_2V$	13.73	80.09	52.63	-0.41	-0.83
(Py)(SPr)V	-	51.85	-	-1.02	-
(Py)(NPr)V	-	54.92	-	-0.95	-

Of the one-electron storage species with a single pendent arm, **(Py)(SPr)V** has the overall most favorable towards hydrogen evolution with an uphill energy of 51.85 kcal/mol as well as the overall highest reduction potential at -1.02 V vs NHE. For the doubly-reduced derivatives, **$(SPr)_2V$** is the most favorable for hydrogen evolution with a change of free energy of 47.48 kcal/mol with the highest reduction potential of -0.94 V vs NHE, and **$(Ph)_2V$** is the least at 65.74 kcal/mol and a reduction potential of -0.55 V vs NHE. These trends are consistent with the theoretical predictions in water solvent with good correlation.

Summary

AORFBs are highly attractive for large-scale energy storage because redox organic molecules are synthetically tunable, sustainable, and potentially low-cost. Herein demonstrates that rational molecular engineering yielded a series of two-electron storage viologen molecules to be used as anolyte materials for AORFBs. At the fundamental level, DFT calculations proved to be a powerful tool in designing two-electron storage systems, offering insightful information on the chemical and electronic structures of three redox states of these two-electron storage molecules.

Calculating the electrostatic charge surface of **$(SPr)_2V$** and its charged state, **$[(SPr)_2V]^{-1}$**, reveals charge repulsion and size exclusion enable their compatibility with a cation exchange membrane. Furthermore, it was shown that the stability of these designed viologens in the one- and two-electron reduced states is due to the high charge delocalization of their frontier SOMO or HOMO.

To determine the best potential viologen candidates for synthesis, the thermodynamics of the hydrogen evolution reaction with these derivatives were calculated

by accounting for the autoprotolysis of water to more accurately model the free energies of the reaction. The results were consistent with observed efficiencies in aqueous and non-aqueous systems. For these two-electron storage molecules, the first electron-reduced derivatives could not favorably reduce water while the second-electron reduced states were shown to do so favorably. However, the well-known dimerization of viologens may increase or decrease the thermodynamics of this process and may largely depend on the functional pendent arms. A future study of these dimer adducts and transition states would be a nice complement to this investigation that could be a great molecular engineering tool in addition to the ones provided here. In the case of unstable doubly-reduced derivatives, undesirable hydrogen evolution can be accessed in the first-electron reduction through the disproportionation reaction to obtain the more negative redox couple of the doubly-reduced specie. For all molecules, disproportionation was shown to be an unfavorable reaction, nevertheless, these reactions are in equilibrium in solution and may slowly generate hydrogen. The trends presented here for disproportionation provided insightful indications as to which derivatives are more likely lose energy due to hydrogen evolution compared to others.

Calculation of the theoretical reduction potentials relative to the internal standard, MV, proved to be a powerful method yielding the lowest MUE to the experimental (37 and 36 mV for the first and second reductions, respectively) of any given system to date. To highlight a derivative, the calculated reduction potentials (-0.36 and -0.72 V vs NHE) of **(NPr)(SPr)V** match well with the experimental (-0.37 V and -0.74 V), giving only 20 mV difference for both the first and second redox couples. Reduction potentials in acetonitrile were also calculated for general interest in regards to NAORFBs.

The largest source of error in the calculation reduction potentials for these viologen derivatives is likely due to ionic effects of the solution not being considered, along with the previously discussed sources of error. The magnitude of this error is dependent on the intrinsic nature of the various pendent arm substituents; *i.e.*, a charge-neutral derivative, such as **(SPr)$_2$V**, may give a different amount of error cancelation than a positively charged specie, such as **(NPr)$_2$V**, based on the selection of the relative explicit reference molecule $[MV]^{2+}$. The excellent agreement between the theoretical reduction potentials and the experimental potentials observed in this research is contributed to the choice of the explicit reference molecule, MV, as part of the molecular engineering employed in this research. This choice was based on MV's median similarity to the other designed viologen derivatives electronically and geometrically, especially in the location of reduction as well as the number of reductions available, thereby eliminating a substantial amount of systematic computational error. To bolster Truhlar's claim concerning the choice of such reference molecules[21], future studies should aim to enact the same framework when using the cancelation of systematic errors method through relative reduction potentials in choosing the appropriate reference molecule.

The synthetic and computational chemistry presented here has opened a new avenue of viologen derivatization for building AORFBs with high voltage, high power density, and high energy density which promises economical and widespread use of RFBs in large-scale energy storage. The presented research highlights the art of molecular engineering as a powerful tool for developing energy-dense redox-active electrolyte materials for RFBs.

References

1. Lin, K.; Gómez-Bombarelli, R.; Beh, E. S.; Tong, L.; Chen, Q.; Valle, A.; Aspuru-Guzik, A.; Aziz, M. J.; Gordon, R. G. *Nature Energy* **2016**, *1*, 16102.
2. Janoschka, T.; Martin, N.; Hager, M. D.; Schubert, U. S. *Angew. Chem. Int. Ed.* **2016**, *55*, 14427-14430.
3. Hu, B.; DeBruler, C.; Rhodes, Z.; Liu, T. L. *J. Am. Chem. Soc.* **2017**, *139*, 1207-1214.
4. Huskinson, B.; Marshak, M. P.; Gerhardt, M. R.; Aziz, M. J. *ECS Trans.* **2014**, *61*, 27.
5. Leung, P.; Martin, T.; Liras, M.; Berenguer, A. M.; Marcilla, R.; Shah, A.; An, L.; Anderson, M. A.; Palma, J. *Applied Energy* **2017**, *197*, 318-326.
6. Frisch, M. J. **2009**.
7. Krishnan, R.; Binkley, J. S.; Seeger, R.; Pople, J. A. *J. Chem. Phys.* **1980**, *72*, 650-654.
8. Mclean, A. D.; Chandler, G. S. *J. Chem. Phys.* **1980**, *72*, 5639-5648.
9. Zhao, Y.; Truhlar, D. G. *Acc. Chem. Res.* **2008**, *41*, 157-167.
10. Zhao, Y.; Truhlar, D. G. *Theor. Chem. Acc.* **2008**, *120*, 215-241.
11. Zhao, Y.; Truhlar, D. G. *Chem. Phys. Lett.* **2011**, *502*, 1-13.
12. Marenich, A. V.; Cramer, C. J.; Truhlar, D. G. *J. Phys. Chem. B* **2009**, *113*, 6378-6396.
13. Li, J.; Fisher, C. L.; Chen, J. L.; Bashford, D.; Noodleman, L. *Inorg. Chem.* **1996**, *35*, 4694-4702.
14. Heinz, H.; Suter, U. W. *J. Phys. Chem. B* **2004**, *108*, 18341-18352.

15. Roy, L. E.; Jakubikova, E.; Guthrie, M. G.; Batista, E. R. *J. Phys. Chem. A* **2009**, *113*, 6745-6750.

16. Dutton, A. S.; Fukuto, J. M.; Houk, K. N. *Inorg. Chem.* **2005**, *44*, 4024-4028.

17. Roy, L. E.; Batista, E. R.; Hay, P. J. *Inorg. Chem.* **2008**, *47*, 9228-9237.

18. Paukku, Y.; Hill, G. *J. Phys. Chem. A* **2011**, *115*, 4801-4810.

19. Ho, J.; Ertem, M. Z. *J. Phys. Chem. B* **2016**, *120*, 1319-1329.

20. Lewis, G. N.; Randall, M.; Pitzer, K. S.; Brewer, L. *Thermodynamics; McGrawHill: New York* **1961**, 353.

21. Ho, J.; Coote, M. L.; Cramer, C. J.; Truhlar, D. G. *O. Hammerich, B. Speiser (Eds.), Organic Electrochemistry (5th edition), Taylor and Francis Group* **2015**, 229-259.

22. Sawyer, D. T.; Sobkowiak, A.; Roberts, J. L. *Electrochemistry for Chemists (2nd ed.); Wiley: New York* **1995**, 192.

23. Goerigk, L.; Grimme, S. *PCCP* **2011**, *13*, 6670-6688.

24. Kruse, H.; Goerigk, L.; Grimme, S. *J. Org. Chem.* **2012**, *77*, 10824-10834.

25. Cances, M. T.; Mennucci, B.; Tomasi, J. *J. Chem. Phys.* **1997**, *107*, 3032-3041.

26. Cossi, M.; Rega, N.; Scalmani, G.; Barone, V. *J. Comput. Chem.* **2003**, *24*, 669-681.

27. Barone, V.; Cossi, M. *J. Phys. Chem. A* **1998**, *102*, 1995-2001.

28. Cramer, C. J.; Truhlar, D. G. *Acc. Chem. Res.* **2009**, *42*, 493-497.

29. Marenich, A. V.; Olson, R. M.; Kelly, C. P.; Cramer, C. J.; Truhlar, D. G. *J. Chem. Theor. Comput.* **2007**, *3*, 2011-2033.

30. Marenich, A. V.; Cramer, C. J.; Truhlar, D. G. *J. Chem. Theor. Comput.* **2009**, *5*, 2447-2464.

31. Qu, X.; Persson, K. A. *J. Chem. Theor. Comput.* **2016**, *12*, 4501-4508.

32. Wertz, D. H. *J. Am. Chem. Soc.* **1980**, *102*, 5316-5322.

33. Fawcett, W. R. *Langmuir* **2008**, *24*, 9868-9875.

34. Kuznetsov, A. M.; Maslii, A. N.; Krishtalik, L. I. *Russ. J. Electrochem.* **2008**, *44*, 34-42.

35. Kelly, C. P.; Cramer, C. J.; Truhlar, D. G. *J. Phys. Chem. B* **2006**, *110*, 16066-16081.

36. Hünenberger, P.; Reif, M. *Single-Ion Solvation: Experimental and Theoretical Approaches to Elusive Thermodynamic Quantities; RSC Publishing: Cambridge, U.K.* **2011**.

37. Sokhan, V. P.; Tildesley, D. *J. Mol. Phys.* **1997**, *92*, 325-640.

38. Randles, J. E. B. P. C. L., 7, 107–179. *Phys. Chem. Liq.* **1977**, *7*, 107-179.

39. Castro, L.; Bühl, M. *J. Chem. Theor. Comput.* **2014**, *10*, 243-251.

40. Nishinaga, T. *Organic Redox Systems: Synthesis, Properties, and Applications; John Wiley & Sons* **2015**.

41. DeBruler, C.; Hu, B.; Moss, J.; Luo, J.; Liu, T. B. *ACS Energy Lett.* **2018**, *3*, 663-668.

42. DeBruler, C.; B., H.; Moss, J.; Liu, X.; Luo, J.; Sun, Y.; Liu, T. L. *Chem* **2017**, *3*.

43. Silverstein, T. P. H., S. T. *J. Chem. Educ.* **2017**, *94*, 690-695.

44. Fonrodona, G.; Rafols, C.; Bosch, E.; Roses, M. *Anal. Chim. Acta* **1996**, *335*, 291-302.

45. Sanli, S.; Altun, Y.; Sanli, N.; Alsancak, G.; Beltran, J. L. *J. Chem. Eng. Data* **2009**, *54*, 3014-3021.

46. Ertokus, G. P.; Aktas, A. H. *Asian J. Chem.* **2008**, *20*, 3042-3048.

47. Schmidt-Rohr, K.; Chen, Q. *Nat. Mater.* **2008**, *7*, 75-83.

48. Lee, S. Y. *Bull. Korean Chem. Soc.* **2015**, *36*, 443-444.

49. Namazian, M.; Coote, M. L. *J. Phys. Chem. A* **2007**, *111*, 7227-7232.

50. Bruschi, M.; Breglia, R.; Arrigoni, F.; Fantucci, P.; Gioia, L. D. *Int. J. Quantum Chem.* **2016**, *116*, 1695-1705.

51. Namazian, M.; Lin, C. Y.; Coote, M. L. *J. Chem. Theor. Comput.* **2010**, *6*, 2721-2725.

52. Hu, B.; Seefeldt, C.; DeBruler, C.; Liu, T. *J. Mat. Chem. A* **2017**, *139*, 1207-1214.

53. Kosower, E. M.; Cotter, J. L. *J. Am. Chem. Soc.* **1964**, *86*, 5524-5527.

54. Zhang, D.-W.; Chen, J. T. L.; Zhang, L.; Li, Z.-T. *Chem. Asian J.* **2014**, *10*, 56-68.

55. Wolszczak, M.; Stradowski, C. *Radiat. Phys. Chem.* **1989**, *33*, 355-359.

CHAPTER IV

IRON(II)-MEDIATED ELECTROCATALYTIC HYDROGEN EVOLUTION AND MULTI-ELECTRON REDUCTION OF CO_2 IN NON-AQUEOUS SYSTEMS

Abstract

In efforts to progress technology in recyclable fuels, we report the synthesis of an iron(II)-polypyridine complex with two pendent amines that enables electrochemical and photochemical reduction of CO_2 to CO, formic acid, and methane. Furthermore, this complex was found to catalyze the hydrogen evolution reaction with a TOF upwards of 120,000 s^{-1}. The characterization of the newly synthesized Fe(bapbpy)$(OTf)_2$ catalyst includes a complete paramagnetic proton resonance assignment using 1D and 2D NMR techniques, X-ray crystallography, FTIR, UV-vis, cyclic voltammetry, Mössbauer spectroscopy, and elemental analysis. The electronic properties were investigated with Evans method and Mössbauer spectroscopy revealing four unpaired electrons, consistent with a distorted pseudo-octahedral geometry, and spin-crossover properties were also observed. Ongoing efforts are being made to optimize the electrochemical and photochemical reduction of CO_2 for methane selectivity.

Introduction

Escaping the vicious cycle of increased fossil fuel consumption and depleting economically-accessible oil reserves[1-2] requires new technologies to convert CO_2 to reusable, high-energy products. While considerable progress has been made toward the electrocatalytic reduction of CO_2, very few have investigated the amine proton relay moiety

in catalytic design with iron metal centers.[3] It has been shown that the Fe(bapbpy)$(OTf)_2$ catalyst can reduce CO_2 beyond the two-electron reduction products yielding formaldehyde and methanol.[4-9] While there have been no reported homogenous catalysts that can reduce CO_2 to methane electrochemically, a recent study reveals the first homogenous molecular catalysts able to achieve this conversion photochemically using iron-porphyrin complexes and a photosensitizer.[10-11] Additionally, bipyridyl-based catalysts have exhibited robust behavior in their ability to reduce CO_2 electrochemically and also photochemically in the presence of a photosensitizer.[8, 11]

In this study, we developed a homogenous molecular iron catalyst for the electrochemical reduction of CO_2 by utilizing two pendent amine proton relays coupled with a polypyridine backbone to enable multi-electron reduction of CO_2. The details of the characterization of the newly synthesized Fe(bapbpy)$(OTf)_2$ complex including paramagnetic resonance assignments via 1D and 2D NMR techniques, proton source optimizations of the electrocatalytic reduction of CO_2, and the photochemical reduction of CO_2 using visible light in the presence of a photosensitizer are reported. Our results show the formation of CO and CH_4 from the electrocatalytic and photocatalytic conversion of CO_2. This represents the first electrochemical conversion of CO_2 to CH_4 by a homogenous molecular catalyst.[12] Additionally, Fe(bapbpy)$(OTf)_2$ was shown to catalyze the hydrogen evolution reaction at a high TOF.

Experimental

General Methods. All reagents and solvents were obtained from commercial sources and were used as received unless specified otherwise. Solvents were further dried

and degassed using an Inert PureSolv MD solvent system and stored over 3 Å molecular sieves. Chemicals and solvents were stored in a Vigor SciLab glovebox station under an atmosphere of argon where oxygen is below 1 ppm and water below 0.01 ppm. All reactions were done using an inert atmosphere of argon in the glovebox or using proper Schlenk techniques in a nitrogen atmosphere. N-(6-(6-(pyridin-2-ylamino)pyridin-2-yl)pyridin-2-yl)pyridin-2-amine (bapbpy) was synthesized according to the literature under an atmosphere of nitrogen using Schlenk techniques.[13-14] The purity of the ligand was confirmed by comparing the ^{1}H NMR spectra to the referenced literature.[14]

The $Fe(MeCN)_2(OTf)_2$ precursor was prepared according to literature procedures.[15] This reaction was performed in the glovebox as this compound was found to be air-sensitive as exposure to air results in the formation of a brown Fe(III) species. The color was consistent to that described by the literature. A light, blue-green precipitate was formed upon evaporation of the solvent via a flow of nitrogen corresponding to $Fe(MeCN)_4(OTf)_2$. The removal of two coordinated acetonitrile ligands was achieved by applying a vacuum for 24 h yielding a fine white powder corresponding to $Fe(MeCN)_2(OTf)_2$.[15]

Physical Methods. General. UV-visible spectra were collected in the glovebox under an argon atmosphere using an Ocean Optics Flame-S-XR1 Sony ILX511B CCD diode array spectrophotometer equipped with an Ocean Optics DH-mini UV-Vis-NIR light source. Each spectrum was recorded using 128 scans at 200 ms exposure per scan and a boxcar averaging of 4. IR spectra were recorded on a PerkinElmer Spectrum 100 FT-IR spectrometer with an attenuated total reflectance (ATR) attachment using a pure powder. Elemental analysis was performed by Atlantic Microlabs of Norcross, GA using a PE2400 automatic analyzer. Mössbauer spectra were recorded with two spectrometers using Janis

Research (Wilmington, MA) SuperVaritemp dewars in the temperature range from 4.0 K to 100 K with zero applied magnetic field. Mössbauer spectral simulations were performed using the WMOSS software package (SEE Co., Edina, MN). Gas chromatography was done on a Shimadzu GC-8A fitted with a TCD for H_2 quantification and a Shimadzu GC-8A fitted with an FID for CO and CH_4 quantification. Retention times for each gas were determined using standardized samples containing a solution of 10 mL 0.1 M $TBAPF_6$ in dry MeCN in a 20 mL septum vial that has been purged with CO_2 and injected with a standard target gas.

X-Ray Crystallography. Crystals obtained in a vial containing the mother liquor was sealed and sent to the University of Montana in Bozeman, MT. X-ray diffraction data were collected at 100 K on a Bruker D8 Venture using Mo Kα-radiation (λ = 0.71073 Å). Data have been corrected for absorption using SADABS[16] area detector absorption correction program. Using Olex2[17], the structure was solved with the SHELXT[18] structure solution program using Direct Methods and refined with the SHELXL[19] refinement package using least squares minimization. All non-hydrogen atoms were refined with anisotropic thermal parameters. Hydrogen atoms attached to heteroatoms were found from the residual density maps, placed, and refined with isotropic thermal parameters. All other hydrogen atoms in the investigated structure were located from difference Fourier maps but were placed in geometrically calculated positions and refined using a riding model. Isotropic thermal parameters of the placed hydrogen atoms were fixed to 1.2 times the U value of the atoms they are linked to, and 1.5 for methyl groups. Calculations refinement of structures were carried out using APEX2[20], SHELXTL[21], and Olex2 software.

NMR Methods. All NMR spectra were recorded on a Bruker Avance III HD Ascend-500 NMR spectrometer (proton at 500 MHz). The temperature was set to 298 K. Chemical shifts were referenced to the residual solvent peak(s) of C*H*D_2CN (^{1}H, 1.94 ppm, pentet). A typical one-dimensional ^{1}H NMR spectrum consists of 64K data points, 512 scans, a 250 ms relaxation delay, and an acquisition time of 3.0 seconds. The 90° pulse of 8.9 μs was calibrated at 298 K. Longitudinal relaxation times (T_1) were measured using the inversion-recovery pulse sequence (180°-τ-90°) method. Two-dimensional ^{1}H DQF-COSY spectra were obtained at 298 K in CD_3CN using a 60° pulse of 10.0 μs, 1024 data points for the F1 dimension, 2048 data points for the F2 dimension, a relaxation delay of 2.0 s, and sine function processing. Magnetic susceptibility was determined by the Evans method at 298 K.[22]

Electrochemical Methods. Cyclic voltammetry (CV) experiments were performed with a Gamry Interface 1000 Potentiostat using a three-electrode setup with a Ag/AgCl reference electrode, a polished 3 mm glassy carbon working electrode, and a glassy carbon counter electrode, and a scan rate of 50 mV/s unless specified otherwise. Solutions contained 0.1 M $TBAPF_6$ supporting electrolyte in dry MeCN with 0.5 mM catalyst. The atmosphere of the vessel was purged with nitrogen to remove any solubilized oxygen. Bulk electrolysis experiments were run using a three-cell set up with an Ag/AgCl reference electrode, a glassy carbon rod working electrode, and a graphite rod counter electrode with 0.1 M $TBAPF_6$ supporting electrolyte in dry MeCN with 0.5 mM catalyst. Sealed reaction vessels were purged with nitrogen for the hydrogen evolution reaction and carbon dioxide for the CO_2 reduction experiments. Before each experiment, the glassy-carbon working electrode was polished with a felt pad with 0.05 μm alumina MicroPolish powder (CH

Instruments, Inc.) dampened with deionized water, and then rinsed with deionized water and dried with a Kimwipe. Nonaqueous electrolyte solutions were stored over 3 Å molecular sieves that had been recently activated in a 350 °C oven for at least 24 h and stored in air-tight containers. The overpotential for CO_2 reduction with PhOH as a proton source was calculated with Eqs 4-1 and 4-2,

$$\eta = E_{Peak} - E \tag{4-1}$$

$$E = E° - 0.0592pKa \tag{4-2}$$

where the E_{peak} is the observed peak catalytic current and the pKa used for PhOH in acetonitrile was 29.14 for reasons outlined in Kutt. *et al.*[23-24] The pKa used for PhOH in DMF was 15.40.[25]

Photochemical Methods. Visible light-driven photochemical reduction of CO_2 was performed in a 20 mL septum-sealed glass vial containing 0.5 mM Fe(bapbpy)$(OTf)_2$, 20 mM phenol as a proton donor, 0.5 mM $Ir(ppy)_3$ as a photosensitizer, and 50 mM TEA as a sacrificial electron donor in MeCN dried with 3 Å molecular sieves. The sample was further sealed with tape and illuminated with visible light (>420 nm) for 72 h from a Newport 66921 lamp equipped with a Newport 68950 Digital Exposure Controller with a UV-light filter.

Synthesis of Fe(bapbpy)$(OTf)_2$. The complete synthesis of the Fe(bapbpy)$(OTF)_2$ complex was performed in the glovebox under an argon atmosphere. In a 100 mL round bottom flask, N-(6-(6-(pyridin-2-ylamino)pyridin-2-yl)pyridin-2-yl)pyridin-2-amine (bapbpy) (0.628 mg, 1.44 mmol) was added to $Fe(MeCN)_2(OTf)_2$ (0.490 mg, 1.44 mmol) in 75 mL dried MeCN. This produced a red-orange mixture that was stirred for 3 h at room temperature. The solvent was removed under reduced pressure until *ca.* 10 mL remained

which resulted in the formation of a yellow precipitate in a dark brown-red solution. The precipitate was allowed to settle and the solvent was removed by pipette, and then the precipitate was washed with diethyl ether (3 x 5 mL). The yellow crystals were dried by vacuum for 24 h (780 mg, 78% yield). Crystals suitable for single crystal X-ray diffraction were obtained via slow diffusion of diethyl ether into an MeCN solution of Fe(bapbpy)$(OTf)_2$ at ambient temperature yielding yellow monoclinic crystals. ^{1}H NMR (CD_3CN, 500 MHz): δ 75.78 (br s, 2H), 64.56 (s, 2H), 61.08 (s, 2H), 42.23 (s, 2H), 29.64 (s, 2H), 10.61 (s, 2H), 8.28 (s, 2H), 7.05 (s, 2H). Elemental analysis calculated for $C_{22}H_{16}F_6FeN_6O_6S_2$: C, 38.06; H, 2.32; N, 12.10; found: C, 38.18; H, 2.23; N, 12.13. UV-vis [CH_3CN; nm, (ϵ, M^{-1} cm^{-1})]: 418 (183), 474 (292), 580 (34). ATR-FTIR (cm^{-1}): 3318 (ν_{ss}N-H), 3217 (ν_{b}N-H), 3153 (ν_{ss}C-H), 3060 ($\nu_{C=H}$), 1639 ($\nu_{C=C}$), 1586 ($\nu_{C=C}$), 1538 ($\nu_{C=C}$), 1489 ($\nu_{C=C}$), 1466 ($\nu_{C=C}$), 1449 ($\nu_{C=C}$), 1374 (ν_{SO2})[26-27], 1294 (ν_{as}SO2)[26], 1222 (ν_{ss}CF3)[26], 1164 (ν_{as}CF3)[26], 1029 (ν_{ss}SO2)[26], 1011 (ν_{as}CF3)[28]. μ_{eff} (298 K) = 4.9(7) μ_B.

Results and Discussion

Characterization of Fe(bapbpy)$(OTf)_2$. In pursuit of a bifunctional iron catalyst that can do both CO_2 reduction and hydrogen evolution, an iron polypyridine-based catalyst, Fe(bapbpy)$(OTf)_2$, was synthesized (Scheme 4-1). The catalyst was prepared in 78% yield via treatment of bapbpy with an equimolar amount of $Fe(MeCN)_2(OTf)_2$ under an inert atmosphere followed by recrystallization from MeCN/Et_2O. While the bapbpy ligand (Scheme 4-1) is known, the iron(II)-bapbpy triflate complex has never been characterized as the previous work was aimed at spin-crossover property studies of the thiocyanide-coordinated compound.

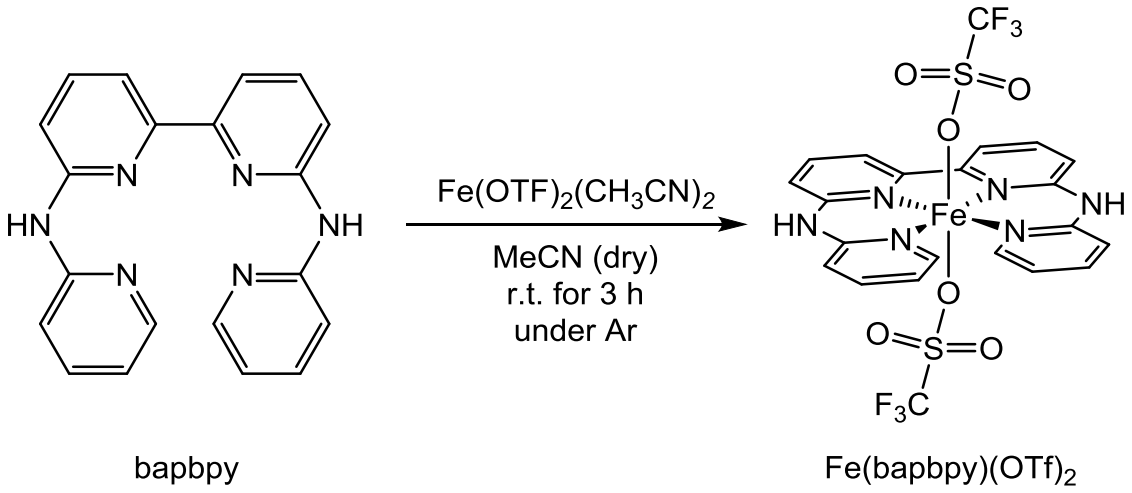

Scheme 4-1. Synthesis of Fe(bapbpy)(OTf)$_2$.

However, use of a weaker coordinating and more electrochemically stable counterion is theorized here to exhibit functional capability towards CO_2 reduction by opening up two available coordination sites on the iron metal center. A portion of the work performed here focuses on the synthesis and structural characterization of the Fe(bapbpy)(OTf)$_2$ complex, which includes X-ray crystallography, one- and two-dimensional ^{1}H NMR, UV-vis, ATR-FTIR, CV, and elemental analysis. A detailed ^{1}H NMR peak assignment was developed using experimentally determined T_1 values in Solomon's equations and correlated to a two-dimensional ^{1}H DQCOSY spectrum. Evans method was used to characterize the magnetic susceptibility of the coordination complex.[22]

The complex was characterized by single-crystal X-ray crystallography with the results given in Table 4-1. The structure of Fe(bapbpy)(OTf)$_2$ is shown in Figure 4-1 revealing both triflate anions coordinating to the iron(II) center in the solid state. The average basal Fe-N bond length of 2.1198(13) Å for Fe(bapbpy)(OTf)$_2$ is slightly shorter

than the previously reported Fe(bapbpy)$(NCS)_2$ complex with an average basal Fe-N bond length of 2.1469(15) Å.[14]

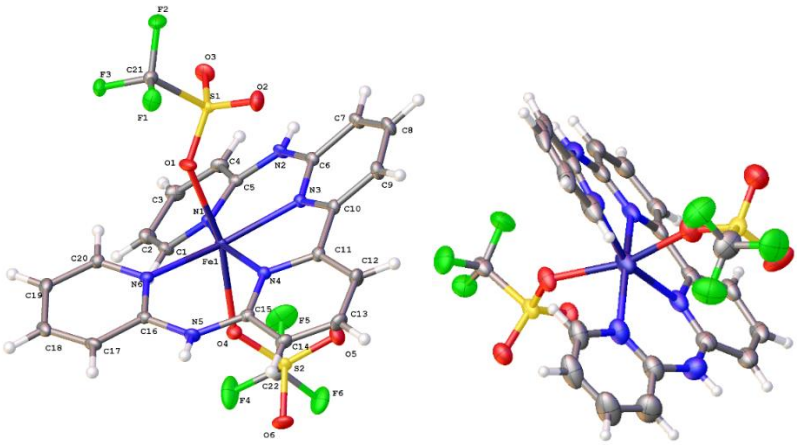

Figure 4-1. Representation of Fe(bapbpy)$(OTf)_2$ from single-crystal XRD. Left: (*R*) axial chirality. Right: (*S*) axial chirality. Ellipsoids are plotted at the 50% probability level.

This contraction is explained by the increased Lewis acidity of the Fe(II) center due to the coordination of the weakly donating triflate anion with a Fe-OTf bond length of 2.2284(12) Å compared to the shorter Fe-NCS length of 2.1350(15) Å. The basal coordination angles range from 85.96° to 111.25° exhibiting slightly less distortion compared to the Fe(bapbpy)$(NCS)_2$ complex with a range of 77.34(8)° to 113.78(9)°. The smaller distortion can be attributed to the smaller extent of π-π overlap due to the larger size of the triflate anion in comparison to the smaller NCS anion.[14] This is reflected in the bonding distances of the counteranion and the amine proton on the ligand where Fe(bapbpy)$(OTf)_2$ has an average distance of 2.09365(8) Å (Figure 4-3) whereas Fe(bapbpy)$(NCS)_2$ is 2.58(2) Å.[14]

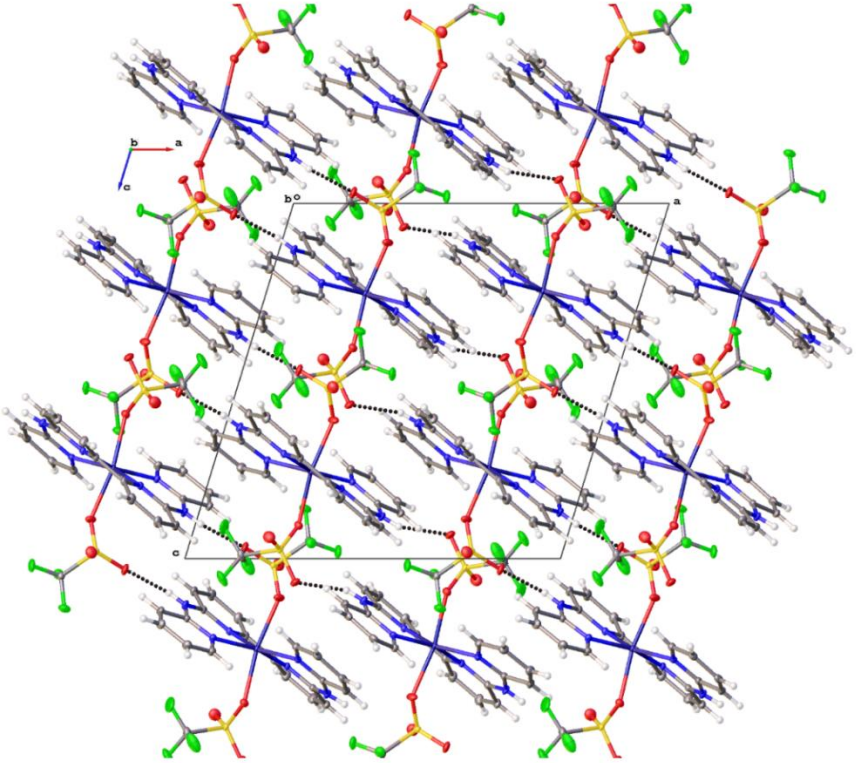

Figure 4-2. Representation of Fe(bapbpy)$(OTf)_2$ crystal layers as determined by single-crystal X-ray crystallography data. Ellipsoids are plotted at the 50% probability level.

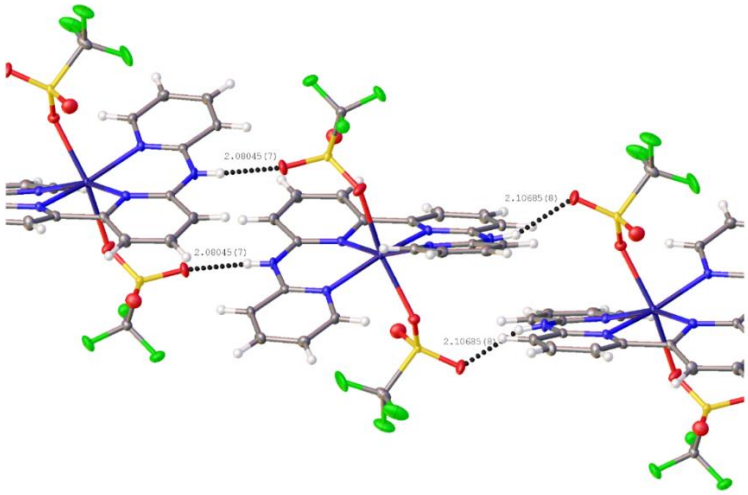

Figure 4-3. Representation of chiral-alternating crystal packing and corresponding hydrogen-bond lengths.

Table 4-1. Summary of X-Ray Crystallography Data and Structural Refinement for Fe(bapbpy)$(OTf)_2$.

Empirical formula	$C_{22}H_{16}F_6FeN_6O_6S_2$
Formula weight	694.38
Temperature (K)	100
Crystal system	monoclinic
Space group	$P2_1/c$
a (Å)	14.9582(6)
b (Å)	12.0697(5)
c (Å)	14.8013(6)
α (deg)	90
β (deg)	106.9970(10)
γ (deg)	90
V (Å^3)	2555.52(18)
Z	4
Density (calcd), g/cm^3	1.805
μ (mm^{-1})	0.851
F (000)	1400.0
Crystal size (mm^3)	0.2 × 0.18 × 0.12
Radiation used	Mo Kα (λ = 0.71073 Å)
Diffractometer	Bruker D8 Venture
2Θ range for data collection (deg)	6.522 to 63.206
Index ranges	$-22 \leq h \leq 22$, $-17 \leq k \leq 17$, $-21 \leq l \leq 21$
Reflections collected	132085
Independent reflections	8562 [R_{int} = 0.0550, R_{sigma} = 0.0259]
Data/restraints/parameters	8562/0/396
Goodness-of-fit on F^2	1.123
Final R indexes [I>=2σ (I)]	R_1 = 0.0411, wR_2 = 0.0819
Final R indexes [all data]	R_1 = 0.0585, wR_2 = 0.0889
Largest difference (e Å^{-3})	1.18/-0.42

Overall, the mononuclear Fe(II) complex exhibits a distorted pseudo-octahedral geometry with the bapbpy ligand bent out of the plane, demonstrating (*R*) axial chirality (Figure 4-1, left). Close examination of the crystal packing (Figure 4-2) reveals lattice layers that alternate between the (*R*) and (*S*) enantiomers. This phenomenon was confirmed in a second crystal obtained for single-crystal X-ray crystallography (Figure 4-1, right). This alternating chiral-layering suggests solution-phase chirality is in rapid equilibrium and

solid-state chirality is determined by the initial geometry assumed during crystal formation yielding chiral-selective lattice layering, as seen in Figures 4-2 and 4-3.

Table 4-2. Selected Bond Distances (Å) and Angles (deg) for Fe(bapbpy)$(OTf)_2$.[a]

Fe–O(1)	2.2253(12)	O(1)–Fe–O(4)	165.48(4)
Fe–O(4)	2.2315(12)	N(1)–Fe–O(1)	96.92(5)
Fe–N(1)	2.1163(13)	N(1)–Fe–O(4)	86.81(5)
Fe–N(3)	2.1265(13)	N(1)–Fe–N(3)	85.96(5)
Fe–N(4)	2.1139(13)	N(1)–Fe–N(6)	111.25(5)
Fe–N(6)	2.1225(13)	N(3)–Fe–O(1)	86.54(5)
H(2)···O(3) [b]	2.08045(17)	N(3)–Fe–O(4)	107.77(5)
H(5)···O(6) [b]	2.10685(8)	N(4)–Fe–O(1)	96.15(5)
Fe-H(α)[c]	4.95564	N(4)–Fe–O(4)	84.62(5)
Fe-H(α')[c]	4.99324	N(4)–Fe–N(1)	159.03(5)
Fe-H(β)[c]	5.79552	N(4)–Fe–N(3)	78.52(5)
Fe-H(β')[c]	5.83491	N(4)–Fe–N(6)	86.92(5)
Fe-H(γ)[c]	5.13877	N(6)–Fe–O(1)	81.24(5)
Fe-H(γ')[c]	5.15467	N(6)–Fe–O(4)	84.32(5)
Fe-H(λ)[c]	4.14963	N(6)–Fe–N(3)	159.88(5)
Fe-H(λ')[c]	2.95367		

[a] Estimated standard deviations in the last significant figure is given in parentheses.
[b] Hydrogen bonding distance between the (S) and (R) enantiomers in crystal stacking.
[c] Proton assignments in Table 4-3 and Figure 4-4.

Assignment of Resonances. Fe(bapbpy)$(OTf)_2$ is a high spin compound that displayed paramagnetic signatures in its ^{1}H NMR spectrum (Figure 4-4). Spectral assignments of Fe(bapbpy)$(OTf)_2$ were determined by 2D ^{1}H DQF-COSY and measured T_1 values (see Figure 4-5 and Table 4-3). The COSY spectrum shows coupling to six protons with two different spin systems correlating to the ^3J coupling within the two different aromatic rings in bapbpy (Figure 4-5). The two spin systems are shown in Figure 4-5 with the light-blue and red connecting lines representing which protons couple together. The intensity of these correlations is weak causing the *ortho* position on the

terminal ring to not show coupling. The weak correlations can be attributed to two primary reasons, the first being extremely short spin-lattice relaxation times (T_1). As seen from Table 4-3, T_1 values exhibit a large range from 21.94 ms to 0.2 ms. These short relaxation times are due to the paramagnetic metal center giving two prominent relaxation mechanisms: dipolar relaxation and contact relaxation.[29-30] Dipolar (pseudocontact) relaxation is a through-space relaxation that occurs between two point-dipoles in which orientational changes relative to each other induces spin transitions that allow new relaxation pathways. Contact (Fermi contact) relaxation is conveyed through molecular orbitals that develops from the interaction between the nuclear magnetic moment of the proton and unpaired electron delocalization over the proton nucleus.[31]

The second cause for the observed weak coupling correlations arise from the large spectral width of the experiment causing the appropriate 90° pulse length for the protons to differ. Since the resonance frequency with a large offset frequency experiences weaker excitation power than those with a small offset frequency, signals near the transmitter frequency tilt 90° while those further away tilt only *ca.* 20° in this case. This small tilt angle combined with the fast spin-lattice relaxation times greatly diminishes coupling magnetization from building. Hence, explaining why the *ortho* proton on the terminal bapbpy pyridine ring was not able to be resolved in the DQF-COSY spectrum.

To distinguish between the two spin systems and give correct T_1 assignments to each resonance, we utilized the relationships present between the T_1 values of each proton and their distance from the paramagnetic metal center obtained from X-ray crystallography. Following the methodology established by Swift, Bertini, and Luchinat the appropriate T_1 values were assigned to each proton using relationships derived from the

Solomon equation, that is, the spin-lattice relaxation time is directly proportional to the sixth power to the distance (r) between the metal center and the atom in question where T_1 α r^6.[32-34] Therefore, each measured T_1 value was assigned directly by correlating the increasing metal-proton distance to increasing T_1 times in sequential order, respectively, as seen in Table 4-3. The result was cross-checked with the DQF-COSY spectrum and were found to be in excellent agreement where the two spin systems were maintained. According to the distances given in the crystal structure and the correlated T_1 assignments, the *ortho* proton did not show coupling in the COSY spectrum, as supported by the prior discussion, and complete assignment is shown in Figure 4-4 and Table 4-3. Additionally, it can be seen from the X-ray crystallography data that the amine proton is directly in the xy-plane of the metal center suggesting it experiences large dipolar relaxation contributions which is reflected in its small measured T_1 value of 1.68 ms while the others are distorted with pyridyl plane.

Table 4-3. ^{1}H NMR Chemical Shifts for Fe(bapbpy)(OTf)$_2$ in CD_3CN at 298 K.

assignment	chem shift (ppm)[a]	$\Delta\nu_{1/2}$ (Hz)[b]	T_{1exp} (ms)[c]	Fe-H (Å)[d]	rel area
α	64.54	103	5.98	4.956	2, s
α'	61.08	88	7.21	4.993	2, s
β	8.28	25	16.16	5.796	2, s
β'	10.61	33	21.94	5.835	2, s
γ	29.64	49	8.16	5.139	2, s
γ'	42.23	57	11.06	5.155	2, s
λ	7.05	128	1.68	4.150	2, s
λ'	75.78	920	0.2	2.954	2, br s

[a] Chemical shifts are listed in ppm relative to the residual solvent peak of C*H*D$_2$CN (^{1}H, 1.94 ppm, pentet). [b] Line widths are full width at half the maximum peak height. [c] T_1 values were obtained at 500 MHz. [d] Iron-proton distance measurements obtained from the X-ray crystallographic structural data.

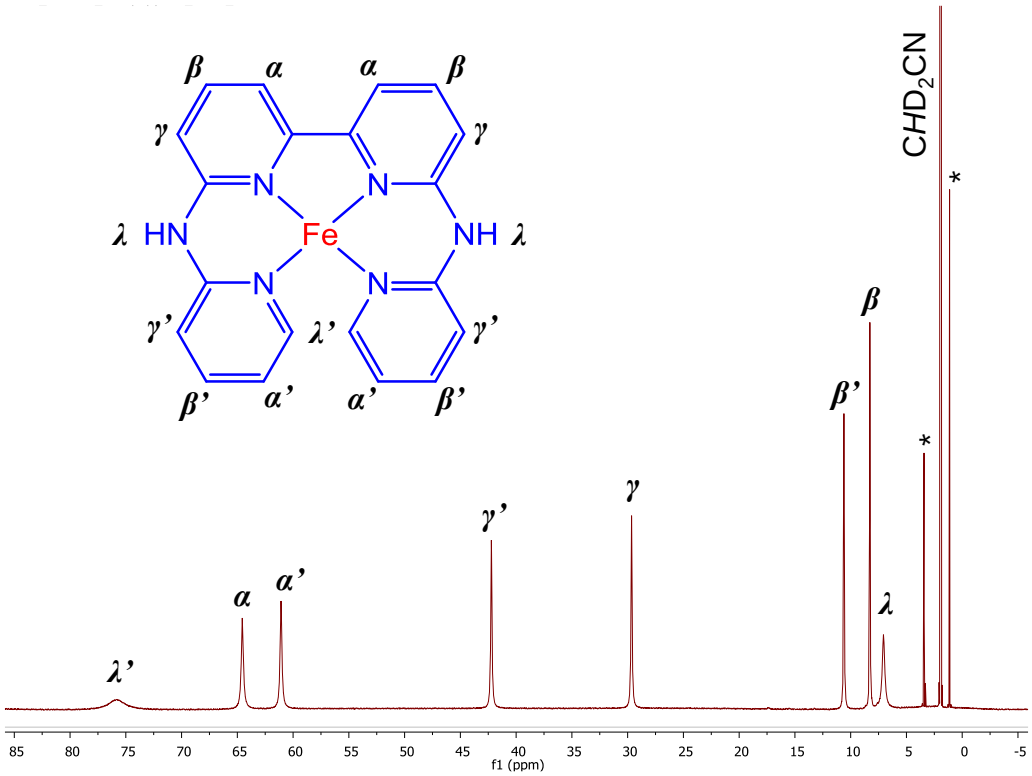

Figure 4-4. ^{1}H NMR of Fe(bapbpy)(OTf)$_2$ in CD_3CN at 298 K. Spectrum was referenced to the residual proton C*H*D$_2$CN peak (1.94 ppm, pentet). * Absorbed THF in the CD_3CN solvent from argon glovebox atmosphere.

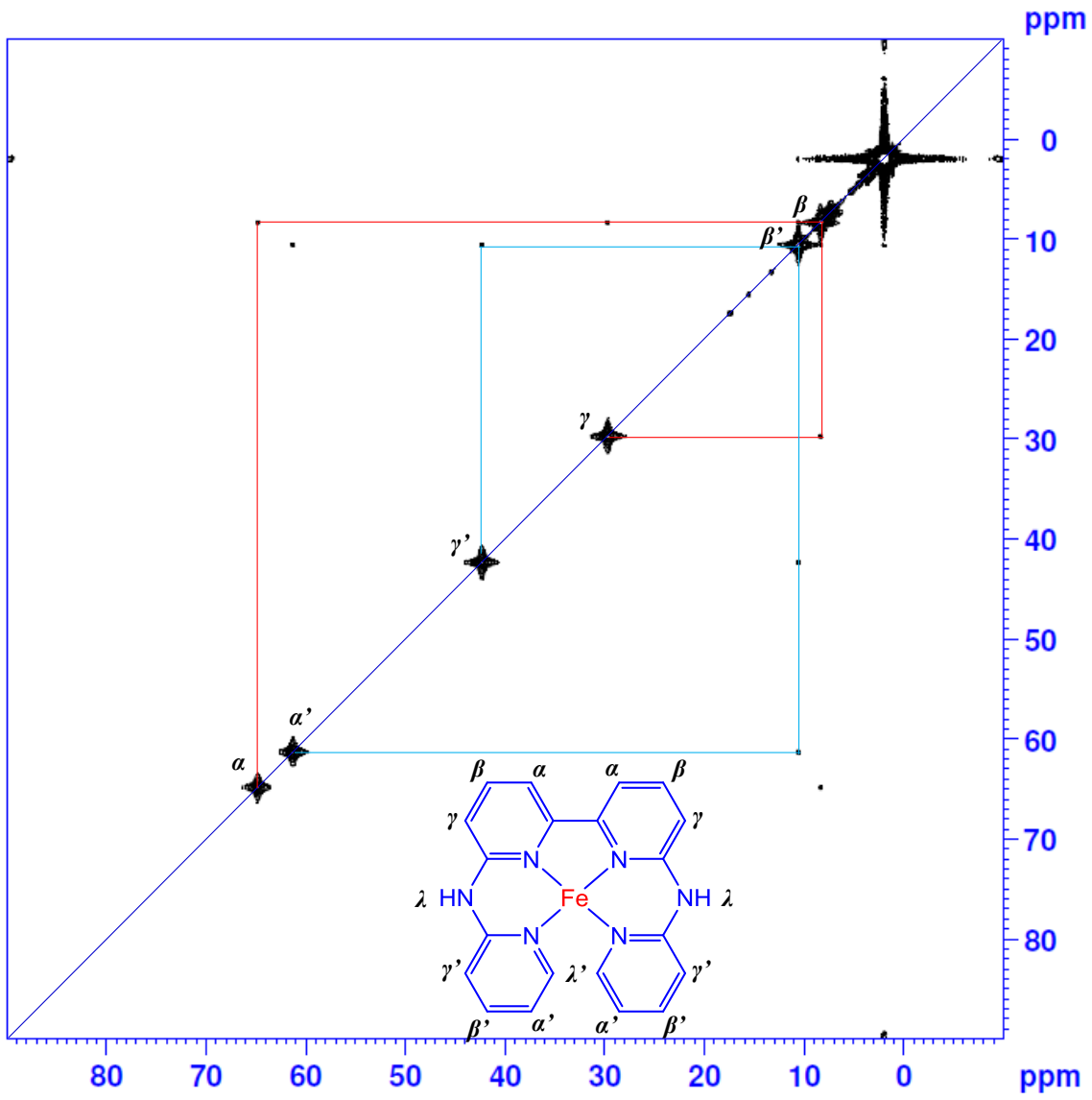

Figure 4-5. 2D ^{1}H DQF-COSY of Fe(bapbpy)(OTf)$_2$ in CD_3CN at 298 K showing two spin systems.

Magnetic Properties. The magnetic properties of Fe(bapbpy)(OTf)$_2$ were examined by measurement of its magnetic susceptibility. In acetonitrile-d_6, Fe(bapbpy)(OTf)$_2$ exhibited an effective magnetic moment of μ_{eff} = 4.9(7) μ_B as measured by Evans method.[22] The solvated complex is coordinated in the axial positions by the

triflate anions or, more likely, coordinated by the solvent giving a pseudo octahedral high-spin geometry. A quintet ground state is possible with four unpaired electrons on the iron center. The observed magnetic moment is slightly higher than the predicted spin-only magnetic moment for four unpaired electrons of this electronic structure (μ_{SO} = 4.90 μ_B) indicating only minor orbital contributions. Mössbauer spectroscopy of the solid-state complex can be fitted by a single doublet, confirming only Fe(II) valence (Figure 4-6).

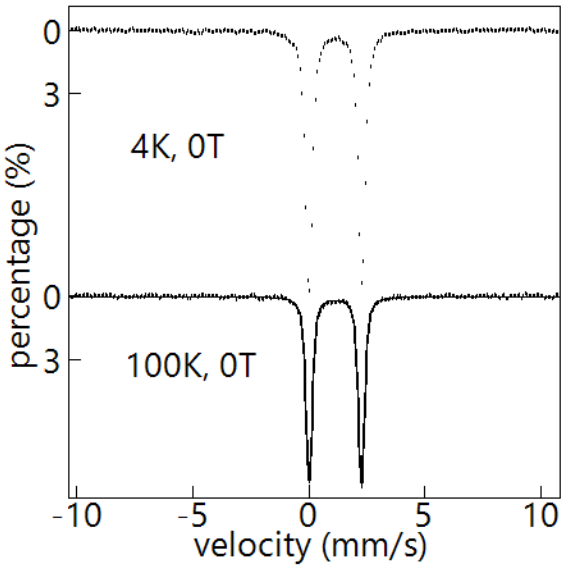

Figure 4-6. Mössbauer spectroscopy of Fe(bapbpy)$(OTf)_2$ at 4 and 100 K with zero applied magnetic field. Parameters: isomer shift of δ = 1.14 mm/s; quadrupole fitting of ΔE_q = 2.26 mm/s; and linewidth = -0.24 mm/s. Fit with a single doublet indicating only ferrous species present.

Triflate Coordination and Properties. It was observed that the Fe(bapbpy)$(OTf)_2$ complex was stable under normal atmosphere when completely dry, but slowly decomposed when the crystals were dissolved in MeCN and exposed to air. The solvated

air sensitivity can be attributed to coordination of the triflate anion in the crystal state while in the solution phase triflate is a free anion, opening up new active sites on the metal center allowing oxygen to coordinate. To probe the coordination of the triflate anion in the solid and solution phase, vibrational shifts of the SO_3 group were examined using ATR-FTIR (Figure 4-8 and Table 4-4; the full IR spectrum of the complex is given in Figure 4-7). Vibrational assignments of metal-coordinated triflate anions were given in previous studies.[26-28] In the solution phase, the aromatic C-C vibrations do not shift and have good correspondence to the solid phase. However, a very different profile is seen in the triflate region of 1400 cm^{-1} to 1000 cm^{-1} offering strong evidence that the triflate anion has dissociated from the metal center when solvated. This is good support for the high catalytic activities observed in CO_2 reduction and H_2 evolution reactions.

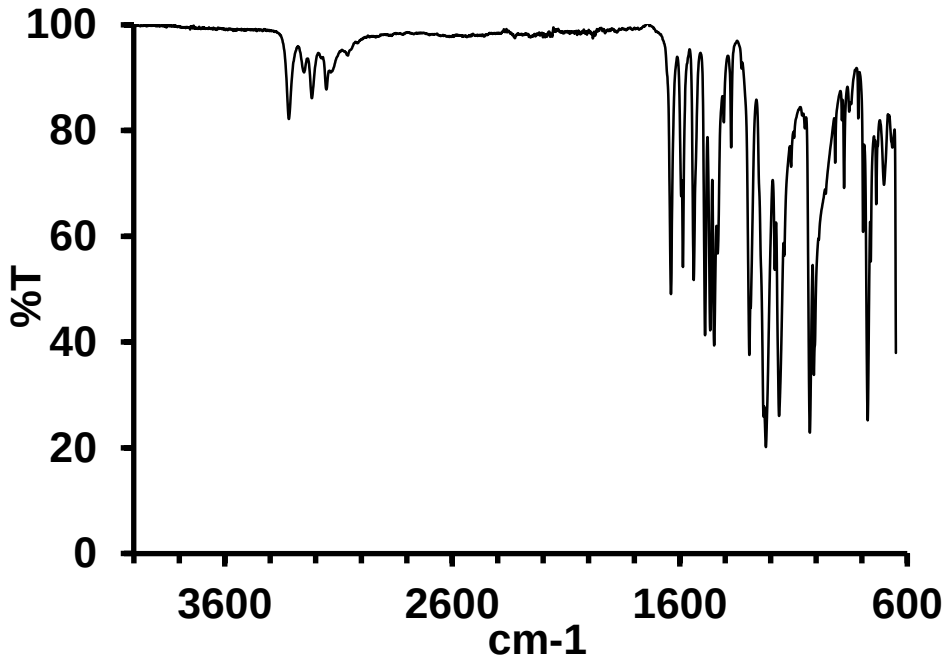

Figure 4-7. FT-IR spectrum of $Fe(bapbpy)(OTf)_2$ crystals using ATR attachment.

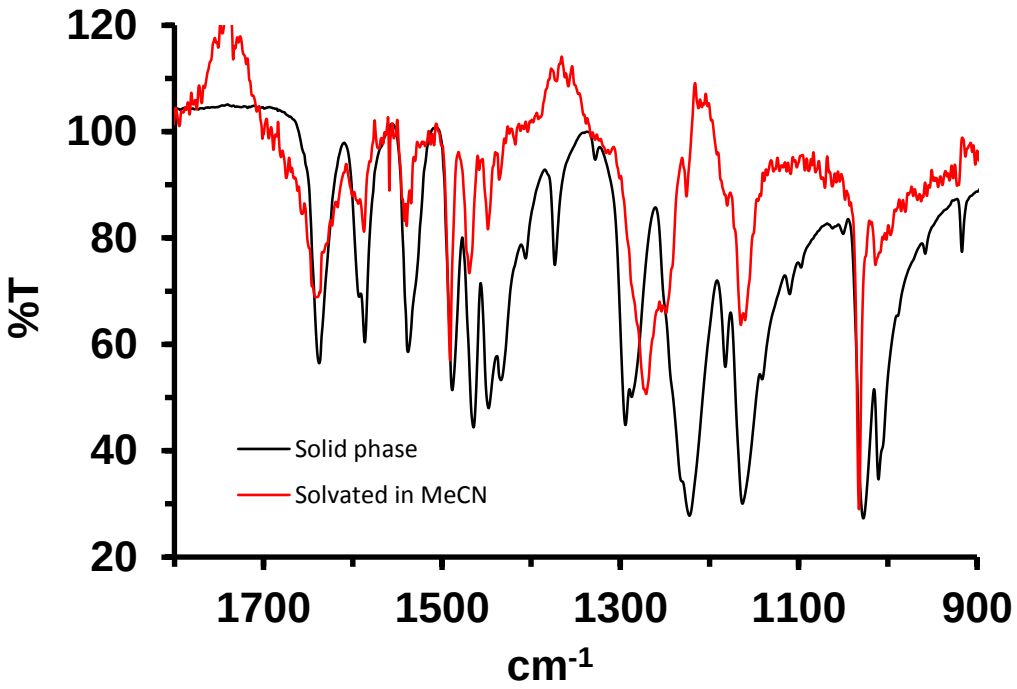

Figure 4-8. ATR-FTIR of Fe(bapbpy)$(OTf)_2$ crystals (black) and solvated complex in MeCN (red). Assignments are given in the Experimental section.

Table 4-4. Vibrational Shifts of IR Spectra in Figure 4-7.

Solid State		Solvated in MeCN	
ν **(cm^{-1})**	**Vibration**	***ν*** **(cm^{-1})**	**Vibration**
1639	C=C	1641	C=C
1586	C=C	1588	C=C
1538	C=C	1539	C=C
1489	C=C	1491	C=C
1466	C=C	1469	C=C
1449	C=C	1449	C=C
1374	SO_2	-	-
1294	SO_2	1272	SO_2
1222	CF_3	1248	CF_3
1164	CF_3	1165	CF_3
1029	SO_2	1033	SO2
1011	CF_3	-	-

Electrochemical Characterization. Cyclic voltammetry (CV) studies of Fe(bapbpy)$(OTf)_2$ show a reversible $Fe^{2+/3+}$ redox couple at 0.697 V vs Fc and six irreversible peaks from -1.66 V to -2.70 V vs Fc in MeCN, as seen in Figure 4-9. On the return wave, there is some slight quasi-reversibility shown in the peak at 0.62 V vs Fc. In N,N'-dimethylformamide (DMF), the first reduction peak becomes more reversible (Figure 4-10) indicating that MeCN interferes with the reversibility of Fe(bapbpy)$(OTf)_2$. Increasing the potential more negative shows several more reductions that can be attributed to the bipyridines on the bapbpy ligand through possible non-innocent redox activity.

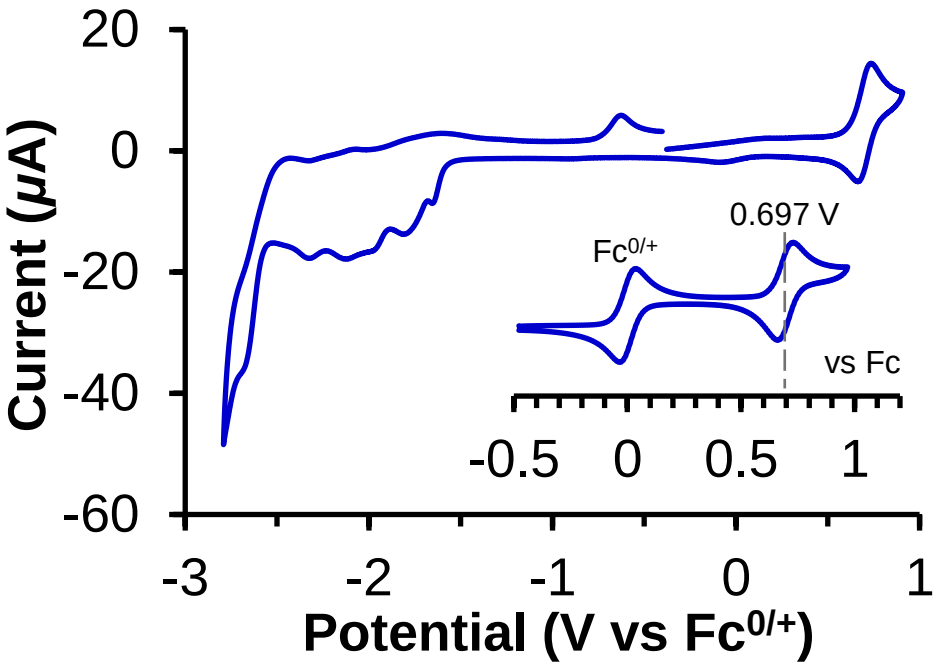

Figure 4-9. Cyclic voltammograms of 0.5 mM Fe(bapbpy)$(OTf)_2$ in MeCN under N_2 with 0.1 M $TBAPF_6$ supporting electrolyte, an Ag/AgCl reference electrode, a polished glassy-carbon working electrode, and a glassy-carbon counter electrode under N_2. T = 20 °C ± 2. Ferrocene added afterward for internal referencing.

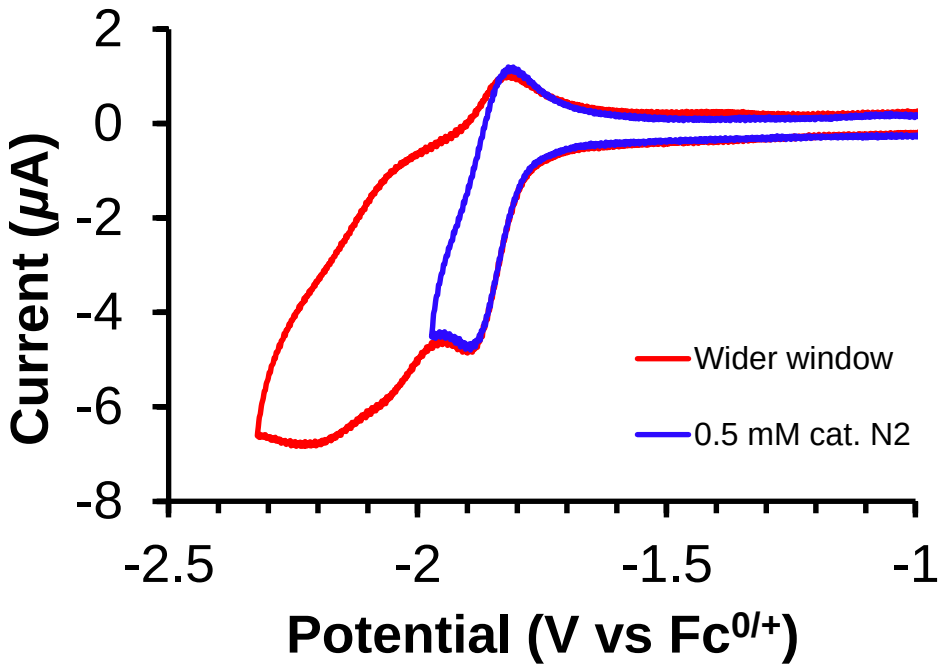

Figure 4-10. Cyclic voltammograms of 0.5 mM Fe(bapbpy)$(OTf)_2$ in DMF under N_2 with 0.1 M $TBAPF_6$ supporting electrolyte, an Ag/AgCl reference electrode, a polished glassy-carbon working electrode, and a glassy-carbon counter electrode with a scan rate of 50 mV/s. T = 20 °C ± 2. Ferrocene added afterward for internal referencing.

Electrocatalytic Reduction of CO_2. The reduction of CO_2 was achieved by bubbling a 0.5 mM solution of Fe(bapbpy)$(OTf)_2$ in an air-tight container with CO_2 gas and applying an electrochemical potential. CV was used to observe the catalytic response and calculate the TOF and overpotential. Constant potential electrolysis was used to calculated the TON. Figure 4-11 shows the catalytic response occurs at -2.19 V vs Fc at the addition of CO_2 after a background scan under a nitrogen atmosphere. To increase the catalytic CO_2 reduction performance the proton donor was optimized. First, the reaction was optimized using water as a proton donor. Figure 4-12 shows a complex catalytic profile

where the potential of the catalytic peaks shifts to less negative potential along with the development of new peaks. Figure 4-12A shows a linear increase in less negative potential with the increase of water concentration from 0% to 0.1% (v/v) and nearly constant current. The same linear trend is observed of decreasing overpotential with the addition of more water up to 1% giving a slight increase of catalytic current (Figure 4-12B). Further increasing the concentration of water from 1% to 5% shows dramatic changes.

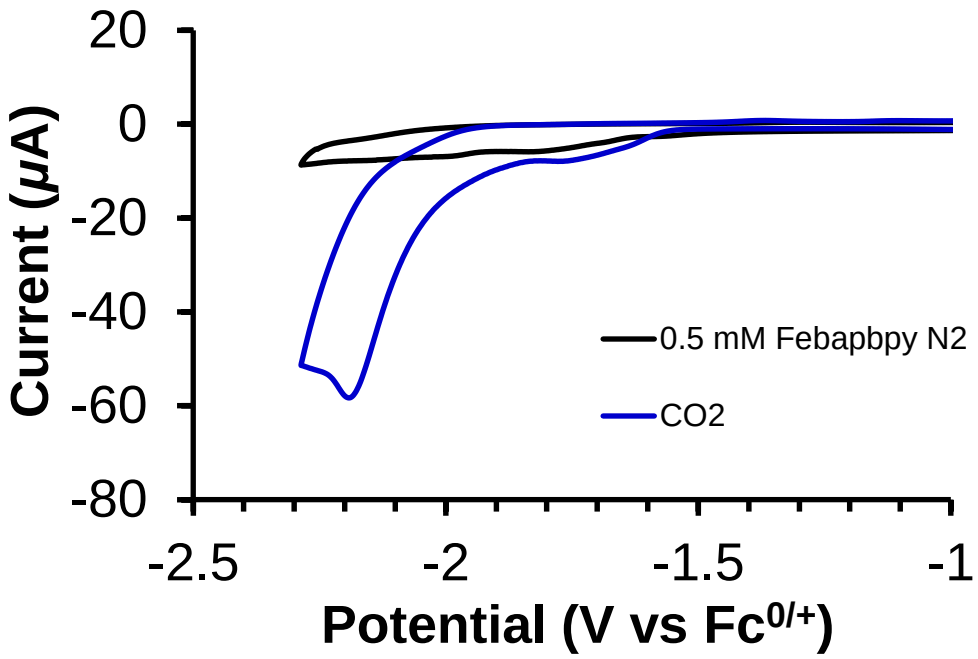

Figure 4-11. Cyclic voltammograms of 0.5 mM Fe(bapbpy)$(OTf)_2$ in MeCN under N_2 and CO_2 with 0.1 M $TBAPF_6$ supporting electrolyte, an Ag/AgCl reference electrode, a polished glassy-carbon working electrode, and a glassy-carbon counter electrode with a scan rate of 100 mV/s. T = 20 °C ± 2. Ferrocene added afterward for internal referencing. Ohmic drop was not considered due to the small currents involved.[35-36]

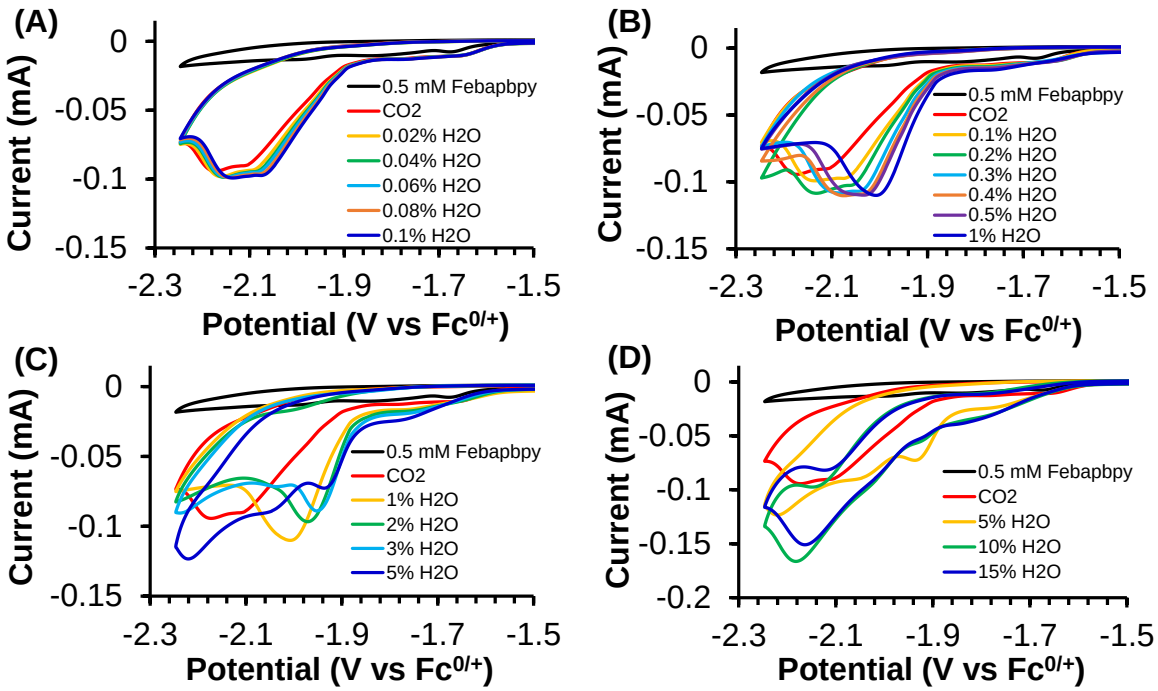

Figure 4-12. Cyclic voltammograms of H_2O dependence on the electrocatalytic reduction of CO_2 with 0.5 mM Fe(bapbpy)$(OTf)_2$ in MeCN with 0.1 M $TBAPF_6$ supporting electrolyte, an Ag/AgCl reference electrode, a polished glassy-carbon working electrode, and a glassy-carbon counter electrode with a scan rate of 100 mV/s. T = 20 °C ± 2. Ferrocene added afterward for internal referencing.

As observed in Figure 4-12C, the catalytic current decreases along with the overpotential to a lower potential of -1.95 V vs Fc between 2% and 3% water. However, the development of several new peaks begins to form at -2.04 V vs Fc and -2.22 V vs Fc with 3% or more water with a sharp increase of catalytic current for the new peaks. Figure 4-12D reveals the less negative potential peaks nearly disappear completely with one pronounced peak at -2.16 V vs Fc. Each peak in the CV is an indication of a different catalytic mechanisms occurring at the various potentials. The formation of new peaks are

likely due to the competing hydrogen evolution reaction (HER) from water with which increasing the water concentration past 3% increases the Faradaic efficiency (F.E.) of hydrogen evolution beyond the F.E. of the CO_2 reduction reaction. The decrease in overpotential indicates changes in the catalytic mechanism for CO_2 reduction and is dependent on the pH and/or the concentration of the proton donor. Constant potential experiments were performed to determine the products with water as a proton donor using GC analysis and confirmed the formation of H_2 and CO. With 0.1% water, the F.E. for CO and H_2 was 5% and 20%, respectively, suggesting significant energy loss to other unknown products. Hence, the solution phase was investigated via ^{1}H NMR and revealed 0.5% formic acid was produced. However, this does not account for all of the energy loss.

In attempts to further optimize the CO_2 reduction reaction, methanol was used as a different proton source as it has a higher pKa (pka^{MeCN} *ca.* 39) that will likely decrease the competing HER reaction.[37-39] As seen in Figure 4-13, the most prominent catalytic peak occurs at -2.26 V vs Fc at 10% MeOH, however, there is a relatively large peak at lower potential at -1.58 V vs Fc that is not present with H_2O as a proton source (Figure 4-12D). Between 5% and 10% MeOH the large peak at -2.26 V vs Fc shifts more negative to -2.38 V vs Fc indicating increased HER competition implying that 5% is more optimal for increased selectivity than 10% MeOH concentration. Constant potential experiments were done to analyze the products. At 5% MeOH, F.E.'s of 71% and 20% for CO and H_2, respectively, giving a much higher selectivity than that of water as a proton donor. Increasing the MeOH concentration to 10% gives a nearly reverse of F.E.'s than the prior with 20% and 79% for CO and H_2, respectively. While coulombic efficiencies are 91% and 99% for 5% and 10% MeOH above, respectively, there is still some degree of energy loss.

^{1}H NMR taken of the resulting mixture of a constant potential experiment with 0.1% methanol showed the presence of formic acid at *ca.* 5% F.E. and a smaller amount of formaldehyde, indicating multi-proton and multi-electron processes are catalyzed by this iron complex. GC analysis shows that methanol still produces a significant amount of H_2 evolution.

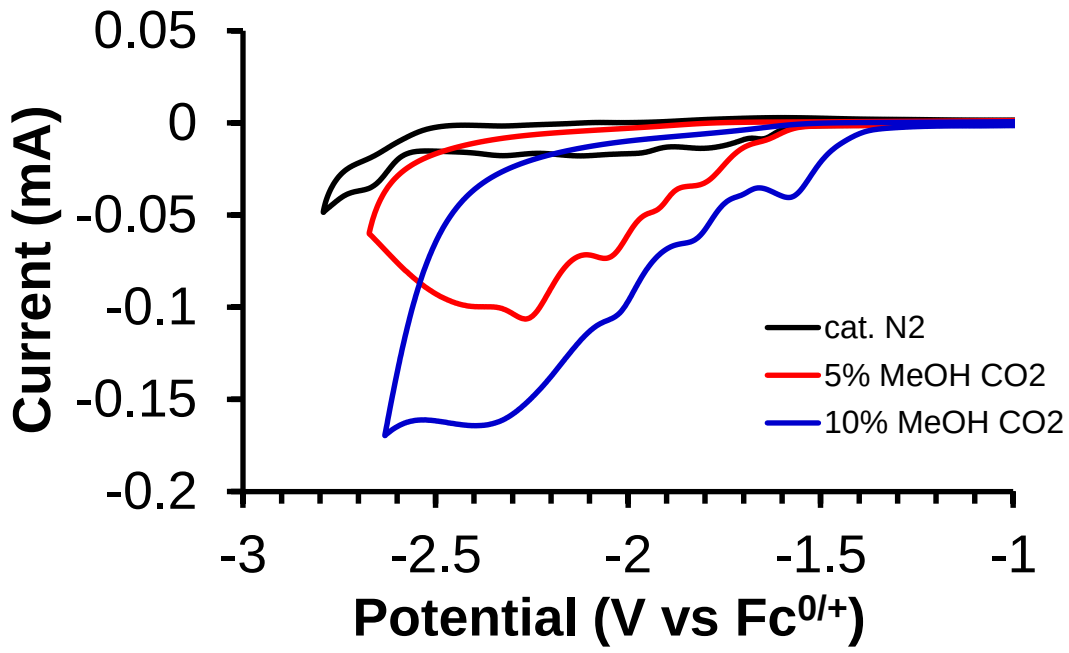

Figure 4-13. Cyclic voltammograms of MeOH dependence on the electrocatalytic reduction of CO_2 with 0.5 mM Fe(bapbpy)$(OTf)_2$ in MeCN with 0.1 M $TBAPF_6$ supporting electrolyte using Ag/AgCl reference electrode, a polished glassy-carbon working electrode, and a glassy-carbon counter electrode with a scan rate of 100 mV/s. T = 20 °C ± 2. Ferrocene added afterward for internal referencing.

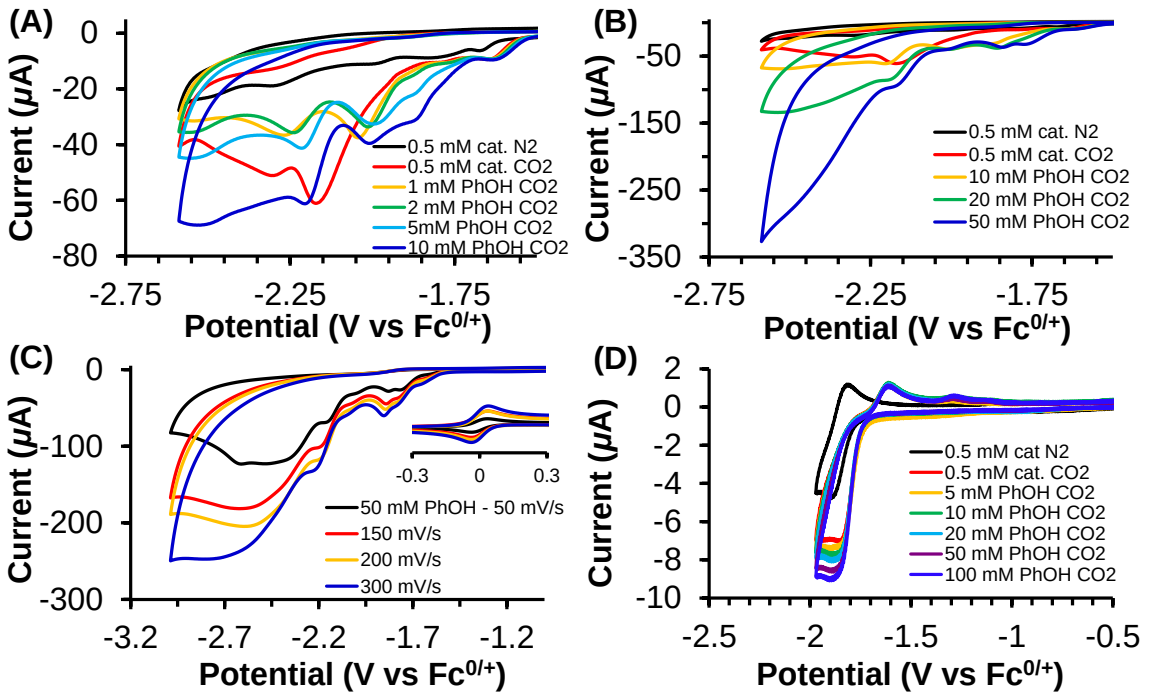

Figure 4-14. Cyclic voltammograms of PhOH dependence on the electrocatalytic reduction of CO_2 in MeCN and DMF with 0.5 mM Fe(bapbpy)$(OTf)_2$ with 0.1 M $TBAPF_6$ supporting electrolyte, an Ag/AgCl reference electrode, a polished glassy-carbon working electrode, and a glassy-carbon counter electrode. T = 20 °C ± 2. Ferrocene added afterward for internal referencing. (A) Increasing phenol (PhOH) concentration from 0 to 10 mM in MeCN with a scan rate of 100 mV/s. (B) Increasing phenol concentration from 10 mM to 50 mM in MeCN with a scan rate of 100 mV/s. (C) Increasing scan rate from 50 mV/s to 300 mV/s at 50 mM phenol. Inset: $Fc^{0/+}$ redox couple at an equivalent current response as the catalyst $Fe^{2+/3+}$ redox couple. (D) Increasing phenol concentration from 0 mM to 100 mM in DMF with a scan rate of 50 mV/s.

Phenol was then evaluated as a proton source as it has been shown to be an effective proton donor while yielding high selectivity due to its high pKa.[38] In MeCN, phenol has a

pKa of 29.14 which was used to determine the overpotential (η).[23] The effect of adding phenol to the catalytic solution is shown in Figure 4-14. In Figure 4-14A, the CO_2 reduction peak without the addition of phenol shows three catalytic peaks, a moderate one at -2.30 V vs Fc, the prominent peak at -2.19 V vs Fc and a small one at -1.62 V vs Fc. With the addition of 1 mM phenol, the two larger peaks shift less negative as seen with water and methanol to -2.26 V vs Fc and -2.03 V vs Fc with a decrease in catalytic current. Closer inspection reveals a total of five catalytic peaks in total at -2.54 V vs Fc, -2.27 V vs Fc, -2.03 V vs Fc, -1.89 V vs Fc, and -1.64 V vs Fc. Similar to the addition of water or methanol, this shift in potential is indicative of a change in the reaction mechanism. Increasing the concentration of phenol from 1 to 5 mM decreases the current and potential at the prominent peak to -2.00 V vs Fc while slightly increasing the current for the peak at -1.89 V vs Fc. The decrease of current for some peaks and increase of current at -1.89 V vs Fc suggests differing selectivity at differing concentrations of phenol. From 5 to 10 mM a large increase of catalytic current is observed at -2.51 V vs Fc and is attributed to HER competition based on the CV and GC analysis done with water and methanol studies prior, and the CO_2/CO reduction peak at -2.20 V vs Fc is attributed to the CO_2/CO reduction reaction. Figure 4-14B shows the hydrogen evolution peak at -2.51 V vs Fc and the CO_2 reduction peak at -2.20 V vs Fc continue to increase in catalytic current until 50 mM phenol. For this reason, constant potential experiments were performed with 20 mM phenol concentration as the HER peak was relatively small while still giving increased catalytic current for CO_2 reduction.

To obtain the TOF of the catalyst, a plateau S-shaped curve needs to be achieved either by increasing the substrate concentration or the scan rate.[40] Figure 4-14C shows

scan-rate dependence at 50 mM phenol and a wider potential window to capture the hydrogen evolution peak that is occurring just before reduction of the solvent. A nice plateau is reached at 300 mV/s giving a peak potential of 133 μA at -2.23 V vs Fc for the reduction of CO_2. As the reversibility of the $Fe^{+/2+}$ and $Fe^{0/+}$ redox couples are non-ideal, the current ratio i_{cat}/i_p was calculated using the $Fc^{0/+}$ redox couple at an equivalent current response as the iron catalyst $Fe^{2+/3+}$ redox couple to be used for TOF calculations with negligible error.[41] Therefore, i_{cat}/i_p is 9.33 and the TOF for CO production is calculated to be 51 s^{-1}, however, these values are only estimates as they are mixed products (CO/H_2). Overpotential (η) was calculated using the peak catalytic potential as described previously in Eq 4-1 yielding a relatively low overpotential of 380 mV.[41-42] In DMF (Figure 4-14D), the reduction of CO_2 yielded a more reversible process showing slower catalytic activity, however, smaller overpotential. At these conditions, i_{cat}/i_p was 3.31 giving a TOF of 1.07 s^{-1} and an overpotential of 260 mV. Furthermore, it is interesting to note that the catalytic peak potential does not shift more negative with increasing phenol concentration as it did in acetonitrile indicating the solvent plays a catalytic role at some level.

Preliminary studies of GC analysis on bulk electrolysis experiments at a constant potential of -1.72 V vs Ag/AgCl (the peak of -2.20 V vs Fc in CV experiments) with 20 mM phenol in acetonitrile indicated the presence of CH_4, CO, and H_2 gases. These were not quantified; however, the peaks were referenced to calibrated samples containing the solvent matrix, purged with CO_2 and injected with the specified gas of either CH_4, CO, and H_2. These results confirm $Fe(bapbpy)(OTf)_2$ is able to catalyze eight-electron and eight-proton electrochemical processes to the formation of high-value methane. Furthermore, the observed methane formation offers explanation for the variation of the multiple peaks as

seen in Figure 4-14 due to the multiple electron reduction steps in the mechanism. That is, the shifting catalytic peak potentials as well as increase and decrease of the various CV peaks with respect to phenol concentration suggests selectivity of intermediates between two- and eight-electron reductions can be controlled by phenol concentration dependence and applied potential. It is believed that these complex reductions are facilitated by non-innocence redox activity with the ligand.

Beyond electrochemical conversions of carbon dioxide to methane, light-driven photochemical conversion of CO_2 to methane was attempted. In preliminary studies, a sample was irradiated with visible light for 72 h containing 0.5 mM Fe(bapbpy)$(OTf)_2$, 20 mM phenol as a proton donor, 0.5 mM $Ir(ppy)_3$ as a photosensitizer, and 50 mM TEA as a sacrificial electron donor in dry MeCN. GC analysis revealed a significant methane peak, very weak carbon monoxide peak, and a strong hydrogen peak indicating methane selectivity over CO with a competing hydrogen evolution side-reaction (Figure 4-15). Such results suggest further optimization of the Fe(bapbpy)$(OTf)_2$ catalyst conditions may lead to selective reduction of CO_2 to methane formation electrochemically or photochemically. The extensive stabilization of the CO_2 adduct intermediate to enable the multi-electron and multi-proton reductions to form methane can be visualized as Figure 4-16.

Note: The preliminary data associated with the methane formation were produced from an experiment performed only once due to time constraints. This experiment should be repeated to confirm the reproducibility of the results.

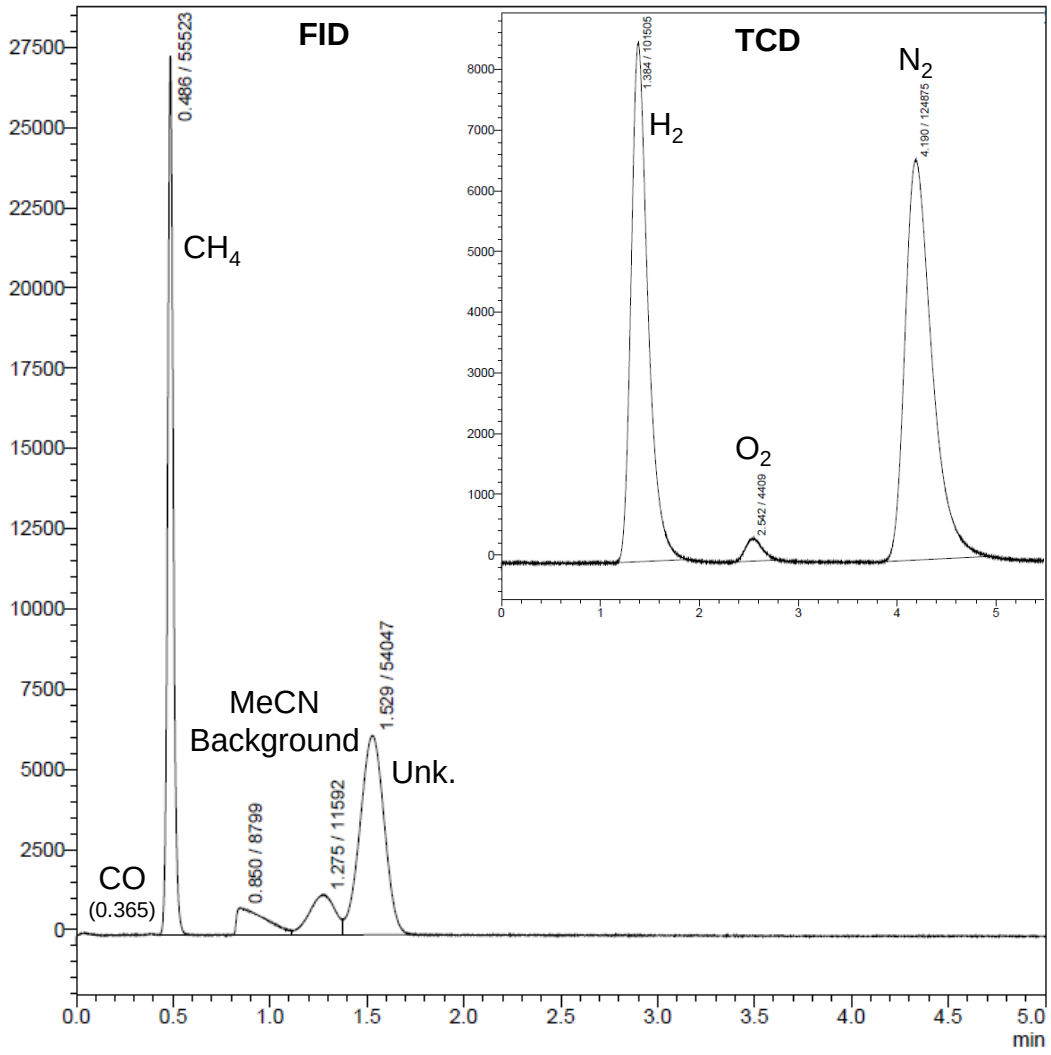

Figure 4-15. GC analysis of the photochemical reduction of CO_2. Peak assignment was determined from standardized samples. Retention times and integration areas are listed with only the standard retention time for CO is shown in parentheses.

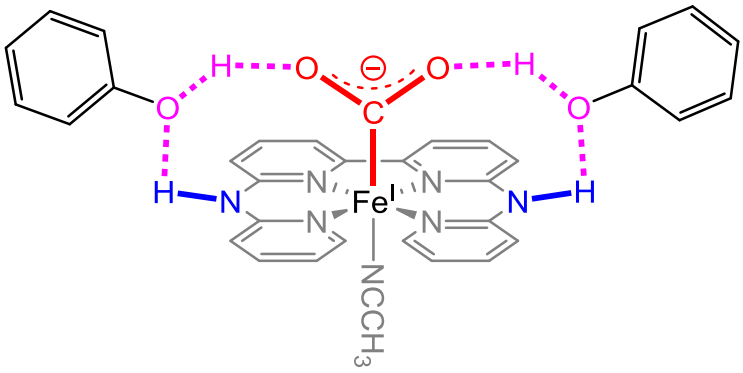

Figure 4-16. Hydrogen bonding stabilization of the CO_2 adduct on Fe(bapbpy)$(OTf)_2$ through the proton relay system assisted by the proton donor.

Electrocatalytic Hydrogen Evolution. Fe(bapbpy)$(OTf)_2$ can catalyze the reduction of acids to produce H_2. The first acid studied as a proton source was anilinium tetrafluoroborate which exhibited a catalytic response as seen in Figure 4-17A. Increasing the concentration of acid to 290 mM gave a nice S-shape plateau indicative of substrate saturation.[41] The TOF was calculated using the $Fe^{2+/3+}$ redox couple as before to give an i_{cat}/i_p of 357 and a corresponding TOF of 25,000 s^{-1}. Using the pKa of 10.7 for anilinium in acetonitrile[43] and an $E_{1/2}$ of -1.67 V vs Fc, the overpotential was calculated to be 900 mV. However, Figure 4-17A shows the catalytic potential becomes increasingly negative with the increase of relatively large current indicates the source of such a large overpotential is likely due to ohmic drop (iR), which can be corrected for electronically giving a decrease in measured catalytic overpotential.[35-36, 44] Figure 4-17B shows the catalytic response to the reduction of acetic acid to form H_2 with an i_{cat}/i_p of 777. Using the pKa of 22.3 for acetic acid in acetonitrile and an $E_{1/2}$ of -1.97 V vs Fc, the overpotential was calculated to be 510 mV with a substantial TOF of 120,000 s^{-1}.

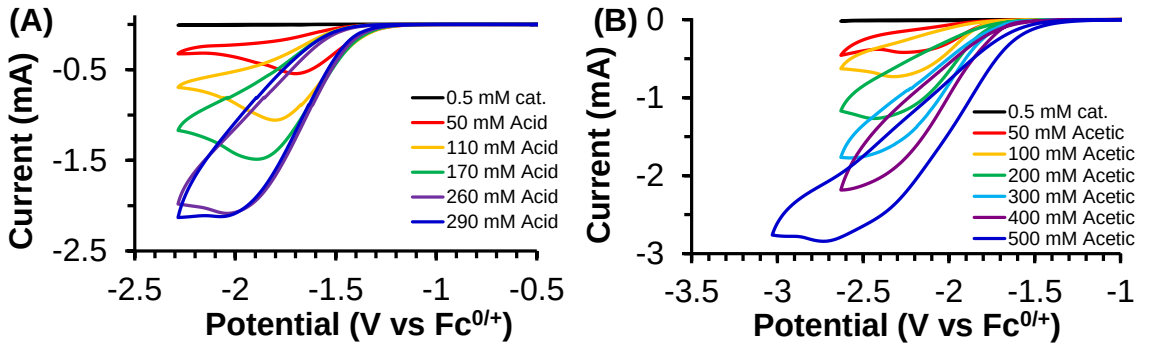

Figure 4-17. Cyclic voltammograms of acetic acid dependence on the hydrogen evolution reaction with 0.5 mM Fe(bapbpy)$(OTf)_2$ 0.1 M $TBAPF_6$ supporting electrolyte in MeCN, an Ag/AgCl reference electrode, a polished glassy-carbon working electrode, and a glassy-carbon counter electrode with a scan rate of 100 mV/s. T = 20 °C ± 2. Ferrocene added for internal referencing. (A) Increasing anilinium tetrafluoroborate concentration from 0 to 290 mM. (B) Increasing glacial acetic acid concentration from 0 mM to 500 mM.

Conclusions

While metal-bound bapbpy complexes have been utilized in spin-crossover studies,[14, 45] the Fe(bapbpy)$(OTf)_2$ complex has never been synthesized or used for the electrocatalytic reduction of CO_2. The choice of the triflate precursor was in part due to its weakly coordinating attributes that will allow available active sites in solution to enable the reduction for CO_2 as well as for its electrochemical stability. The characterization of Fe(bapbpy)$(OTf)_2$ provides a rare example for which both the solid-state structure is known and the paramagnetic ^{1}H NMR resonances are fully assigned. Additionally, a 2D ^{1}H DQF-COSY spectrum was obtained with sufficient proton coupling to support resonance and T_1 assignments. Electronic studies reveal four unpaired electrons in the paramagnetic complex consistent with its distorted pseudo-octahedral geometry.

The electrochemical reduction of CO_2 with various proton donors revealed that phenol gave the best selectivity over hydrogen production as well as access to higher-value products such as methane with a TOF of 51 h^{-1} and an overpotential of 380 mV in acetonitrile. Electrolysis in DMF yielded a much smaller TOF of 3880 h^{-1} but also a smaller overpotential of 260 mV, although slightly reversible. Products in DMF were not confirmed by GC. The photochemical reduction of CO_2 using $Ir(ppy)_3$ as a photosensitizer yielded high selectivity over methane, however, still accompanied by a significant amount of hydrogen evolution. Future studies aim to further optimize the reduction of CO_2 for methane selectivity for both electrocatalytic and photocatalytic reactions. Catalyzing the hydrogen evolution reaction gave a generous TOF of 120,000 s^{-1} at a relatively large overpotential of 510 mV at 500 mM acetic acid in acetonitrile.

The generation of multi-electron reduced products such as CO and methane are attributed to the two pendent amines which allow for increased stabilization of the metal-CO_2 adducts. While still in the early stages of optimization for the iron(II)-polypyridine catalyst, the research presented here has realized the electrochemical conversion of CO_2 to methane enabled by the amine proton relay and pyridine system. We anticipate this study will inspire the development of more efficient homogeneous molecular catalysts for the electrochemical and photochemical reduction of CO_2 to bolster sustainable energy sources.

References

1. Petroleum Resources Management System **2007** (Society of Petroleum Engineers (SPE), A. A. o. P. G. A., World Petroleum Council (WPC), Society of Petroleum Evaluation Engineers (SPEE)).
2. Reserven, R. u. V. v. E. D. R., Bundesanstalt fgr Geowissenschaften und Rohstoffe).
3. Chen, L.; Guo, Z.; Wei, X.-G.; Gallenkamp, C.; Bonin, J.; Anxolabehere-Mallart, E.; Lau, K.-C.; Lau, T.-C.; Robert, M. *J. Am. Chem. Soc.* **2015**, *2015*, 10918-10921.
4. Lacy, D. C.; McCrory, C. C. L.; Peters, J. C. *Inorg. Chem.* **2014**, *53*, 4980-4988.
5. Roy, S.; Sharma, B.; Pecaut, J.; Simon, P.; Fontecave, M.; Tran, P. D.; Derat, E.; Artero, V. *J. Am. Chem. Soc.* **2017**, *139*, 3685-3696.
6. Fujita, E.; Haff, J.; Sanzenbacher, R.; Elias, H. *Inorg. Chem.* **1994**, *33*, 4627-4628.
7. Collin, J. P.; Jouaiti, A.; Sauvage, J. P. *Inorg. Chem.* **1988**, *27*, 1986-1990.
8. Chabolla, S. A.; Machan, C. W.; Yin, J.; Dellamary, E. A.; Sahu, S.; Gianneschi, N. C.; Gilson, M. K.; Tezcana, F. A.; Kubiak, C. P. *Faraday Discuss.* **2017**, *198*, 279-300.
9. Beley, M. C., J. P.; Ruppert, R.; Sauvage, J. P. *J. Am. Chem. Soc.* **1986**, *108*, 7461-7467.
10. Rao, H.; Schmidt, L. C.; Bonin, J.; Robert, M. *Nature* **2017**, *548*, 74-77.
11. Steinlechner, C.; Junge, H. *Angew. Chem. Int. Ed.* **2018**, *57*, 44-45.
12. Francke, R.; Schille, B.; Roemelt, M. *Chem. Rev.* **2018**, *118*, 4631-4701.
13. Arcis-Castíllo, Z.; Zheng, S.; Siegler, M. A.; Roubeau, O.; Bedoui, S.; Bonnet, S. *Chem. Eur. J.* **2011**, *17*, 14826-14836.

14. Bonnet, S.; Siegler, M. A.; Costa, J. S.; Molnár, G.; Bousseksou, A.; Spek, A. L.; Gameza, P.; Reedijk, J. *Chem. Comm.* **2008**, *0*, 5619-5621.

15. Hagen, K. S. *Inorg. Chem.* **2000**, *39*, 5867-5869.

16. Sheldrick, G. M. *SADABS: Area Detector Absorption Correction* **2001**, University of Göttingen: Göttingen, Germany.

17. Dolomanov, O. V.; Bourhis, L. J.; Gildea, R. J.; Howard, J. A. K.; Puschmann, H. *J. Appl. Cryst.* **2009**, *42*, 339-341.

18. Sheldrick, G. M. *Acta Cryst. A* **2015**, *71*, 3-8.

19. Sheldrick, G. M. *Acta Cryst. C* **2015**, *71*, 3-8.

20. Bruker, A. B. A. I., Madison, Wisconsin, USA, **2007**.

21. Sheldrick, G. M. *Acta Cryst. A* **2008**, *64*, 112-122.

22. Evans, D. F. *J. Chem. Soc.* **1959**, *0*, 2003-2005.

23. Kutt, A.; Movchun, V.; Rodima, T.; Dansauer, T.; Rusanov, E. B.; Leito, I.; Kaljurand, I.; Koppel, J.; Pihl, V.; Koppel, I.; Ovsjannikov, G.; Toom, L.; Mishima, M.; Medebielle, M.; Lork, E.; Roschenthaler, G. V.; Koppel, I. A.; Kolomeitsev, A. A. *J. Org. Chem.* **2007**, *73*, 2607-2620.

24. Muckerman, J. T.; Skone, J. H.; Ninga, M.; Wasada-Tsutsui, Y. *Biochim. Biophys. Acta* **2013**, *1827*, 882-891.

25. Roya, K.; Popelier, P. L. A. *J. Phys. Org. Chem.* **2009**, *22*, 186-196.

26. Johnston, D. H.; Shriver, D. F. *Inorg. Chem.* **1993**, *32*, 2045-2047.

27. Lawrance, G. A. *Chem. Rev.* **1986**, *86*, 17-33.

28. Batchelor, R. J.; Ruddick, J. N. R.; Sams, J. R.; Aubke, F. *Inorg. Chem.* **1977**, *16*, 1414-1417.

29. Bertini, I.; Luchanat, C. *Benjamin/Cummings Publishing Company: Menlo Park, CA*, **1986**.

30. Berliner, L. J.; Reuben, J. *Springer Science Business Media, LLC: NY*, **1993**.

31. Bloembergen, N. *J. Chem. Phys.* **1957**, *27*, 572-573.

32. Swift, T. J.; Connick, R. E. *J. Chem. Phys.* **1962**, *37*, 307-320.

33. Bertini, I.; Luchinat, C.; Mancini, M.; Spina, G. *J. Magn. Reson.* **1984**, *59*, 213-222.

34. Solomon, I. *Phys. Rev.* **1955**, *99*, 559-566.

35. Howell, J. O.; Wightman, R. M. *Anal. Chem.* **1984**, *56*, 524-529.

36. Heinze, J. *Angew. Chem. Int. Ed.* **1993**, *32*, 1268-1288.

37. Morris, R. H. *Chem. Rev.* **2016**, *116*, 8588-8654.

38. Costentin, C.; Robert, M.; Savéant, J.-M.; Tatin, A. *PNAS* **2015**, *112*, 6882-6886.

39. Silverstein, T. P. H., S. T. *J. Chem. Educ.* **2017**, *94*, 690-695.

40. Costentin, C.; Drouet, S.; Robert, M.; Savéant, J.-M. *J. Am. Chem. Soc.* **2012**, *134*, 11235-11242.

41. Rountree, E. S.; McCarthy, B. D.; Eisenhart, T. T.; L., D. J. *Inorg. Chem.* **2014**, *53*, 9983-10002.

42. Sampson, M. D.; Kubiak, C. P. *J. Am. Chem. Soc.* **2016**, *138*, 1386-1393.

43. Felton, G. A. N.; Glass, R. S.; Lichtenberger, D. L.; Evans, D. H. *Inorg. Chem.* **2006**, *45*, 9181-9184.

44. Popkirov, G. S. *J. Electroanal. Chem.* **1993**, *359*, 97-103.

45. Zheng, S.; Siegler, M. A.; Roubeau, O.; Bonnet, S. *Inorg. Chem.* **2014**, *53*, 13162-13173.

CHAPTER V

CONCLUSIONS

To meet the pressing energy demands for clean, renewable energy sources, advanced energy storage and energy conversion systems are necessary. The work presented in this thesis details the advancement and strategies to remediate energy concerns by providing valuable insights to Mg electrolytes necessary for Mg battery operation, molecular engineering of viologen derivatives for efficient two-electron storage systems to be used for anolyte materials for aqueous organic redox flow batteries (AORFBs), and the synthesis and characterization of a polypyridine iron(II) compound to catalyze the reduction of CO_2 to energy-rich fuels and precursors.

In chapter 2, the Mg-Cl / Al-Cl in THF electrolyte system was investigated by higher level density function theory to gain a deeper understanding of the solution chemistry present to inspire the design of the next generation Mg electrolytes. Each theorized Mg and Al species were modeled to determine the most thermodynamically stable solvated species which was then used to examine the spontaneity of theorized Mg-Cl dimerization. The $[MgCl]^+$ species was found to solvate to the six-coordinate $[MgCl(THF)_5]^+$ species, contrary to previous results which concluded the $[MgCl(THF)_3]^+$ species was the most stable species in solution. However, by optimizing each structure directly in the modeled solvent using the universal solvation model, SMD, together with an ultrafine grid at the M06-2x / 6-31+G(d) level instead of simply optimizing in the gas-phase as previous studies have done, we were able to achieve excellent correlation to experimental measurements, hence, providing fundamental framework with which to

investigate the dimerization of Mg-Cl electrolytes in THF. To validate our method, we compared our calculated relative abundance of the self-ionization products of aluminum chloride in THF to the measured values yielding accuracy within 0.6 kcal/mol for this system. For the Mg-Cl systems, a comparison was made between the calculated bond lengths and measured bond-lengths from crystallographic data obtained from several known Mg-Cl structures. Not only were the bond-lengths in good agreement, but the orientation of the coordinated THF ligands matched as well, indicating the predictive power of the method implemented.

With the established method, solvation of Mg dichloride species was found to solvate to the five-coordinate *e,e-cis-tbp*-$MgCl_2(THF)_3$ (I) species. By examining the favorability of dimerization by *e,e-cis-tbp*-$MgCl_2(THF)_3$ (I) and $[MgCl(THF)_5]^+$, it was found that dimerization occurs favorably by a significant -6.30 kcal/mol suggesting that $[(\mu\text{-}Cl)_3Mg_2(THF)_6]^+$ is the most abundant species in THF solution.

The solvation of aluminum chloride in THF was also investigated as the only way to obtain Mg monochloride is through mono-Cl abstraction. To accurately model the mono-Cl abstraction of *e,e-cis-tbp*-$MgCl_2(THF)_3$ (I) by the Lewis acid, the most thermodynamically stable solvated aluminum chloride species were first determined. The $AlCl_3$ species was found to solvate to the known *trans*-$AlCl_3(THF)_2$ species, and the $[AlCl_2]^+$ species favorably coordinated with four THF molecules to give the [*trans*-$AlCl_2(THF)_4]^+$ species. The self-ionization of *trans*-$AlCl_3(THF)_2$ to the [*trans*-$AlCl_2(THF)_4][AlCl_4]$ ion pair was calculated to be uphill by 1.27 kcal/mol giving a relative abundance of *ca.* 25% self-ionization. Considering the contribution of each aluminum chloride species, the DFT results indicate mono-Cl abstraction of *e,e-cis-tbp*-$MgCl_2(THF)_3$

(I) is unfavorable by 4.22 kcal/mol. However, since the free energy of dimerization is so favorable (-6.30 kcal/mol), the overall dimerization reaction is driven by a thermodynamic force of -2.08 kcal/mol, hence, supporting Mg-Cl dimer formation in THF solution. Therefore, the results suggest that the dimer is the dominant species primarily involved in the Mg deposition process.

Chapter 3 presents rational molecular engineering of highly attractive two-electron storage viologen derivatives to be used as energy-dense anolyte materials for AORFBs. DFT was used as a powerful tool in designing the two-electron storage systems to explore the chemical and electronic properties of three different redox states of these two-electron storage molecules.

Electrostatic potential mapping provided insightful information concerning the compatibility of **(SPr)$_2$V** with a Nafion cation-exchange membrane due to charge distribution and size exclusion. Furthermore, the stability of these viologen derivatives is attributed to the high charge delocalization about the two ring systems in their frontier SOMO or HOMO.

Theoretical reduction potentials were calculated using MV as a relative reference molecule as a means to determine optimal viologen derivative candidates for synthesis. The choice and rationale of using this particular reference proved to yield exceptional experimental correlation to known viologen derivatives with a mean unsigned error of 37 mV for the first electron reduction and 36 mV for the second electron reduction demonstrating the lowest error reported to date for theoretical reduction potentials. These results reflect the importance of choosing a structurally and electronically similar reference

molecule when calculating theoretical reduction potentials via the cancelation of systematic errors method using a relative reference.

Further considerations of viologen derivatization were included to investigate pathways of energy loss that decrease the performance of RFBs. Hence, a thermodynamic analysis of their ability to initiate the hydrogen evolution side reaction was calculated in addition to the free energy of disproportionation, both of which can be used to further develop viologen derivatives. The synthetic and theoretical work presented has opened new avenues of viologen derivatization for building AORFBs with high voltage, high power density, and high energy density for economical and widespread use of RFBs in large-scale energy storage.

Chapter 4 details the synthesis and characterization of an iron(II) polypyridine catalyst, Fe(bapbpy)$(OTf)_2$, that enables the electrocatalytic and photocatalytic reduction of CO_2. Characterization of the catalyst provides a rare example for which both the solid-state structure is known and the paramagnetic ^{1}H NMR resonances are fully assigned yielding a beautiful ^{1}H NMR spectrum accompanied by a 2D ^{1}H DQF-COSY spectrum. The catalyst was further characterized by X-ray crystallography, FTIR, UV-vis, cyclic voltammetry, Mössbauer spectroscopy, and elemental analysis.

The electrochemical reduction of CO_2 demonstrated that optimization of the proton donor increased CO product selectivity substantially at 5% MeOH concentration with an overpotential of 380 mV in acetonitrile. According to CV analysis, changing the proton donor as well as its concentration tuned the selectivity of the catalyst. The presence of phenol as a proton source indicated possible electrochemical transformation of CO_2 to methane through GC analysis. Further confirmation of the methane product would

represent the first homogeneous molecular catalyst to electrochemically convert CO_2 to methane.

In addition to electrochemical transformations, CO_2-to-methane conversion was confirmed by the strong presence of CH_4 found in GC analysis following the photochemical reduction of CO_2 using visible light and a photosensitizer. The stabilization of an eight-electron reduction is attributed to the polypyridine ligand with two pendent amines that can act as proton relays.

While still in the early stages of optimization, the $Fe(bapbpy)(OTf)_2$ catalyst is a milestone in the electrochemical conversion of CO_2 to energy-rich products by utilizing the amine proton relay and polypyridine framework. This study is anticipated to inspire the development of more efficient homogeneous molecular catalysts for the electrochemical and photochemical reduction of CO_2 as a renewable energy source to meet the increasing energy demands while maintaining a sustainable global carbon cycle.

APPENDIX

COPYRIGHT PERMISSIONS

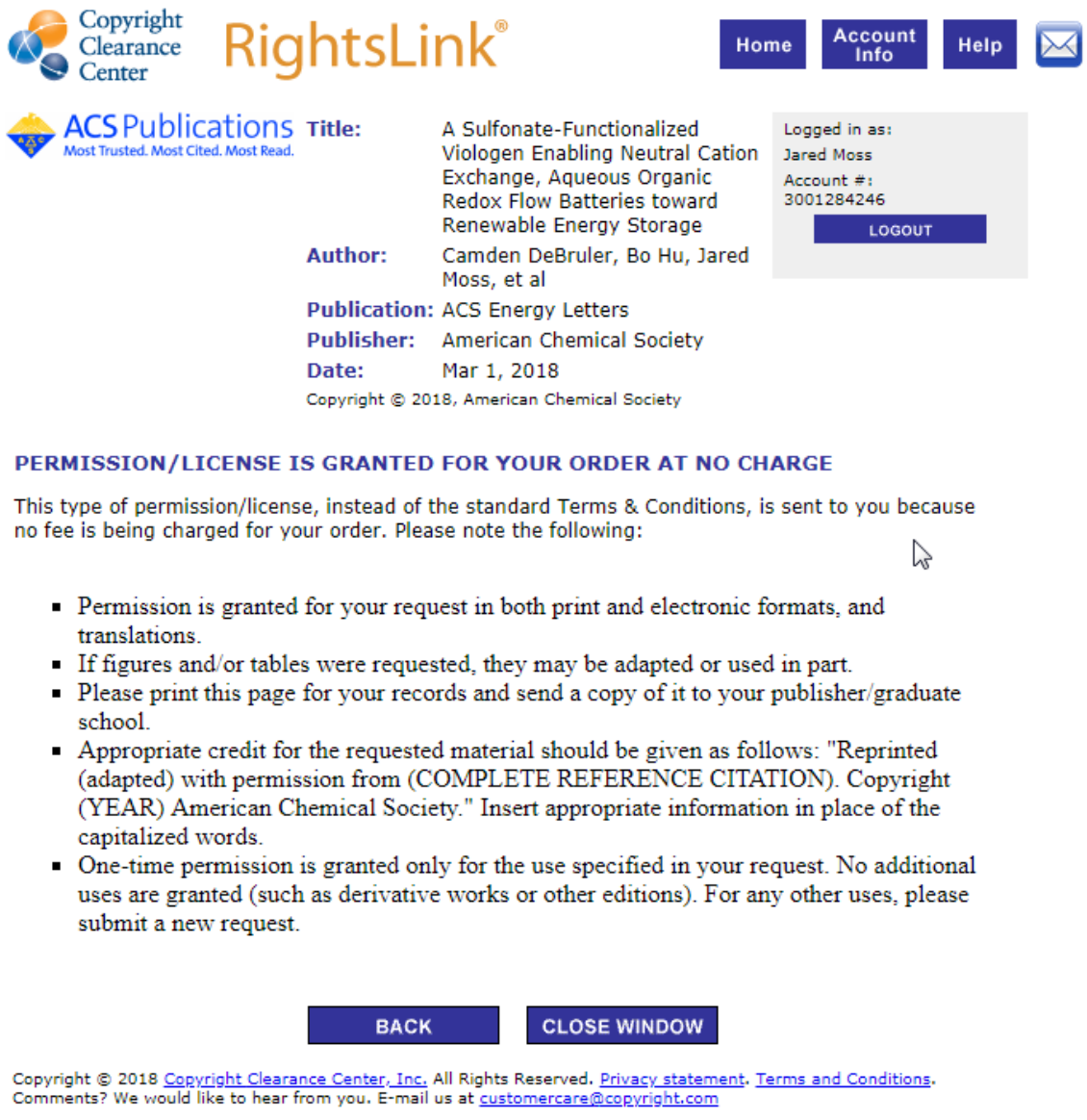

Copyright Clearance Center RightsLink®

Home | Account Info | Help

ACS Publications
Most Trusted. Most Cited. Most Read.

Title: A Sulfonate-Functionalized Viologen Enabling Neutral Cation Exchange, Aqueous Organic Redox Flow Batteries toward Renewable Energy Storage

Author: Camden DeBruler, Bo Hu, Jared Moss, et al

Publication: ACS Energy Letters

Publisher: American Chemical Society

Date: Mar 1, 2018

Copyright © 2018, American Chemical Society

Logged in as:
Jared Moss
Account #:
3001284246
LOGOUT

PERMISSION/LICENSE IS GRANTED FOR YOUR ORDER AT NO CHARGE

This type of permission/license, instead of the standard Terms & Conditions, is sent to you because no fee is being charged for your order. Please note the following:

- Permission is granted for your request in both print and electronic formats, and translations.
- If figures and/or tables were requested, they may be adapted or used in part.
- Please print this page for your records and send a copy of it to your publisher/graduate school.
- Appropriate credit for the requested material should be given as follows: "Reprinted (adapted) with permission from (COMPLETE REFERENCE CITATION). Copyright (YEAR) American Chemical Society." Insert appropriate information in place of the capitalized words.
- One-time permission is granted only for the use specified in your request. No additional uses are granted (such as derivative works or other editions). For any other uses, please submit a new request.

BACK | CLOSE WINDOW

Copyright © 2018 Copyright Clearance Center, Inc. All Rights Reserved. Privacy statement. Terms and Conditions.
Comments? We would like to hear from you. E-mail us at customercare@copyright.com

Figure A-1. Copyright permission from ACS Energy Letters for Chapter III.

Figure A-2. Copyright permission from Chem for Chapter III.